Nuclei Population Dynamics and Cavitation

Thesis by

Zhenhuan Liu

In Partial Fulfillment of the Requirements

for the Degree of

Doctor of Philosophy

California Institute of Technology

Pasadena, California

1995

(Submitted November 14, 1994)

Acknowledgments

There are many people who have played a role during the course of this work. I would like to thank my advisors, Dr. Christopher Brennen and Dr. Allan Acosta, whose professional guidance, encouragement and patience made this work possible.

My thanks also go to my colleagues, especially to Dr. Kotaro Sato, Dr. Yan Kuhn de Chizelle, Dr. Douglas Hart, Garrett Reisman, Yi-Chun Wang, Elizabeth McKenney and Fabrizio D'Auria.

I gratefully acknowledge the assistance of the professional staff of Caltech, especially Pavel Svitek, Marty Gould, Joseph Fontana and Richard Eastvedt.

Funding for this work was provided by the Office of Naval Research under contract number N-00014-85-K-0397 and N-0014-91-k-1295. This support is gratefully acknowledged.

Finally, I dedicate this thesis to my wife, Hongyu Piao.

Abstract

The effect of the nuclei population in water on cavitation has not been investigated thoroughly due to the difficulties of measuring the microbubbles in water. In this thesis, a Phase Doppler Anemometer (PDA) was calibrated by a holographic method and used to measure the micro-bubble distribution in water. Substantial agreement was achieved between the PDA and the holographic method. After the calibration, the PDA was used to study the nuclei population dynamics in two water tunnels. It was also employed in a study of cavitation on an axisymmetric Schiebe body in which the cavitation on the headform and the upstream nuclei population were simultaneously observed.

Substantial changes in the nuclei number density distributions were found in these two water tunnels. The nuclei population in each water tunnel can also vary significantly, sometimes by as much as an order of magnitude. The nuclei population dynamics are complicated and are affected by the tunnel design, the tunnel operating condition and the air content. The cavitation event rate on the Schiebe headform is mainly determined by the cavitation number. It increases dramatically as the cavitation number is decreased. It also varies with the magnitude and the shape of the nuclei number distribution. As the upstream nuclei population increases, the cavitation event rate increases. During the experiments, cavitation acoustic emissions were also measured and analyzed.

An analytical model based on the spherical bubble assumption and the Rayleigh-Plesset theory is developed to relate the free stream nuclei population to the cavitation event rate and the acoustic noise on an axisymmetric body. Complications, such as the effect of the boundary layer flow rate, of the bubble screening, of the bubble/bubble interactions and of the observable bubble size are examined and included in the model. The predicted

cavitation event rate and acoustic impulse are compared with the experimental observations. It is shown that the predicted event rates agree with the observations when the population is small, but that increasing discrepancies occur at lower cavitation numbers when the bubble density becomes larger. The predicted noise qualitatively agrees with the observations, but is generally larger than the observations, mainly due to the fact that the spherical bubble assumption usually departs from the observed bubble shape.

Contents

Acknowledgements ii

Abstract iii

Table of Contents v

List of Figures viii

List of Tables xiv

Nomenclature xv

1 Introduction 1

1.1 Background 1

1.2 Outline of Research 4

2 Experimental Equipment 6

2.1 Introduction 6

2.2 The Low Turbulence Water Tunnel 7

2.3 The High Speed Water Tunnel 8

2.4 Nuclei Measurement 8

2.5 Headform 11

2.6 Hydrophone 12

3 Nuclei Population Dynamics in Water Tunnels **22**

3.1 Variations of Nuclei Populations in Different Water Tunnels 22

3.2 Changes in the Nuclei Population with Tunnel Running Time 24

3.2.1 Results from the Low Turbulence Water Tunnel 24

3.2.2 Results from the High Speed Water Tunnel 27

3.3 Effects of Air Injection and De-aeration 29

3.4 Changes in the Nuclei Population with Cavitation Development on the Headform 31

3.5 Conclusions 33

4 Observation of Cavitation Event Rate and Noise **48**

4.1 Cavitation Event Rate 48

4.2 Observation of Cavitation Noise 52

4.3 Conclusions 53

5 An Analytical Model for Cavitation Event Rate **61**

5.1 Introduction 61

5.2 Spherical Bubble Dynamics 62

5.3 Cavitation Event Rate 65

5.3.1 Boundary Layer Effect 69

5.3.2 Bubble Screening Effect 70

5.3.3 Observable Bubble Size Effect 73

5.3.4 Effect of Bubble/Bubble Interactions 75

5.4 Results of the Analytical Model 78

5.5 Conclusions 82

6 Cavitation Noise **95**

6.1 Introduction 95

6.2 Acoustic Impulse 96

6.3 Impulse Width and Magnitude 100

6.4 Total Acoustic Emission 102

6.5 Comparisons of Predictions and Observations 104

6.6 Conclusions 105

7 Summary and Discussions **110**

References **116**

Appendices **126**

A Procedures for Adjusting Phase Doppler Anemometer **126**

A.1 Alignment of the Transmitting Laser and Optics 126

A.2 Adjustment of Receiving Optics and Electronics 128

B Bubble Screening Effects **131**

List of Figures

2.1 Cavitation experimental setup. 14

2.2 A schematic of the Low Turbulence Water Tunnel at Caltech. 15

2.3 High Speed Water Tunnel circuit schematic. 16

2.4 A schematic of hologram reconstruction. 17

2.5 A histogram of the nuclei number distribution measured by the PDA in the Low Turbulence Water Tunnel at a tunnel velocity of $9.1 m/sec$ and a cavitation number of $\sigma = 0.58$. 18

2.6 A comparison of PDA measured and holographically measured nuclei number density distributions in the Low Turbulence Water Tunnel. 19

2.7 A schematic diagram of the Schiebe headform used in the experiments. The dimensions are normalized by the headform diameter, D. 20

2.8 Pressure distributions on the Schiebe headform. (a) Pressure distribution along the headform surface; (b) Pressure distribution around the minimum pressure point. 21

3.1 A comparison of the nuclei number density distributions in the Low Turbulence Water Tunnel ($\diamond$) and the High Speed Water Tunnel ($\times$). 36

3.2 The effect of water tunnel running time on the free stream nuclei distribution in the Low Turbulence Water Tunnel at different tunnel working conditions. 37

3.3 Changes in the nuclei concentrations with the tunnel running time in the Low Turbulence Water Tunnel at Caltech at six different cavitation numbers. 38

3.4 Changes in the free stream nuclei distribution before and after running the water tunnel at $U = 8.9m/sec\,\sigma = 1.72$ for 10 minutes. $\sigma = 22.9$ ($\diamond$) before; ($\times$) after; $\sigma = 7.71$, (+) before and ($\square$) after. 39

3.5 Changes in the nuclei concentration with the tunnel running time in the High Speed Water Tunnel at Caltech at two different cavitation numbers: $\sigma = 0.47$ ($\diamond$) and $\sigma = 0.52$ (+). 40

3.6 The effect of the air injection on the free stream nuclei distribution in the Low Turbulence Water Tunnel at $U = 3.16m/sec$, $p = 109kPa$, $\sigma = 23.66$. 41

3.7 The effect of the de-aeration on the free stream nuclei distribution in the Low Turbulence Water Tunnel at $U = 5.12m/sec$, $p = 97kPa$, $\sigma = 7.51$. 42

3.8 Changes in the upstream nuclei concentrations before and after air injection in the High Speed Water tunnel. (I) nuclei concentration before air injection; (II) after air injection, changes in the nuclei concentration with the tunnel running time, and (III) nuclei concentration after a night rest of the tunnel. 43

3.9 Changes in the free stream nuclei concentration in the Low Turbulence Water Tunnel with tunnel operating conditions (cavitation number) at $U = 9m/sec$. 44

3.10 Changes in the free stream nuclei number density distribution in the Low Turbulence Water Tunnel at different cavitation numbers, $\sigma = 0.57$ ($\diamond$); $\sigma = 0.50$ (+) and $\sigma = 0.45$ ($*$) and at velocity $U = 9.0m/sec$. 45

3.11 Changes in the free stream nuclei number density distribution in the Low Turbulence Water Tunnel at a cavitation number of $\sigma = 0.57$ and a velocity of $U = 9.0m/sec$, but at different cavitation event rates: $E = 3sec^{-1}(\diamond)$; $E = 14sec^{-1}(\triangle)$; $E = 34sec^{-1}(*)$. 46

3.12 A comparison of the nuclei number density distributions in the Low Turbulence Water Tunnel and the High Speed Water Tunnel with measurements in other facilities and in ocean. 47

4.1 Variations of the cavitation event rate on a $5.08cm$ Schiebe body with cavitation number at $U = 9m/sec$ in the Low Turbulence Water Tunnel. The variations of event rates are distinguished for various ranges of free stream nuclei concentration. 55

4.2 Changes in the cavitation event rate on a $5.08cm$ Schiebe body in the Low Turbulence Water Tunnel as a function of free stream nuclei concentration at $U = 9m/sec$ and two cavitation numbers of $\sigma = 0.57$ and $\sigma = 0.45$. . . . 56

4.3 Changes in the cavitation event rate on a $5.08cm$ Schiebe headform as a function of cavitation number in the High Speed Water Tunnel. The data is plotted for various tunnel speeds and nuclei concentrations. 57

4.4 A comparison of typical nuclei number density distributions in the High Speed Water Tunnel at a cavitation number of $\sigma = 0.54$ and different tunnel velocities: $9.4m/sec$ $(\diamond)$ and $14.5m/sec$ $(+)$. 58

4.5 Probability density distributions of (a) the time between two events, T, normalized by the maximum time period between two events, T_{max}, and of (b) the bubble radius, R, normalized by the maximum bubble radius, R_{max}, at a velocity of $U = 9m/sec$ and at two different cavitation numbers: $\sigma = 0.45$ and $\sigma = 0.56$. 59

4.6 Dimensionless pressure impulse as a function of cavitation number measured in the High Speed Water Tunnel at Caltech. The data is plotted for various tunnel speeds and nuclei concentrations. 60

5.1 A schematic showing typical annular stream tube upstream and in the neighborhood of the minimum pressure point. 84

5.2 A comparison of the maximum bubble sizes obtained by asymptotic equation and numerical solution of Rayleigh-Plesset equation: (a) the pressure distribution used in the calculation; (b) the maximum bubble size plotted against cavitation number. 85

5.3 Variation in the minimum pressure coefficient, C_{PM}, on a streamline with the distance y of that streamline from the surface of the body near the minimum pressure point. (**A**): Potential flow solution, (**B**): $r_H/r_K = 1.5$, (**C**): $r_H/r_K = 2.0$, (**D**): $r_H/r_K = 2.5$. 86

5.4 The function $\Sigma(r/r_H)$ for the stagnation point flow in the potential flow around a sphere. 87

5.5 Typical event rates calculated using an assumed but typical nuclei distribution for flow around a 5.08cm Schiebe body at a velocity of 9m/sec. **Original**: Basic method not including the additional effects included in other lines. **Boundary layer**: As original but including the boundary layer flux effect. **Observable size**: As original but including only "observable" bubbles larger than 1mm in radius. **Screening**: As original but including the bubble screening effect. **Interactions**: As original but including the bubble interaction effect. 88

5.6 Calculated cavitation event rates for two different size headforms (5cm, 50cm) at three velocities (9m/sec, 11.5m/sec and 15m/sec). 89

5.7 A comparison of the predicted and observed cavitation inception numbers for various tunnel velocities (9 m/sec, 11.5 m/sec and 15 m/sec) and headform diameters (5cm, 25cm and 50cm). 90

5.8 Variation of maximum bubble size with cavitation number. 91

5.9 The predicted probability density distribution of maximum bubble size on the Schiebe headform at a velocity of 9m/sec and a cavitation number of 0.45. 92

5.10 A comparison of observed cavitation event rates ($\diamond$) on a 5.08cm Schiebe body in the Low Turbulence Water Tunnel at a speed of 9m/sec with anticipated event rates based on simultaneously measured nuclei distributions. 93

5.11 A comparison of observed cavitation event rates (lines with symbols) on a 5.08cm Schiebe body in the High Speed Water Tunnel at various speeds and nuclei concentrations with the anticipated event rates (corresponding lines without symbol) based on simultaneously measured nuclei distributions. . 94

6.1 A sketch of the variations of the bubble volume and the emitted acoustic pressure as a function of time. (a) Variation of the bubble radius with time, (b) Acoustic pressure generated, (c) Variation of the bubble volume with time. 106

6.2 A comparison of the predicted upper limit of the pressure impulse (I_m^*) and measured pressure impulses in the High Speed Water Tunnel as a function of cavitation number at different tunnel velocities. 107

6.3 Comparisons of the predicted dimensionless pressure impulses, I^*, with experimental measurements on a $5.08cm$ headform by Ceccio and Brennen (1992) as a function of maximum volume of the bubble (divided by r_H^3) at different cavitation numbers. 108

6.4 A comparison of the predicted (solid line) and the measured (dots) pressure impulse width for single bubble cavitation on a Schiebe headform with $r_H = 2.5cm$, $U = 9m/sec$ and $\sigma = 0.45$. The measurements were from Ceccio and Brennen (1992). 109

A.1 A schematic of the transmitting laser and optics setup for the Laser Doppler Anemometer. 130

B.1 Flow field around the stagnation point of a sphere. 135

List of Tables

B.1 Numerical values of $\Sigma(r/r_H)$ as a function of r/r_H. 134

Nomenclature

C	Nuclei concentration
C_P	Coefficient of pressure, $(p - p_\infty)/\frac{1}{2}\rho_L U^2$
C^*_{P1}	Constant used in the pressure coefficient distribution
C_{PM}	Minimum C_P on a given streamline
C_{PMS}	Minimum value of C_P on the headform surface
$C_{P_{crit}}$	Blake critical pressure coefficient, $(p_c - p_v)/\frac{1}{2}\rho_L U^2$
D	Headform diameter
E	Cavitation event rate
F_C	Combinations of various effects on cavitation noise
I	Pressure impulse
I^*	Dimensionless pressure impulse, $4\pi I/\rho_L U r_H$
I^*_m	Upper limit of the dimensionless pressure impulse
$N(R)$	Nuclei density distribution function
P_{max}	Probability density distribution of maximum bubble size on a cavitating body
R, R^*	Radius and dimensionless radius of a cavitation nucleus, $R^* = R/r_H$

$\dot{R}$, $\dot{R}^*$	$\frac{dR}{dt}$, $\frac{dR^*}{dt^*}$
$\ddot{R}$, $\ddot{R}^*$	$\frac{d^2R}{dt^2}$, $\frac{d^2R^*}{dt^{*2}}$
R_0, R_0^*	Bubble radius at initial equilibrium and its dimensionless form, $R_0^* = R_0/r_H$
R_M	Minimum radius of an observable cavitation bubble
R_C	Critical cavitation nucleus radius
Re	The Reynolds number, $U(2r_H)/\nu_L$
R_{max}	Maximum cavitation bubble radius
$R_x, \dot{R}_x$	Bubble radius and wall velocity at which the pressure impulse is calculated
S	Surface tension
T, T_{max}	Time between two cavitation events and the maximum time period between two cavitation events
U	Upstream tunnel velocity
U_M	Maximum velocity corresponding to C_{PMS}
V, V_{max}	Bubble volume and maximum bubble volume, $V_{max} = \frac{4\pi}{3}R_{max}^3$
$\dot{V}$	$\frac{dV}{dt}$
$\ddot{V}$	$\frac{d^2V}{dt^2}$
We	The Webber number
a	Radius of a sphere
c_0	Speed of sound
f_1, f_2, f_3	Numerical factors effecting the cavitation event rate
k	Polytropic constant for gas
n_i	Factor of bubble interactions
p	Fluid pressure

$p_{b\infty}$	Pressure at infinity
p_∞	Pressure upstream
p_{G0}, p_{GM}	Insoluble gas pressure inside a bubble at the origin equilibrium and the maximum bubble size
p_c	Blake critical pressure
$\bar{p}_i$	Average pressure level
p_l	Total acoustic pressure level
p_v	Vapor pressure
p_x	Surrounding pressure at which bubble collapses
q	Flow velocity, $q^2 = u^2 + v^2$
r_H	Headform radius
r_K	Radius of curvature of streamlines near minimum pressure point
r_S	Radius of minimum pressure point
r, y	Normal distances of a given streamline from axis far upstream and from body surface near the minimum pressure point
r_e	Effective radius
s, s_0	Coordinate along a streamline and the location of minimum pressure point
t, t^*	Time variable and its dimensionless form, $t^* = tU/r_H$
t_G	Duration of bubble growth
t_1, t_2	Moments at which the acoustic pressure is equal to the surrounding pressure
t_i, t_i^*	Pressure impulse duration and its dimensionless form, $t_i^* = t_i U/r_H$
u_ρ, u_θ	Fluid velocity components in a spherical coordinate

u, v Fluid velocity components in a cylindrical coordinate

u_M Fluid velocity just outside boundary layer

v_n Velocity of a bubble normal to streamline

y_M Maximum range for nuclei to cavitate

α The flow angle or the angle of scattered light

ρ, θ Spherical coordinates

ρ_L Fluid density

σ Cavitation number, $(p_\infty - p_v)/\frac{1}{2}\rho_L U^2$

σ_{crt} Threshold cavitation number

σ_i Inception cavitation number

ξ, λ Factors in the chosen analytical expression for $N(R)$

ν_L Kinematic viscosity of fluid

μ_L Fluid viscosity

δ, δ_2 Thickness and momentum thickness of boundary layer

ϵ Displacement of a bubble normal to streamline

Σ Function defined by equation (5.25)

Σ' $d\Sigma/d(r/r_H)$

Δs Distance traveled by a bubble in the low pressure region

Ψ Stream function

Chapter 1

Introduction

1.1 Background

Traveling bubble cavitation has been widely studied for a long time. The pioneering observations of single bubble cavitation made by Knapp and Hollander (1948) were followed by the analyses of Plesset (1949), Parkin (1952) and others (Oshima, 1961, van der Walle, 1962, Holl and Kornhauser, 1970, and Johnson and Hsieh, 1966). More recently, Ceccio and Brennen (1992) and Kuhn de Chizelle *et al.* (1992) performed a number of experiments to investigate the dynamics and acoustics of traveling bubble cavitation events. They investigated the scaling of cavitation on an axisymmetric body with the speed and the model size and revealed very complex phenomena. The influence of the nuclei influx on the cavitation event statistics of a given flow has also been studied (Schiebe, 1972, Baiter, 1974, Meyer *et al.*, 1989, 1992, and Ceccio and Brennen, 1992). But most of the investigations of the influence of the nuclei population were based on assumptions of characteristic nuclei distributions in a given flow. There have been significant discrepancies between the experimental

and theoretical results.

The limited evidence available indicates that changes in the nuclei population can be very important in determining cavitation inception, limited cavitation and even fully developed cavitation (Keller, 1972, 1974, Keller and Weitendorf, 1976, Kuiper, 1978, Gates and Acosta, 1978, Ooi, 1985, Ceccio and Brennen, 1992, Li and Ceccio, 1994). Many years ago, Lindgren and Johnson (1966) showed that differences in cavitation in different facilities could be ascribed to the differences in the nuclei content. However, apart from Keller's (1972, 1974) pioneering investigations, we know little about the changes in the nuclei population that may occur during a cavitation experiment and the influence of the nuclei population on cavitation.

The difficulties involved in the accurate measurement of the oncoming nuclei number density distribution function, $N(R)$, have been responsible for the delay in any detailed, quantitative investigation of this component of the problem. By definition, $N(R)dR$ is the number of nuclei with size between R and $R+dR$ per unit volume. Though many techniques for the measurement of cavitation nuclei have been developed over the past thirty years (Ripken and Killen, 1959, 1962, Feldberg, 1973, Keller, 1972, Morgan, 1972, Peterson, *et al.*, 1975, Gates and Acosta, 1978, Oldenziel, 1982, Le Goff and Lecoffre, 1983, and Cartmill and Su, 1993), few have been accepted as reliable and repeatable. As Billet (1985) remarked in his review of nuclei measurement techniques, the only reliable method of obtaining $N(R)$ has been the extremely time consuming procedure of surveying a reconstruction of an *in situ* hologram of a small volume of tunnel water. However, the time and effort required to construct one $N(R)$ distribution by this method has seriously limited the scope of these investigations. The recent development of light scattering instruments employing phase

Doppler techniques (Saffman and Buchhave, 1984, Tanger and Weitendorf, 1992 and Liu *et al.*, 1993) has improved the situation. The great advantage of the PDA system is the speed with which $N(R)$ can be measured. With this new instrument experiments can be performed to measure the nuclei population and to study its effect on traveling bubble cavitation.

In order to synthesize the cumulative effects of a stream of traveling cavitation bubbles, it is necessary to supplement the details of individual events with the rates at which these events occur. Many efforts have been made to relate the cavitation event rate to the nuclei population in the oncoming stream (see, for example, Schiebe, 1972, Keller, 1972, 1974, Keller and Weitendorf, 1976, Kuiper, 1978, Gates and Acosta, 1978, Meyer *et al.*, 1992, Ceccio and Brennen, 1992). At first sight this seems like a straightforward problem of computing the flux of nuclei into the region for which the local pressure is less than the vapor pressure, i.e., $C_P < -\sigma$. However, many complications arise which make this analysis more complicated than might otherwise appear. First, the boundary layer on the surface will clearly have an effect on the volume flux through the low pressure region. Second, the relative motion between the nuclei and the liquid can be important. Johnson and Hsieh (1966) identified this important phenomenon which occurs when nuclei experience the large fluid accelerations in the vicinity of the stagnation point. Other problems arise because the growing bubble rapidly reaches a size which is comparable to important dimensions such as the height of the iso-bar, $-C_P = \sigma$, above the surface. As a result different parts of the bubble surface are exposed to different pressure distribution and the bubble itself changes the local pressure distribution within the flow. Then it becomes necessary to resort to a complex procedure in order to calculate the shape and growth of the bubble. Such analyses,

which would take the place of the Rayleigh-Plesset calculations (see Kuhn de Chizelle, 1993 and Meyer *et al.*, 1992), are too complex for inclusion of these complicated effects in the present event rate analyses, at least initially. In place of this, we need to develop a somewhat heuristic treatment of these complicated effects.

1.2 Outline of Research

In our own laboratory we have attempted to validate and calibrate a Phase Doppler Anemometer (PDA) by taking simultaneous measurements of the nuclei in a water tunnel with the PDA and a holographic system. We present detailed descriptions of the experimental equipment and the calibration of the PDA system against the reliable method of holographic measurement in Chapter 2. After validation, the PDA could then be used with confidence for investigations of the nuclei population dynamics and of the aforementioned relation between $N(R)$ and the cavitation event rate.

Experiments on nuclei population dynamics and on cavitation event rates were performed in two water tunnels. The measured nuclei populations in these two tunnels and the observations of the nuclei population dynamics in each tunnel are presented in Chapter 3. Simultaneous measurements of the upstream nuclei density distribution and the cavitation event rate and noise on an axisymmetric Schiebe body were also carried out in these two tunnels. The observed effect of the nuclei population dynamics on the cavitation event rate and noise is presented in Chapter 4. The experimental data also provides a validation to the analytical model developed later.

In Chapter 5, an analytical model is developed to correlate the cavitation event rate to the nuclei population in the oncoming stream. The cavitation event rate is deduced

on the basis of the spherical bubble assumption and the Rayleigh-Plesset equation. Many complications, such as the effects of the boundary layer flow rate, of the bubble screening, of the observable bubble size and of the bubble/bubble interactions, have been examined and included in the model. The model reveals the relationship of cavitation event rate with the important parameters, such as free stream nuclei population, flow velocity and pressure, and is ready to adapt to other geometries.

Analysis of the acoustics of traveling bubble cavitation is carried out in Chapter 6. Though more approximate than the numerical simulation, it provides a simple method to estimate the noise and is easy to adapt to other applications. The predicted and observed cavitation noise are compared in Chapter 6.

Finally, we summarize and discuss the results in Chapter 7.

Chapter 2

Experimental Equipment

2.1 Introduction

To study the nuclei population dynamics in water tunnels and its effects on cavitation, experiments were performed in the Low Turbulence Water Tunnel and the High Speed Water Tunnel at Caltech. Cavitation on an axisymmetric Schiebe body was observed while the upstream nuclei population was simultaneously measured using a calibrated Phase Doppler Anemometer. Figure 2.1 shows the experimental setup. A Schiebe headform was installed on the center line of the water tunnel. The cavitation event rate on the headform was measured by flush-mounted electrodes on the headform surface, and cavitation noise was measured by a hydrophone installed inside the headform. The free stream nuclei population was measured by a Phase Doppler Anemometer. Detailed descriptions of the equipment and the instrumentation are given in the following sections.

2.2 The Low Turbulence Water Tunnel

A full description of the Low Turbulence Water Tunnel (LTWT) at Caltech, as shown in Figure 2.2, was presented by Gates (1977), but a brief description of the main features are presented here.

The working section of the Low Turbulence Water Tunnel is $2.5m$ long and has a square cross section of $31cm \times 31cm$. The maximum tunnel speed is about $10m/sec$ and the tunnel pressure ranges from $20kPa$ to $110kPa$. To eliminate solid particles in the water, the tunnel water was filtered by using a $5\mu m$ screen for about 7 to 10 hours before each experiment. For all the experiments, the velocity was set, and the static pressure of the water tunnel was controlled by a vacuum system.

To control the air content in the water, a de-aeration system was used. The main component of this system is a closed cylindrical vessel measuring 2.54 meter in length and 0.91 meter in diameter. Tunnel water is pumped to the top of the vessel, then forced through a series of vacuum paths before it is returned to the water tunnel by another pump. The typical flow rate for the de-aeration system was about $3m^3/hour$. After de-aeration, typical air content in the tunnel water was about $10ppm$ to $12ppm$.

An air injection system was used to raise the nuclei population. The air injection system draws water from downstream of the working section and makes the water saturated by mixing the water with high pressure air. It is then injected into the water tunnel stagnation section by a series of very fine nozzles at a flow rate of about $0.02m^3/hour$. Because of the relatively low pressure surrounding the nozzle, it was believed that the air injection only generated very small bubbles.

2.3 The High Speed Water Tunnel

Figure 2.3 shows the structure of the High Speed Water Tunnel (HSWT) at Caltech. The working section of the High Speed Water Tunnel is $1.17m$ long and has a circular cross section $356mm$ in diameter. It was designed for operation at any desired velocity up to $30.5m/sec$, and any pressure from $354kPa$ to the vapor pressure of water. The tunnel was de-aerated by running the tunnel at a low pressure (about $3.4kPa$) for two days before the experiments were performed. Typical air content after de-aeration was about $6ppm$ to $8ppm$. To increase the air content, nitrogen or air can be injected into the water tunnel. The nitrogen was mixed with the water by running the tunnel at a low speed for long time.

The major structural difference between the High Speed Water Tunnel and the Low Turbulence Water Tunnel is that the High Speed Water Tunnel has a resorber which is about $18m$ deep. The tunnel water goes up and down the resorber four times before entering the working section. The gasses released by the tunnel or the cavitating model are re-absorbed before the flow re-enters the working section.

2.4 Nuclei Measurement

Recently, the Phase Doppler Anemometer (PDA) has been used to measure velocities and size distributions of particles. Saffman and Buchhave (1984) developed the physical principle of the phase-diameter relationship for particles going through the focal volume of two laser beams. When a particle passes through the intersection of two laser beams, the fringe pattern existing in the focal volume is projected into space mainly due to reflection from the bubble surface. This projection is equivalent to the Doppler burst. Two or more

photomultipliers at different points in space receive the same Doppler burst, but with a phase lag. This phase difference is related to the size of the particle.

The PDA has been used to measure the velocity and size of particles in the air successfully. But to apply the PDA to measure micro-bubbles in water, it is crucial to provide verification and calibration of the PDA with some reliable methods. Tanger and Weitendorf (1992) did applicability tests for a PDA by measuring latex spheres in water using a PDA and a microscope. Their results showed very good agreement in the sphere diameter and concentration measurement. It is still very important to verify the PDA for measuring air bubbles in water. For this purpose, simultaneous measurements of the free stream nuclei number distributions at different tunnel speeds, pressures and aeration levels were made in the Low Turbulence Water Tunnel at Caltech, using a PDA made by DANTEC and an on-line holographic system.

The PDA utilizes a $200mW$ Argon-ion laser with $514.7nm$ wavelength. It has three photomultipliers. Two of them are used to measure the phase difference of the scattered light. The third photomultiplier provides a spherical check of the signals to discriminate between bubbles and particles. As shown in Figure 2.1, the transmitting optics were mounted horizontally. The laser beams focused at the center line of the water tunnel. This focusing volume of the laser beams measured $0.204mm \times 0.203mm \times 2.348mm$. The receiving optics were mounted above the top window at a plane normal to the laser beams and focused at the center plane of the water tunnel and collected light scattered at an angle of $82°$ to the incident laser beams.

During the experiments, it took about five to fifteen minutes to finish one PDA data acquisition, while several holograms were taken. Then the holograms were reconstructed

and processed. Figure 2.4 is a schematic of the hologram reconstruction and viewing system. A $12mW$ He-Ne laser is used as the illumination source. The slide mounted hologram is transported on an X-Y-Z vernier carriage along the axis of the collimated beam. Reconstructed images are imaged through a $\times 10$ microscope objective onto a video camera and displayed on a monitor. The total magnification from the nuclei to the monitor is about 100. The nuclei are sized directly from the monitor. Typically, 6 to 12 sample volumes were processed on each hologram, and this required about one to two man-days.

A histogram of the nuclei in the Low Turbulence Water Tunnel measured by the PDA is presented in Figure 2.5. A peak appears at the nucleus radius of $12\mu m$. This is quite different from the results of Peterson *et al.* (1975), where the nuclei number distributions approach maximum values as bubble radius approaches zero. The statistics of the nuclei sizes and the velocities shows that the correlation coefficient between the velocity and the radius is about 0.08, which means that the velocity of an individual bubble is quite independent of its size.

Figure 2.6 shows a typical comparison of the nuclei density distributions measured by holographic method and PDA. The nuclei density distribution, $N(R)$, is defined so that the nuclei concentration in a narrow radius range $\triangle R$ is $N(R)\triangle R$. It follows that the total nuclei concentration is $\int_0^\infty N(R)dR$. As one can see in Figure 2.6, substantial agreement between these two techniques was achieved. it should be noted that the number of nuclei measured by the holographic method is consistently larger than that measured by the PDA. This probably is due to the fact that the focal volume of PDA laser beams is so small that some of the bubbles passing through only part of the focal volume are not counted. It should be noted that the holographic method was limited to nucleus radii larger than $10\mu m$

and the data only provide calibration of the PDA measurements for bubbles of radius larger than $10\mu m$. Note that the holographic data shows some scatter. This is primarily because of the small numbers of nuclei counted in the larger size ranges.

The PDA was then applied to study the changes in the nuclei population in the Low Turbulence Water Tunnel at different tunnel operating conditions by using the same setup as shown in Figure 2.1 (see Chapter 3). It was also used to measure the nuclei density distributions while the cavitation event rate and noise were measured on a Schiebe headform (see Chapter 4). Later the data was used to verify an analytical model to correlate cavitation event rate and noise with free stream nuclei population (see Chapter 5).

The same PDA system was also used to monitor the free stream nuclei population in the High Speed Water Tunnel. Before using the PDA system in the High Speed Water Tunnel, a check was made to make sure that the changes in the tunnel design and measurement environment did not affect the PDA performance. The check was done by measuring nuclei number density distributions in saturated water from a small injector in both the High Speed Water Tunnel and the Low Turbulence Water Tunnel. The results were almost identical, showing that the calibration was the same in the Low Turbulence Water Tunnel and the High Speed Water Tunnel. This check verified that the changes in the measurement environment did not affect the PDA measurement.

2.5 Headform

A $5.08cm$ diameter Schiebe headform made from lucite was mounted on the center line of the tunnel working section. A schematic of the headform is shown in Figure 2.6. This headform presents relatively smooth but strong adverse pressure gradients and the boundary

layer has therefore the property of being relatively robust to laminar detachment, unlike the ITTC body (Lindgren and Johnson, 1966). The pressure coefficient along the headform surface and the pressure distribution around the minimum pressure point are presented in Figure 2.6.

The interior of the headform was hollow and a hydrophone was placed inside the headform. The interior was then filled with water at atmospheric pressure. Because of the close match of acoustic characteristics between lucite and water, the hydrophone measurement is not significantly effected by the geometry of the headform (see Ceccio and Brennen, 1992).

Three flush ring electrodes of silver epoxy covering the entire periphery were installed in the lucite headform and allowed the detection of cavitation events occurring on the headform (Ceccio and Brennen, 1992 and Kuhn de Chizelle *et al.*, 1992). A pattern of alternating voltages is applied to the electrodes, and the electric current from each is monitored. When a bubble passes over one of the electrodes, the impedance of the flow is altered causing a drop in current which can be detected. The time between events is also measured and the event rate can therefore be measured.

2.6 Hydrophone

An ITC-1042 hydrophone was used to measure the cavitation noise. The hydrophone has a flat frequency response in the frequency range of $1Hz$ to $80kHz$. The hydrophone signal was filtered and amplified by an amplifier made by Princeton Applied Research (model 113). The amplifier also has a flat frequency response in the above frequency range. The acoustic data was acquired at a sampling rate of $1mHz$.

The hydrophone was placed in the hollow interior of the headform, as shown in Fig-

ure 2.6; then the interior was filled with tunnel water. Ceccio and Brennen (1992) showed that because of the relatively good acoustic impedance match between lucite and water, the interior hydrophone allows the noise generated by the cavitation bubbles to reach the hydrophone relatively undistorted; reflected acoustic signals from other parts of the water tunnel only make their appearance after the important initial signal has been recorded.

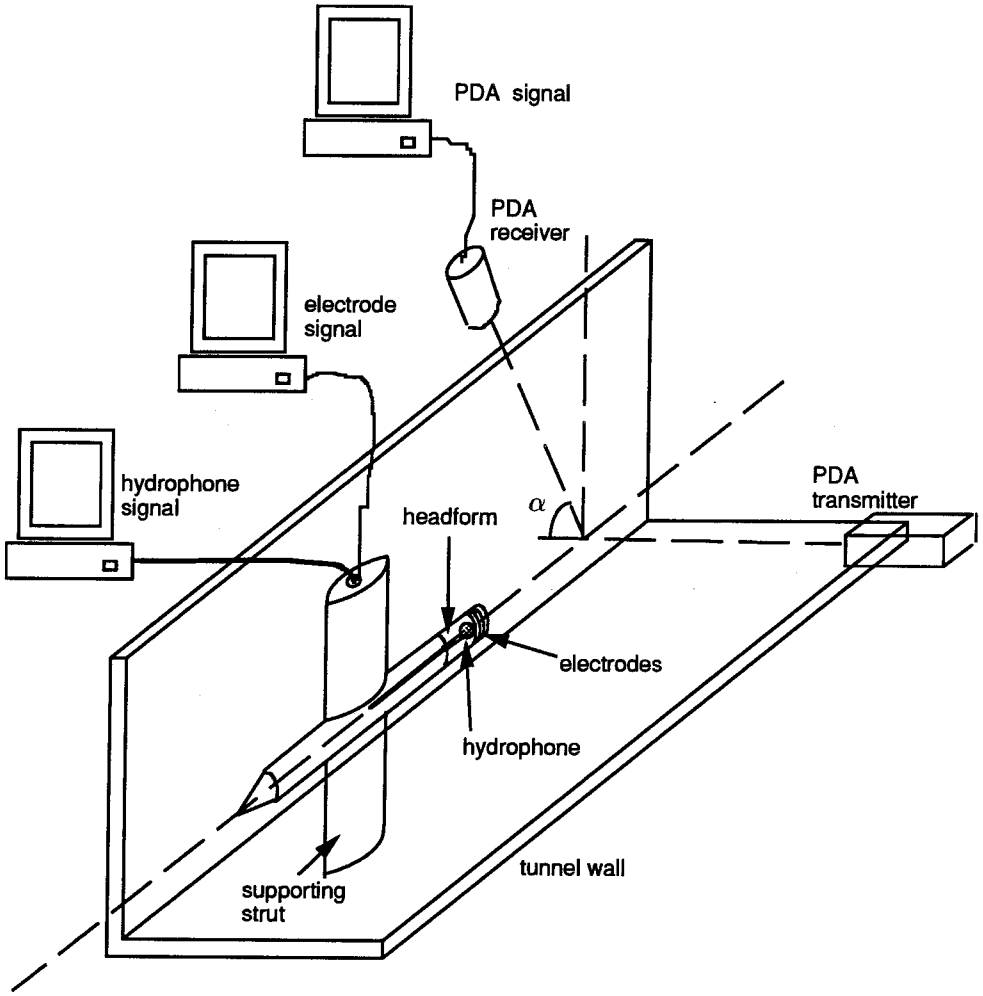

Figure 2.1: Cavitation experimental setup.

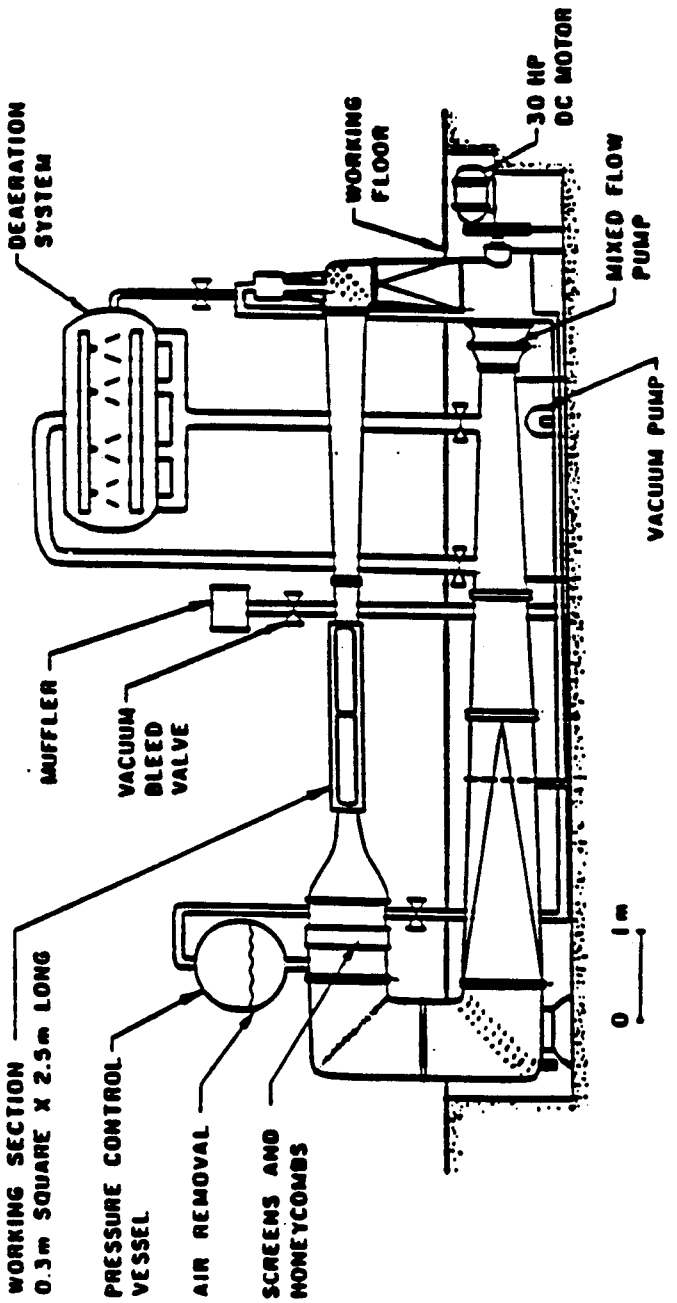

Figure 2.2: A schematic of the Low Turbulence Water Tunnel at Caltech.

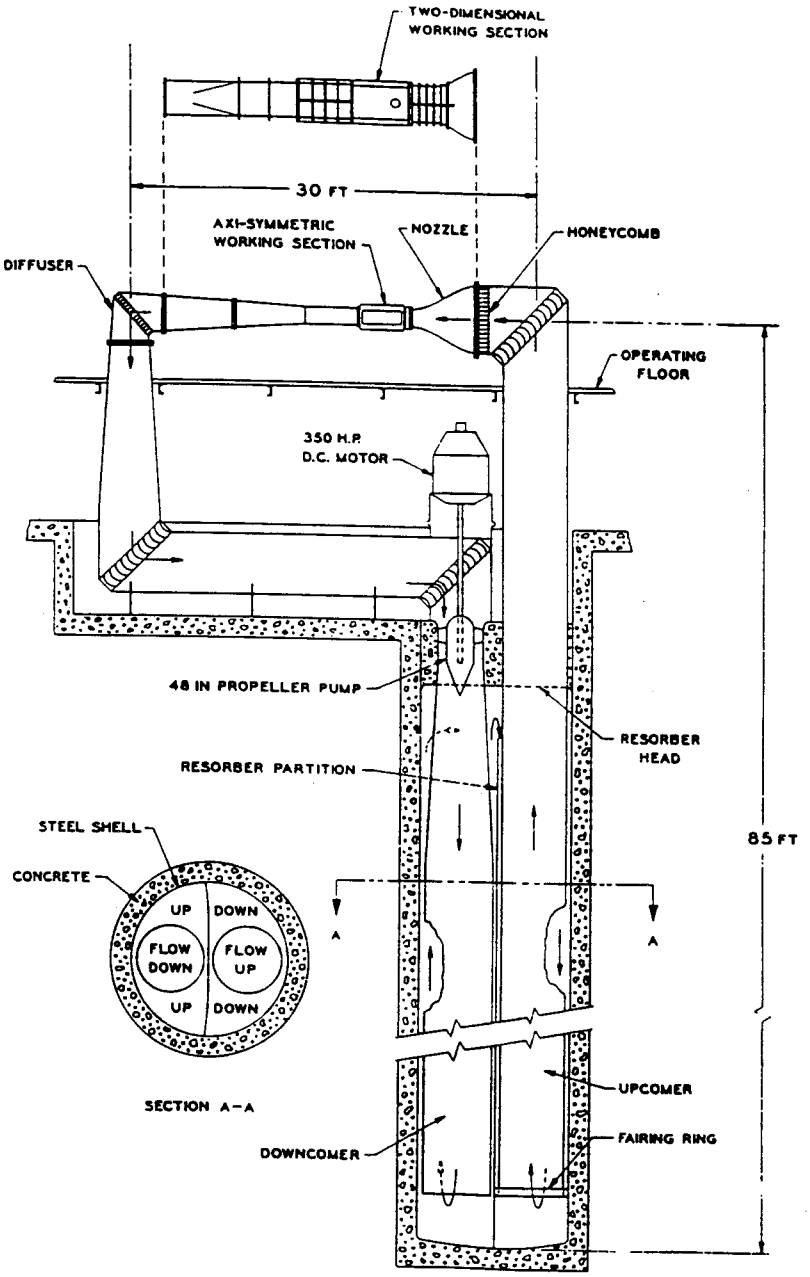

Figure 2.3: High Speed Water Tunnel circuit schematic.

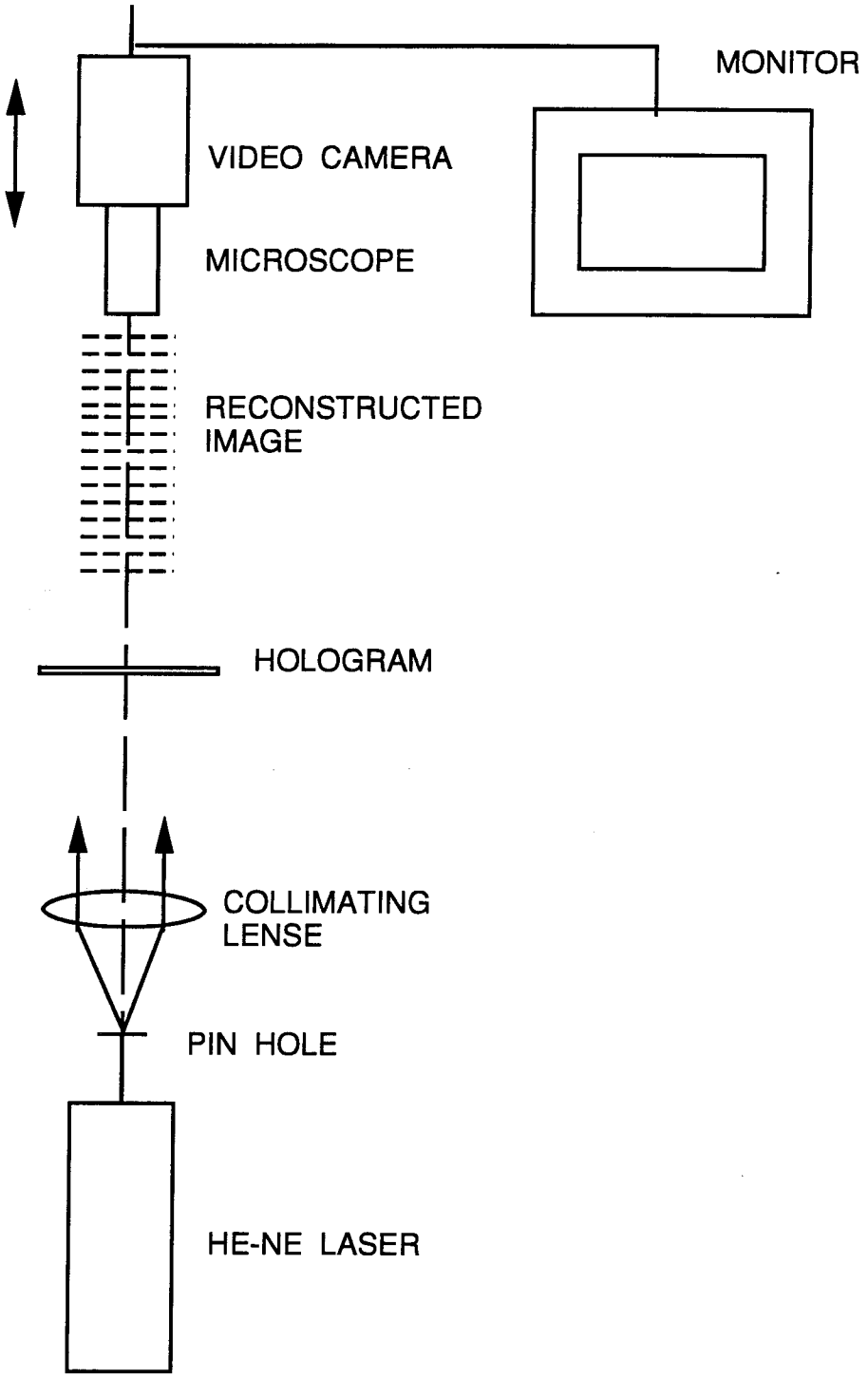

Figure 2.4: A schematic of hologram reconstruction.

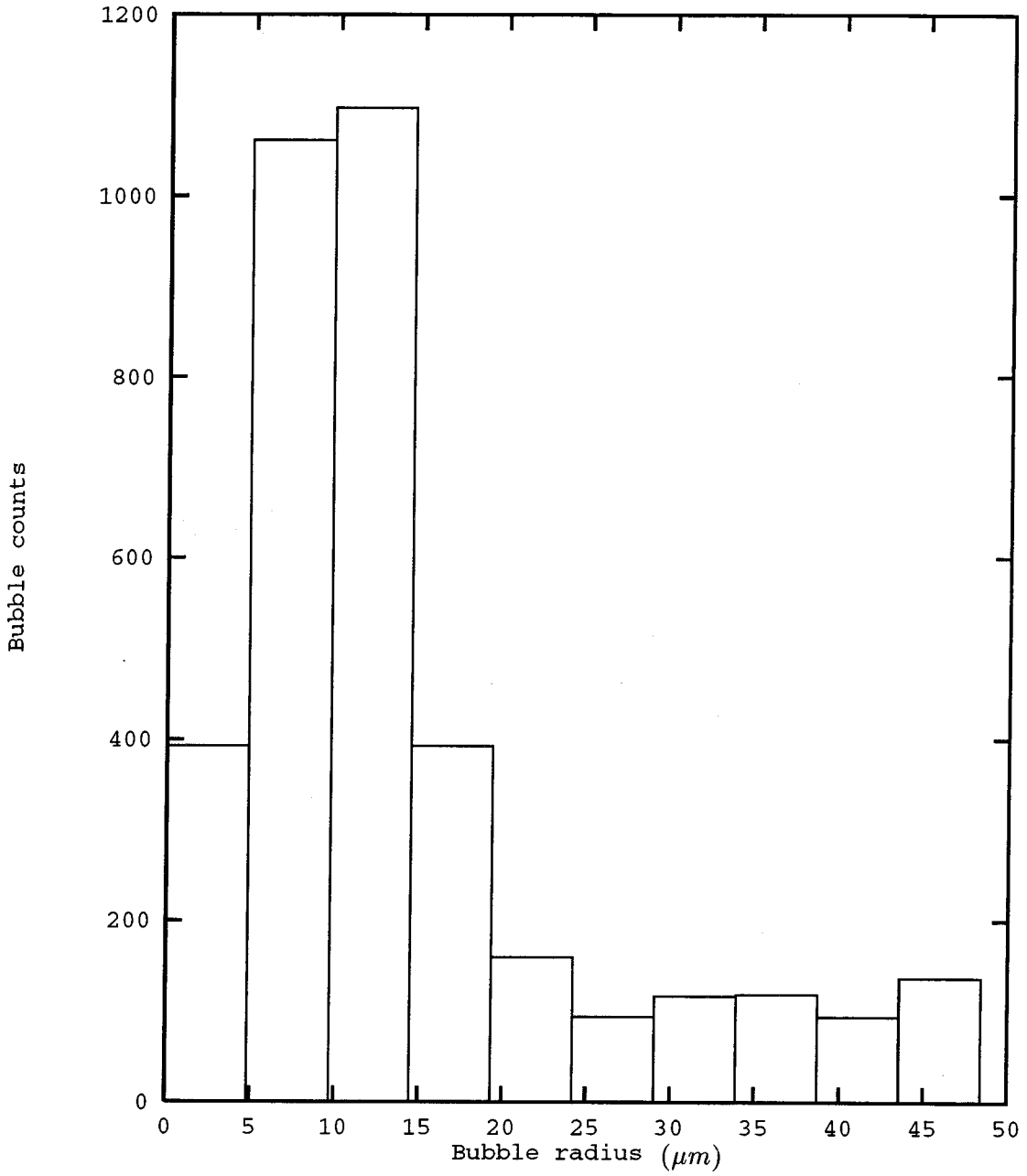

Figure 2.5: A histogram of the nuclei number distribution in the Low Turbulence Water Tunnel at a tunnel velocity of $9.1 m/sec$ and a cavitation number of $\sigma = 0.58$.

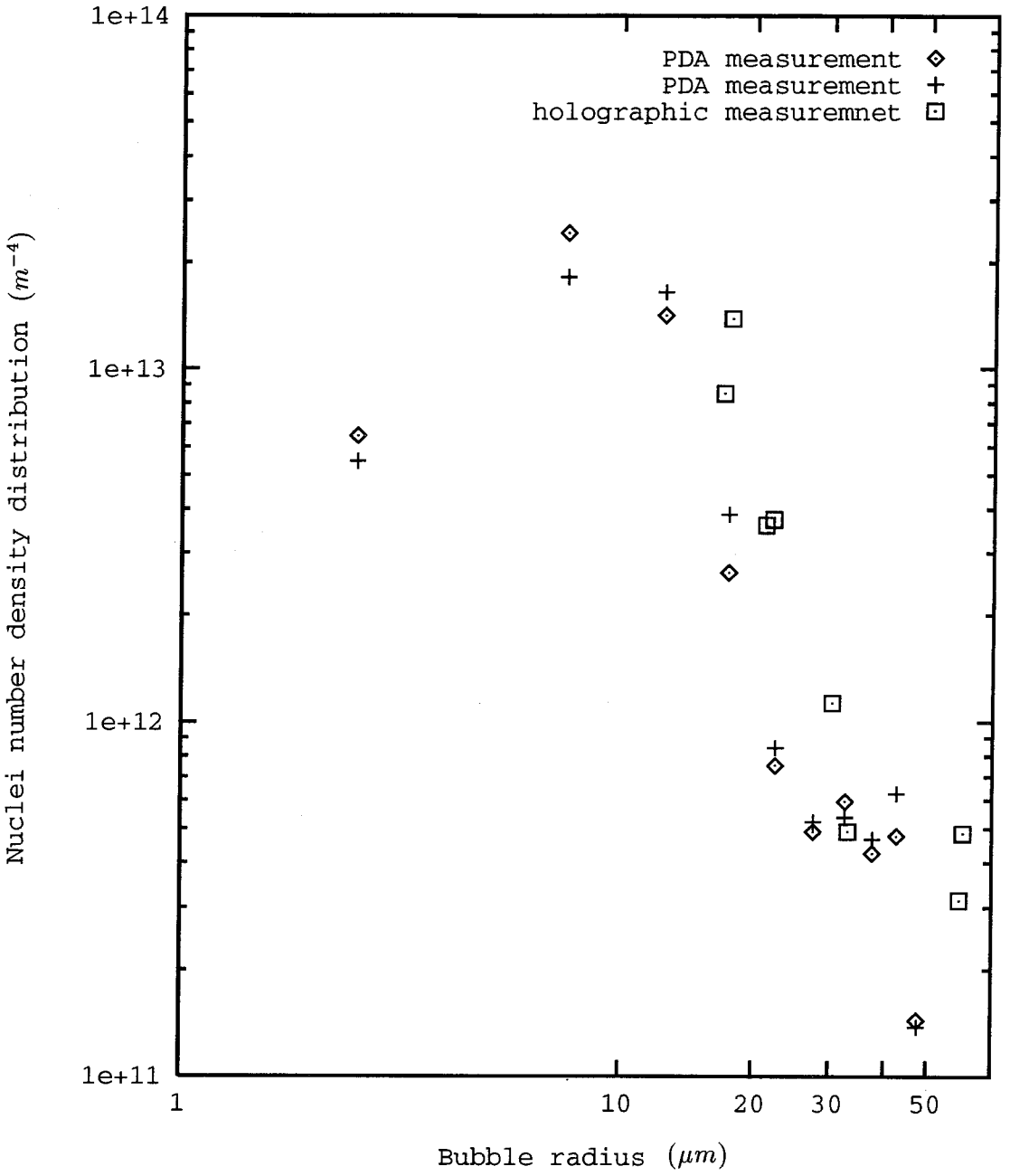

Figure 2.6: A comparison of PDA measured and holographically measured nuclei number density distributions in the Low Turbulence Water Tunnel at a tunnel velocity of $6.10 m/sec$, pressure of $93.9 kPa$ and corresponding cavitation number of 4.89.

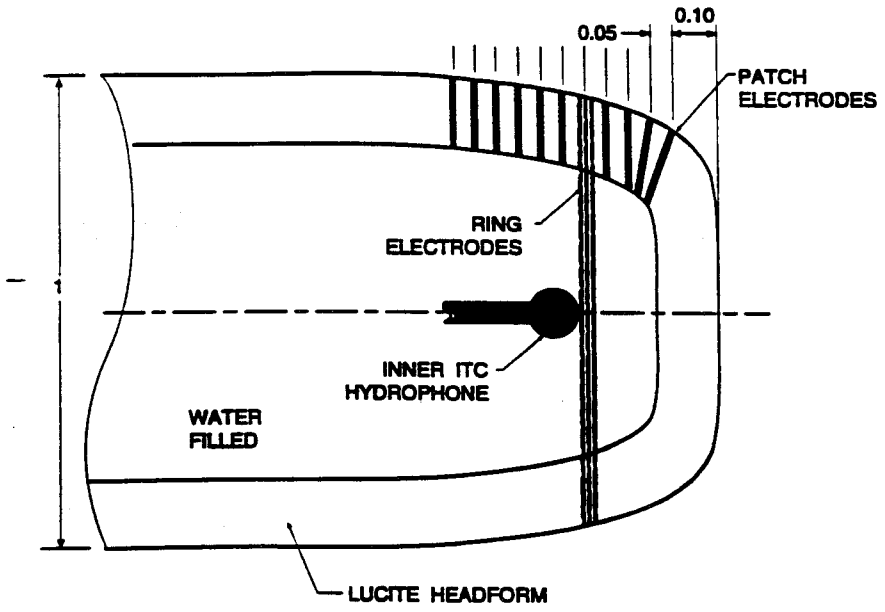

Figure 2.7: A schematic diagram of the Schiebe headform used in the experiments. The dimensions are normalized by the headform diameter, D.

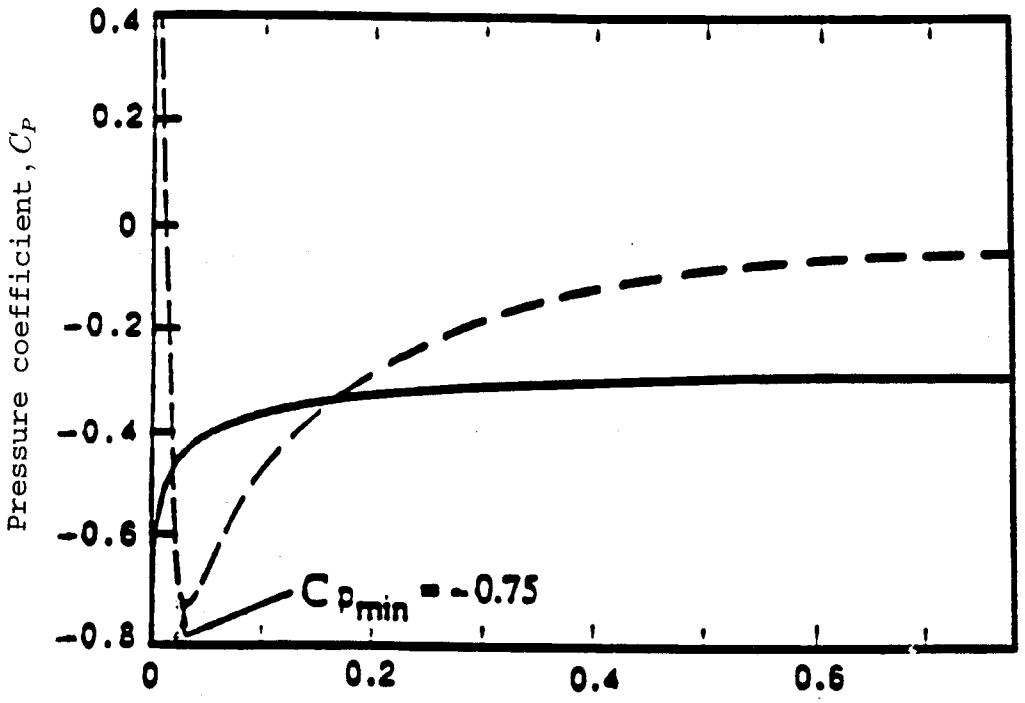

Figure 2.8: Pressure distribution on the Schiebe headform.

Chapter 3

Nuclei Population Dynamics in Water Tunnels

The differences in the nuclei population in different facilities have been identified by other researchers (Peterson, 1972, Feldberg and Shlemenson, 1973, Peterson *et al.*, 1975, Arndt and Keller, 1976, Gates and Bacon, 1978, Weitendorf and Tanger, 1993, Cartmill and Su, 1993, and Gindroz and Billet, 1994). We shall demonstrate in this chapter that not only the nuclei populations but also the population dynamics can be quite different in different water tunnels.

3.1 Variations of Nuclei Populations in Different Water Tunnels

A comparison of the nuclei number density distributions in the Low Turbulence Water Tunnel and the High Speed Water Tunnel is shown in Figure 3.1. Both distributions are

similar in shape, but have a difference of about two orders in magnitude. The typical nuclei concentration in the Low Turbulence Water Tunnel was $150cm^{-3}$, while, in the High Speed Water Tunnel, the typical nuclei concentration was $1cm^{-3}$. Later, we will demonstrate that de-aeration, air injection and the changes in the tunnel operating condition can bring substantial changes in the nuclei population. However, even with these variations included, the High Speed Water Tunnel and the Low Turbulence Water Tunnel still have very different nuclei concentration ranges. Typically, the nuclei concentration in the Low Turbulence Water Tunnel ranges from $80cm^{-3}$ to $270cm^{-3}$; while in the High Speed Water Tunnel the nuclei concentration is between $0.7cm^{-3}$ to $15cm^{-3}$. The difference in the nuclei number density distribution results in very different cavitation phenomena on the same Schiebe body, which will be demonstrated later.

The cause of the difference in the nuclei populations in these two tunnels is not completely clear. In part, it is due to the differences in the design of the tunnels. The High Speed Water Tunnel has a resorber (see Figure 2.3). The tunnel water goes down and up four times before entering the test section. The pressure in the resorber is also much higher than in the working section. The Low Turbulence Water Tunnel, however, does not have any such device. The water circulates directly from the downstream to the working section. Sato *et al.* (1993) studied the nuclei population in the wake of a cavitating cylinder in the Low Turbulence Water Tunnel. The nuclei population in the wake was several orders of magnitude larger than upstream and the process of mixing and diffusion with distance downstream was readily apparent. The resorber used in the High Speed Water Tunnel may be very effective in the sense of mixing and diffusing the microbubbles, since the water travels a longer distance and experiences a higher pressure before re-entering the working

section. In the Low Turbulence Water Tunnel there is no such device to suppress the air bubbles.

The de-aeration systems could also make a difference in the nuclei population. The de-aeration process in the High Speed Water Tunnel put all the tunnel water under low pressure ($3.4kPa$). In the Low Turbulence Water Tunnel only a small portion of tunnel water was subjected to low pressure in the de-aeration tank. Thus the High Speed Water Tunnel could be de-aerated more efficiently, as was verified by air content measurement. The air content in the Low Turbulence Water Tunnel ranged from $10ppm$ to $12ppm$ after de-aeration, compared with $6ppm$ to $8ppm$ in the High Speed Water Tunnel.

3.2 Changes in the Nuclei Population with Tunnel Running Time

3.2.1 Results from the Low Turbulence Water Tunnel

Experiments were performed in the Low Turbulence Water Tunnel at two large cavitation numbers, $\sigma = 22.7$ and $\sigma = 8.28$; two intermediate cavitation numbers, $\sigma = 7.63$ and $\sigma = 3.01$; and two small cavitation numbers, $\sigma = 2.34$ and $\sigma = 1.17$. Typical effects of water tunnel running time on the free stream nuclei number density distribution at different cavitation numbers in the Low Turbulence Water Tunnel are shown in Figure 3.2, where the water tunnel running time is denoted by t. The corresponding changes in the nuclei concentration are shown in Figure 3.3.

As shown in Figure 3.2 (a), at cavitation number of $\sigma = 22.7$ ($U = 3.16m/sec$, $p = 104kPa$), the free stream nuclei distribution decreased about half a decade during

a three-hour running time; similar changes occurred at a cavitation number of $\sigma = 8.28$ ($U = 3.16m/sec$, $p = 40kPa$). And from Figure 3.3, it is very clear that the nuclei concentrations at these two cavitation numbers are decreasing functions of time. At $\sigma = 22.7$, the nuclei concentration decreased from $406cm^{-3}$ at the beginning to $196cm^{-3}$ after 96 minutes and decreased further to $135cm^{-3}$ after 183 minutes. Similar decrease in nuclei concentration happened at $\sigma = 8.28$. Also from Figure 3.3, the rate of decline in the nuclei concentration slows down as time proceeds. At both $\sigma = 22.7$ and $\sigma = 8.28$, the bubble nuclei concentrations approached the same equilibrium.

At intermediate cavitation numbers: $\sigma = 7.63$ ($U = 5.13m/sec$, $p = 98kPa$) and $\sigma = 3.01$ ($U = 5.13m/sec$, $p = 40kPa$), the tunnel running time had little effect on the free stream nuclei distribution. As shown in Figure 3.2 (b) and (c), there was very little change in the cavitation nuclei number distribution during a 3 hour run at $\sigma = 7.63$. These two trends are also manifested in Figure 3.3, where for both cases, the nuclei concentrations remained almost constant. As shown in Figure 3.3, after a 3 hour run at $\sigma = 3.01$, the nuclei number in the radius range from 10 to $25\mu m$ remained almost unchanged while the nuclei number in the radius range from 25 to $50\mu m$ increased slightly. Again both cases seem to yield the same asymptotic distribution at long tunnel running time.

Finally experiments were also performed at two small cavitation numbers: $\sigma = 2.34$ ($U = 8.00m/sec$, $p = 77kPa$) and $\sigma = 1.17$ ($U = 8.00m/sec$, $p = 40kPa$). Typical changes in the nuclei number distribution at $\sigma = 2.34$ are shown in Figure 3.2 (d). The nuclei distributions increased with tunnel running time at both cavitation numbers. In Figure 3.3, it can be seen that the increase in the nuclei distribution was completed within the first 50 minutes, after which the distribution remained almost unchanged. At $\sigma = 1.17$, the nuclei

concentration increased faster than at $\sigma = 2.34$. The asymptotic distribution approached at $\sigma = 1.17$ was also a little higher than that of $\sigma = 2.34$.

Figure 3.3 shows the changes in the nuclei concentration with the tunnel running time in the Low Turbulence Water Tunnel. It is very clear that the trends of the changes in the nuclei concentration with the tunnel running time are quite different of large cavitation numbers ($\sigma \geq 8.28$), intermediate cavitation numbers ($7.63 \geq \sigma \geq 3.01$) and small cavitation numbers ($\sigma \leq 2.34$). At large cavitation numbers, the nuclei concentration increases with time; at small cavitation numbers, the nuclei concentration decreases with time; and at intermediate cavitation numbers, the nuclei concentration remains almost unchanged. It may have been noted from Figure 3.3 that the asymptotic nuclei concentrations for $\sigma = 3.01$ and $\sigma = 7.63$ are smaller than those of $\sigma = 8.28$ and $\sigma = 22.7$. The reason for this lies in the history prior to the measurements. The experiments with $\sigma = 3.01$ and $\sigma = 7.63$ were performed just after a four-hour run at $\sigma = 22.7$ during which substantial nuclei solution took place. And since at $\sigma = 3.01$ and $\sigma = 7.63$, the nuclei distributions remain almost unchanged, the nuclei concentration remained below the asymptotic concentration for $\sigma = 22.7$ and $\sigma = 8.28$ as a result of low initial free air content. It can also be seen in Figure 3.3 that, as the cavitation number decreases from 22.7 to 1.17, the changes in nuclei concentrations as a function of time goes from negative to nearly zero, then to positive.

To verify that running the Low Turbulence Water Tunnel at low cavitation numbers increases the nuclei concentration, the water tunnel was first run at a large cavitation number. Then it was run at a low cavitation number. After a short time, it was again run at the large cavitation number. The nuclei number distributions are compared for the same velocity and cavitation number. Experiments were performed in which the water

tunnel was first run at $\sigma = 22.9$ ($U = 3.19m/sec$, $P = 106kPa$) and $\sigma = 7.71$ ($U = 5.10m/sec$, $P = 98kPa$) respectively for 15 minutes. After this the water tunnel was run at $\sigma = 1.72$ ($U = 8.86m/sec$, $P = 71kPa$) for 10 minutes. Then, in the final phase the water tunnel was again run at the original conditions. The corresponding changes in the nuclei number density distributions are shown in Figure 3.4. In both cases the nuclei number distributions increased substantially after the low pressure period. For the first experiment, the nuclei number density distribution increased about an order of magnitude. And for the second experiment the increase in the nuclei number density distribution was about half a decade. Correspondingly, changes occurred in the nuclei concentration. The nuclei concentrations were $71cm^{-3}$ for $\sigma = 22.9$ and $126cm^{-3}$ for $\sigma = 7.71$ originally. After running the water tunnel at $\sigma = 1.72$ for 10 minutes, the nuclei concentrations jumped to $472cm^{-3}$ for $\sigma = 22.9$ and $460cm^{-3}$ for $\sigma = 7.71$. And when the water tunnel was run at $\sigma = 1.72$, the nuclei concentration was $510cm^{-3}$.

3.2.2 Results from the High Speed Water Tunnel

In the High Speed Water Tunnel, the tunnel running time had a dominant effect on the nuclei population. The nuclei concentrations decreased with the tunnel running time regardless of the tunnel operating condition. The nuclei population seemed to be unaffected by the tunnel operating condition. Typical changes in the nuclei population in the High Speed Water Tunnel are shown in Figure 3.5. At both cavitation numbers shown in the figure, the nuclei concentration decreased substantially with the tunnel running time. For example, during a 60-minute run of the water tunnel at a cavitation number of 0.52, the nuclei concentration decreased from $1.51cm^{-3}$ at the beginning to $0.82cm^{-3}$. It may have

been noted that the nuclei concentration at $\sigma = 0.47$ is much larger than that of $\sigma = 0.52$. This is due to the fact that the experiment at $\sigma = 0.47$ was performed immediately after a two-hour air injection. After the air injection, the nuclei concentration increased to $11.2cm^{-3}$. Then the nuclei concentration decreased monotonically from $11.2cm^{-3}$ during a three-hour experiment. At the end of the three-hour run, the nuclei concentration was $2.4cm^{-3}$; in other words, it had almost returned to the nuclei concentration before the air injection.

We have demonstrated that the changes in the nuclei population in the High Speed Water Tunnel and the Low Turbulence Water Tunnel are quite different. We can not claim that the trends in these two tunnels would necessarily occur in other facilities since the tunnel design and flow fields are quite complicated. But some of the trends would seem to have generality. We have confirmed that the resorber in the High Speed Water Tunnel plays a major role in determining the nuclei population. Since the nuclei in water travels a longer distance and experiences a higher pressure in the resorber, the nuclei in the High Speed Water Tunnel have a much better chance to dissolve in the water. On the other hand, in the Low Turbulence Water Tunnel the water is circulated directly back into the working section; thus the nuclei generated in the working section will re-enter the working section with little chance to dissolve. Therefore, we can make the following general conclusion. If a water tunnel has a device such as the resorber in the High Speed Water Tunnel at Caltech, the nuclei population in that water tunnel will remain relatively constant regardless of the tunnel operating condition. If a tunnel does not have such a device, the nuclei population in the tunnel will change according to the tunnel operating condition. At large cavitation numbers, when there is no cavitation in the water tunnel, free air bubbles dissolve into the

water slowly. Thus the nuclei population will decrease with the tunnel running time. But, at low cavitation numbers, when there is cavitation in the water tunnel (on the propeller blades, behind the honeycomb or screen), free air bubbles are generated and circulated into the working section, raising the nuclei concentration in the water tunnel. However, the increase and decrease in nuclei concentration seem to have certain asymptotic limits for each operating condition. This raises the question as to whether the cavitation on a model in the working section would, in itself, control the nuclei population in the water tunnel. How long would it take for the model/tunnel generated distribution to reach equilibrium and would that equilibrium differ greatly from operating point to operating point. These questions need further investigation.

3.3 Effects of Air Injection and De-aeration

In the Low Turbulence Water Tunnel, an air injection system was used to raise the nuclei population. The air injection system injects saturated water into the water tunnel stagnation section by a series of very fine nozzles at a flow rate of about $0.02m^3/hour$. Figure 3.6 shows the changes in the nuclei number density distribution in the Low Turbulence Water Tunnel during and after the air injection. The nuclei number density distribution increased a little during the air injection. But once the air injection was stopped, the nuclei number density distribution returned to the original distribution. The nuclei concentration rose from $235cm^{-3}$ to $273cm^{-3}$ during the air injection, and returned to $233cm^{-3}$ after the air injection was stopped.

We conclude that the air injection system used in the Low Turbulence Water Tunnel is not effective to increase the free stream nuclei population. The main reason is that the

flow rate of the air injection system is so small that it takes a long time to make significant changes in the large volume of tunnel water.

The air injection in the High Speed Water Tunnel was very effective in raising the nuclei population. Nitrogen was injected into the water tunnel when the tunnel was run at a low speed ($U \approx 2m/sec$). Figure 3.5 is a schematic of the variations of the nuclei concentration in the High Speed Water Tunnel. After two hours of air injection, the nuclei concentration was increased from $1.2cm^{-3}$ to $11.8cm^{-3}$. However, the nuclei concentration decreased consistently with time during the experiments. After about four hours of cavitation experiments, the nuclei concentration decreased to about $0.8cm^{-3}$. We also note that the overnight rest of the tunnel also increased the nuclei population in the High Speed Water Tunnel. After an overnight rest, the nuclei concentration increased from $0.8cm^{-3}$ to $4.64cm^{-3}$. A possible explanation is that during the overnight rest, the extracted air dissolved into the water slowly.

The de-aeration system in the Low Turbulence Water Tunnel described in Chapter 2 was used to lower the air content in the tunnel water. As shown in Figure 3.7, de-aeration effectively reduced the nuclei population in the Low Turbulence Water Tunnel. The nuclei concentration decreased from $248cm^{-3}$ to $178cm^{-3}$ after two hours of de-aeration, and further decreased to $151cm^{-3}$ after another six hours of de-aeration. It is also noted that when the air content decreases, the effectiveness of de-aeration goes down. During the first two hours of de-aeration the nuclei concentration decreased by 28%, but the nuclei concentration decreased by only 15% after the next six hours of de-aeration.

In the High Speed Water Tunnel, de-aeration was effected by running the water tunnel at a low speed ($U \approx 2m/sec$) and at a low pressure ($3.4kPa$). This seemed to work well.

After running for two days, the nuclei concentration in the water was about $1cm^{-3}$, which was much lower than what could be achieved in the Low Turbulence Water Tunnel.

3.4 Changes in the Nuclei Population with Cavitation Development on the Headform

The nuclei population in the Low Turbulence Water Tunnel varied with the tunnel operating condition and with the cavitation development on the headform in the working section. However, no significant changes in the nuclei population were observed in the High Speed Water Tunnel when the tunnel operating condition was changed.

The changes in the free stream nuclei concentration in the Low Turbulence Water Tunnel with the tunnel operating condition are shown in Figure 3.9, where the nuclei concentration is plotted against the cavitation number. Clearly, for a given cavitation number, the free stream nuclei concentration varied substantially. At the same cavitation number, the nuclei concentration could vary by more than $100cm^{-3}$. Despite these variations, a basic trend is evident, namely that the free stream nuclei concentration increases as cavitation number is decreased.

In the analytical model developed in Chapter 5, it will be shown that the cavitation event rate depends not only on the free stream nuclei concentration, but also on the shape of the nuclei number density distribution. Experimentally, it was observed that both the magnitude and shape of the nuclei distribution varied with the tunnel operating condition, the air content and the previous history of operation. By comparing nuclei number density distributions at various cavitating conditions, we may observe the effect of the nuclei number

density distribution on the cavitation event rate (or vice versa). We present the changes in the upstream nuclei population in the Low Turbulence Water Tunnel at different cavitation numbers in Figure 3.10 and the changes in the nuclei number density distribution at the same cavitation number but at different cavitation event rates in Figure 3.11. Note that most of the changes in the shape of the free stream nuclei number density distribution occur for nuclei in the size range above $15\mu m$ in both figures. An increase in the nuclei population in this range results in a major increase in the event rate. There is little change in the number of nuclei smaller than $15\mu m$ when the cavitation number is changed or the event rate changes.

During the cavitation experiments in the Low Turbulence Water Tunnel, cavitation inception occurred at about $\sigma_i = 0.60$. It is noted in Figure 3.9 that the free stream nuclei concentration exhibits a significant increase when cavitation number is decreased below 0.60. This implies that cavitation itself leads to an increase in the free stream nuclei concentration as is often surmised. This is probably the explanation for the cavitation hysteresis effect observed by Holl and Treaster (1966).

In the High Speed Water Tunnel, as mentioned before, the tunnel running time is the dominant effect. Little change in the nuclei population was observed as cavitation number was changed or the cavitation on the headform changed. Even when the cavitation on the headform surface became fully attached, there was very little change in the free stream nuclei population.

3.5 Conclusions

We can draw the following conclusions from these investigations of the nuclei population dynamics in the Low Turbulence Water Tunnel and High Speed Water Tunnel at Caltech.

Substantial differences in the nuclei number density distribution were found between these two tunnels. Although the shapes of the distributions are similar, the differences in the magnitude can be as much as two orders. Many researchers have measured nuclei number density distributions in facilities around the world and observed a wide range of nuclei number density distributions. Figure 3.12 presents comparisons of the measured nuclei number density distributions in the Low Turbulence Water Tunnel and the High Speed Water Tunnel with nuclei distributions in other facilities and in the ocean (Peterson, 1972, Feldberg and Shlemenson, 1973, Peterson *et al.*, 1975, Keller and Weitendorf, 1976, Arndt and Keller, 1976, Gates and Bacon, 1978, and Cartmill and Su, 1993). The typical nuclei concentration in the Low Turbulence Water Tunnel is about $100cm^{-3}$; while the typical nuclei concentration in the High Speed Water Tunnel is about $1cm^{-3}$. Billet (1985) and Gindroz and Billet (1994) presented useful reviews of the subject of nuclei concentrations and distributions. They found that for de-aerated water, typical concentrations are of the order of $20cm^{-3}$ with sizes ranging from about $5\mu m$ to about $200\mu m$. We conclude that the Low Turbulence Water Tunnel is nuclei rich and the High Speed Water Tunnel is nuclei poor. Therefore, comparative experiments in these two tunnels should provide a good evaluation of the nuclei population effects on cavitation.

Although it has been found that the nuclei populations in different facilities are quite different, it has often been assumed that the nuclei population in a given facility remains relatively constant during a cavitation experiment. In the present investigations, dramatic

changes in the nuclei population in the same tunnel were found in the Low Turbulence Water Tunnel and in the High Speed Water Tunnel. The changes in the nuclei population can be as much as an order of magnitude and could be influenced by the tunnel design, the air content, the tunnel running time, the tunnel operating condition and the cavitation in the working section. Therefore, we highly recommend that the nuclei population be monitored when carrying out cavitation experiments.

The most dominant effect on the nuclei population comes from the tunnel design. The Low Turbulence Water Tunnel and the High Speed Water Tunnel differ in that the High Speed Water Tunnel has a resorber. Consequently, the nuclei population dynamics in these two tunnels showed very different characteristics. In the Low Turbulence Water Tunnel, the tunnel operating condition has significant effect on the nuclei population. Nuclei populations changed constantly with the tunnel operating condition. On the other hand, the nuclei population in the High Speed Water Tunnel was almost independent of the tunnel operating condition. Since the tunnel design and the flow fields are quite complex, we can not claim that these trends would necessarily occur in other tunnels. But the following observations seem to have generality.

In a tunnel which has a resorber or a device to suppress the free air bubbles in the water before the flow re-enters the working section, the nuclei population probably will not be influenced by the tunnel operating condition, but will decrease with the tunnel running time regardless of the tunnel operating condition. On the other hand, if a tunnel does not have such a device, the nuclei population in the tunnel water will depend on the operating condition, and running the tunnel at different cavitation numbers will have different effects on the nuclei concentration. At low cavitation numbers, the concentration increases

within a couple of minutes; at intermediate cavitation numbers, the nuclei concentration remains almost constant and at large cavitation numbers, the nuclei concentration decreases over long time. There appears to be an asymptotic nuclei concentration for each specific operating condition.

De-aeration can decrease the nuclei population while air injection can increase the nuclei population. But the effectiveness depends heavily on the flow rate at which de-aeration or air injection is performed. The air injection and de-aeration used in the High Speed Water Tunnel are very effective; however, in the Low Turbulence Water Tunnel, the de-aeration system is less effective and the air injection system had very little effect on the nuclei population due to the very small flow rate in the air injection system.

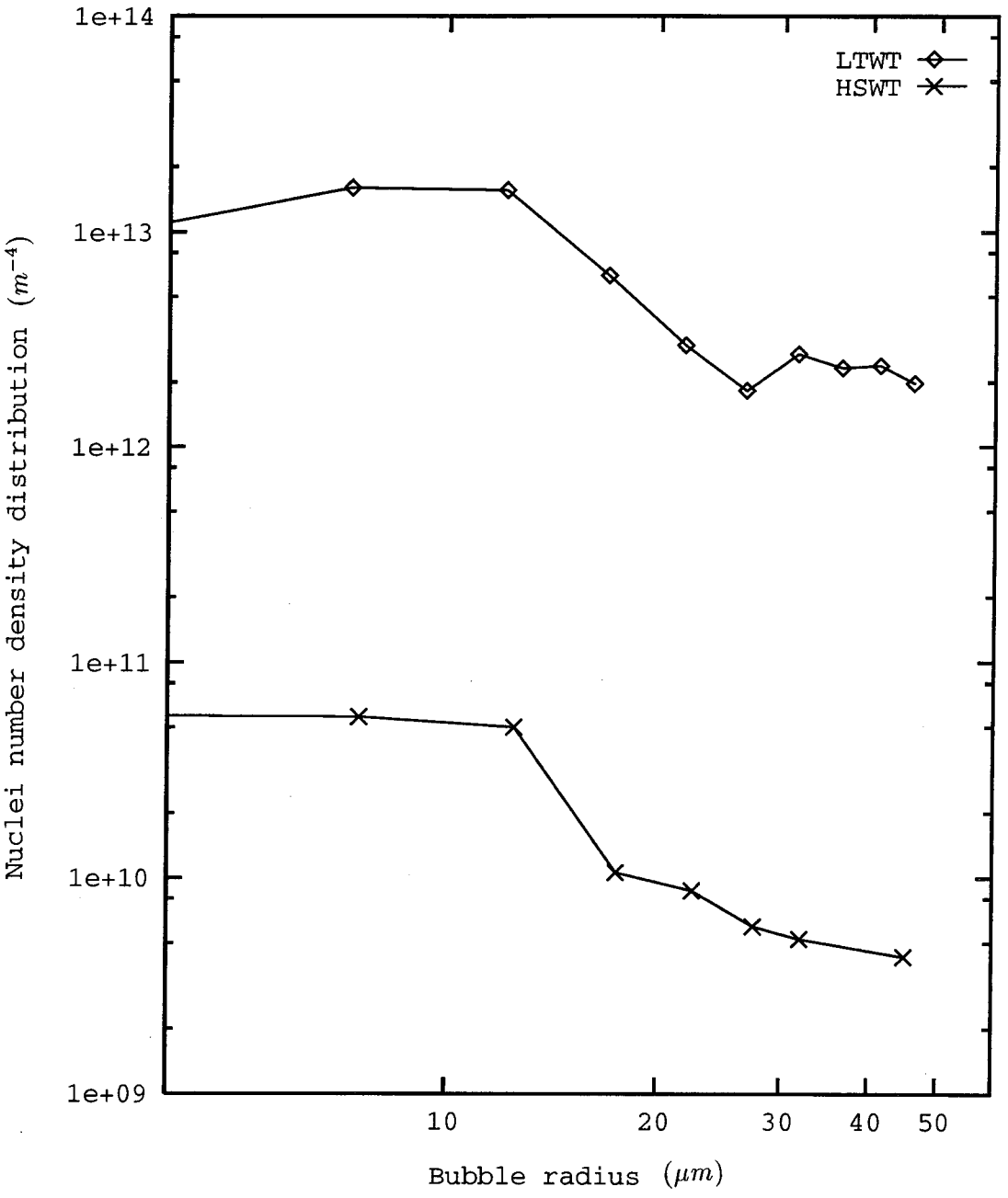

Figure 3.1: A comparison of the nuclei number density distributions in the Low Turbulence Water Tunnel ($\diamond$) and the High Speed Water Tunnel ($\times$).

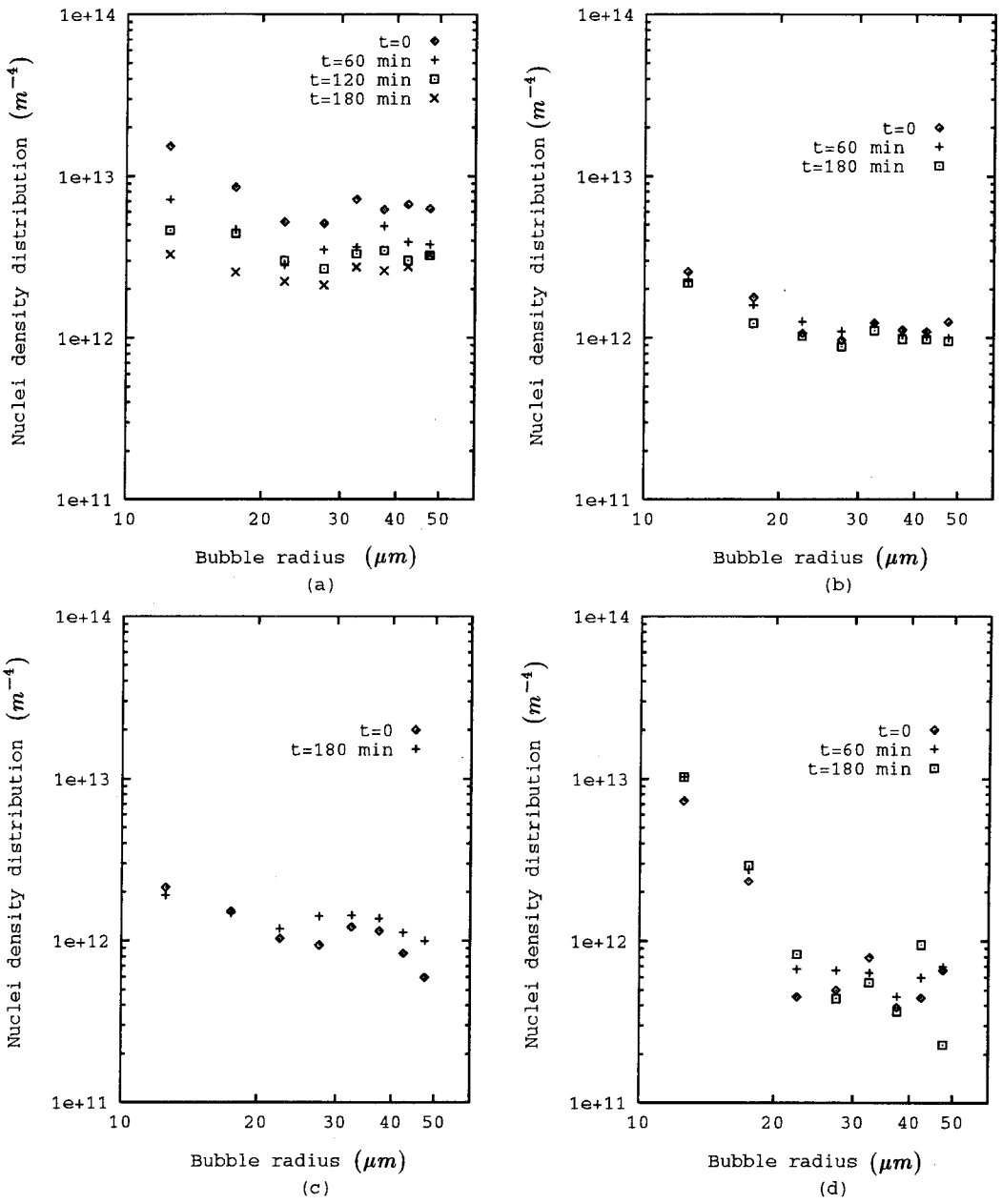

Figure 3.2: The effect of water tunnel running time on the free stream nuclei distributions in the Low Turbulence Water Tunnel at different tunnel working conditions. (a) $U = 3.16m/sec, p = 104kPa, \sigma = 22.7$ (b) $U = 5.13m/sec, p = 98kPa, \sigma = 7.63$ (c) $U = 5.13m/sec, p = 40kPa, \sigma = 3.01$ (d) $U = 8.00m/sec, p = 77kPa, \sigma = 2.34$.

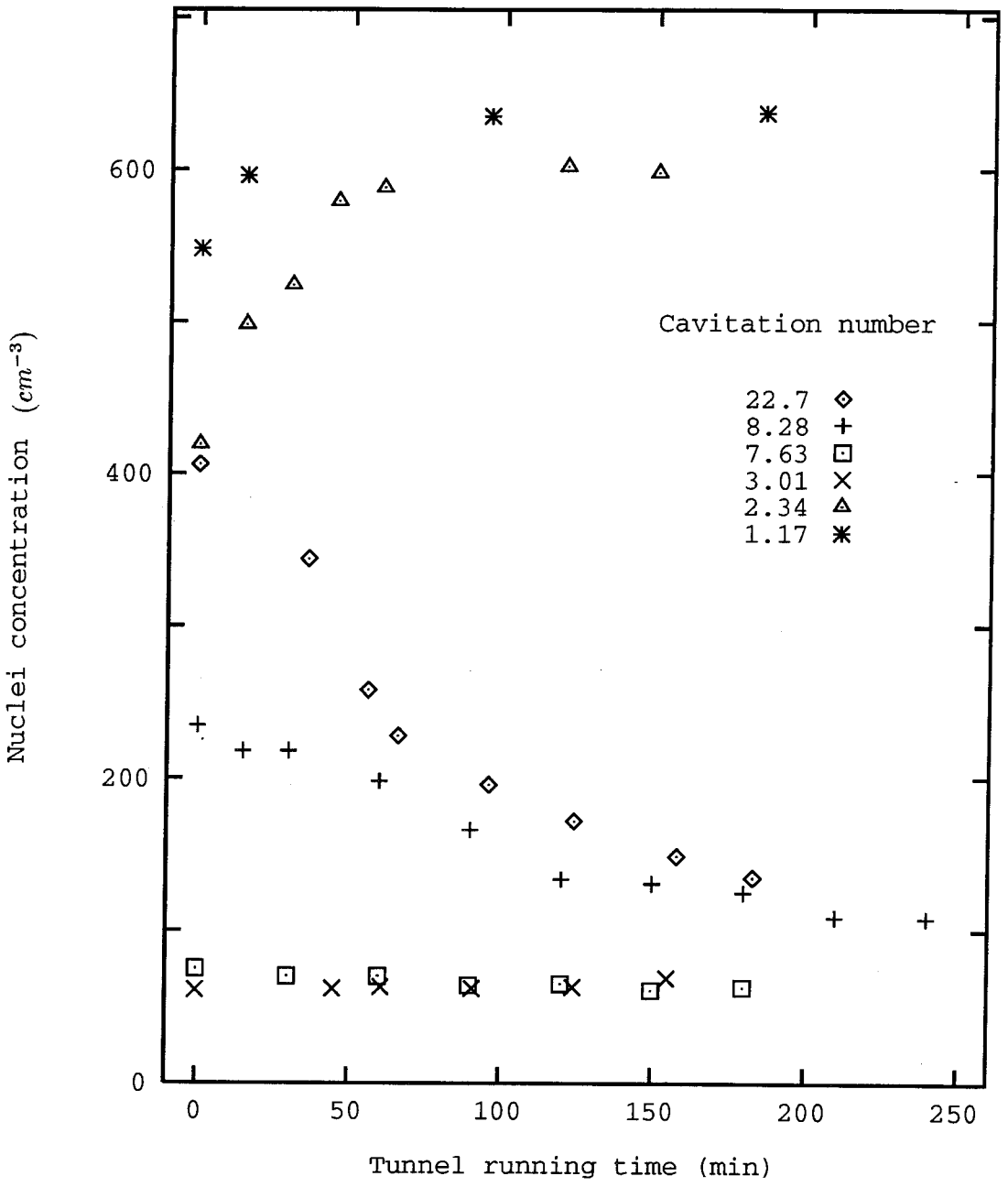

Figure 3.3: Changes in the nuclei concentrations with the tunnel running time in the Low Turbulence Water Tunnel at Caltech at six different cavitation numbers.

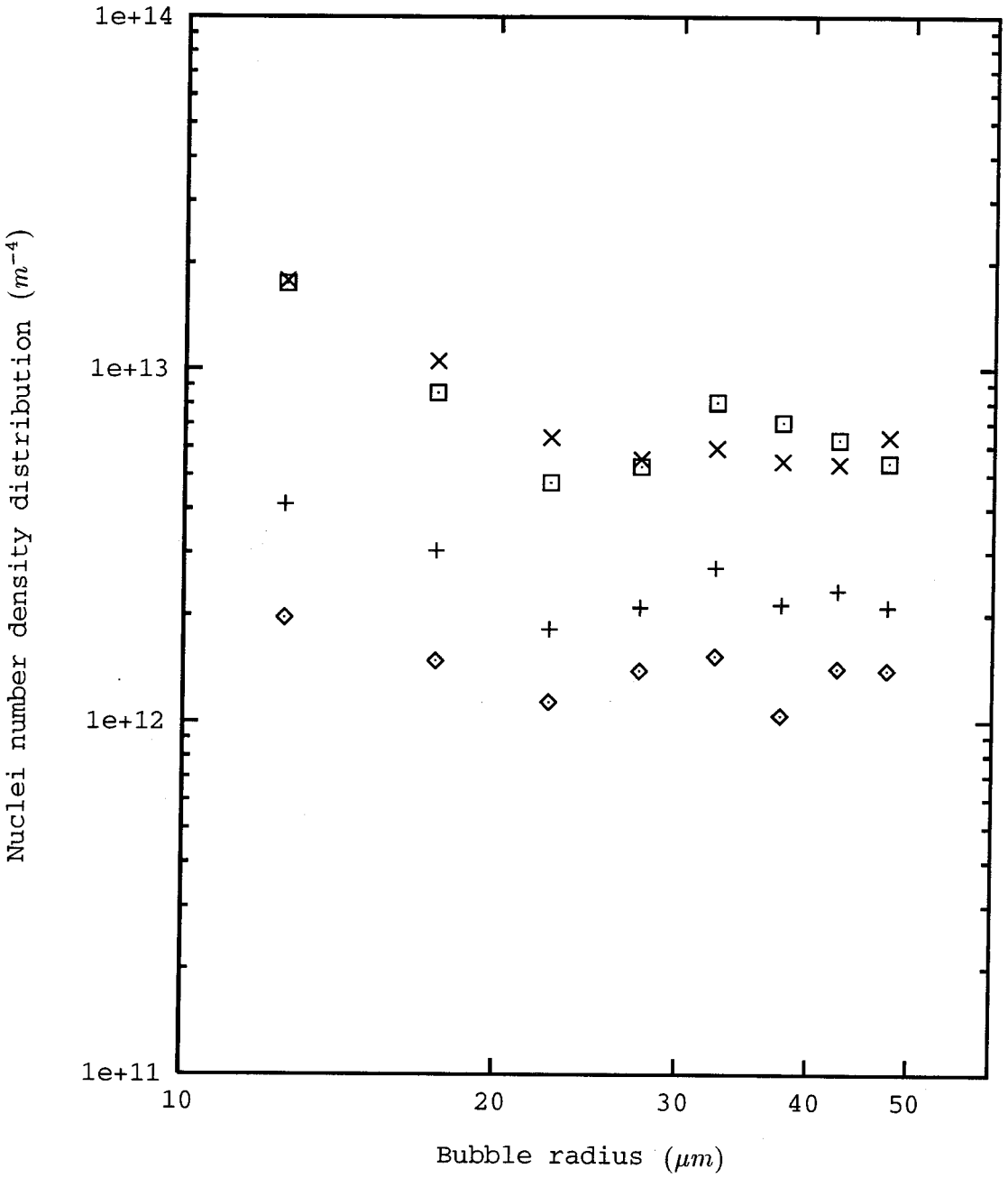

Figure 3.4: Changes in the free stream nuclei distribution before and after running the water tunnel at $U = 8.9m/sec\,\sigma = 1.72$ for 10 minutes. $\sigma = 22.9$ ($\diamond$) before; ($\times$) after; $\sigma = 7.71$, (+) before and ($\Box$) after.

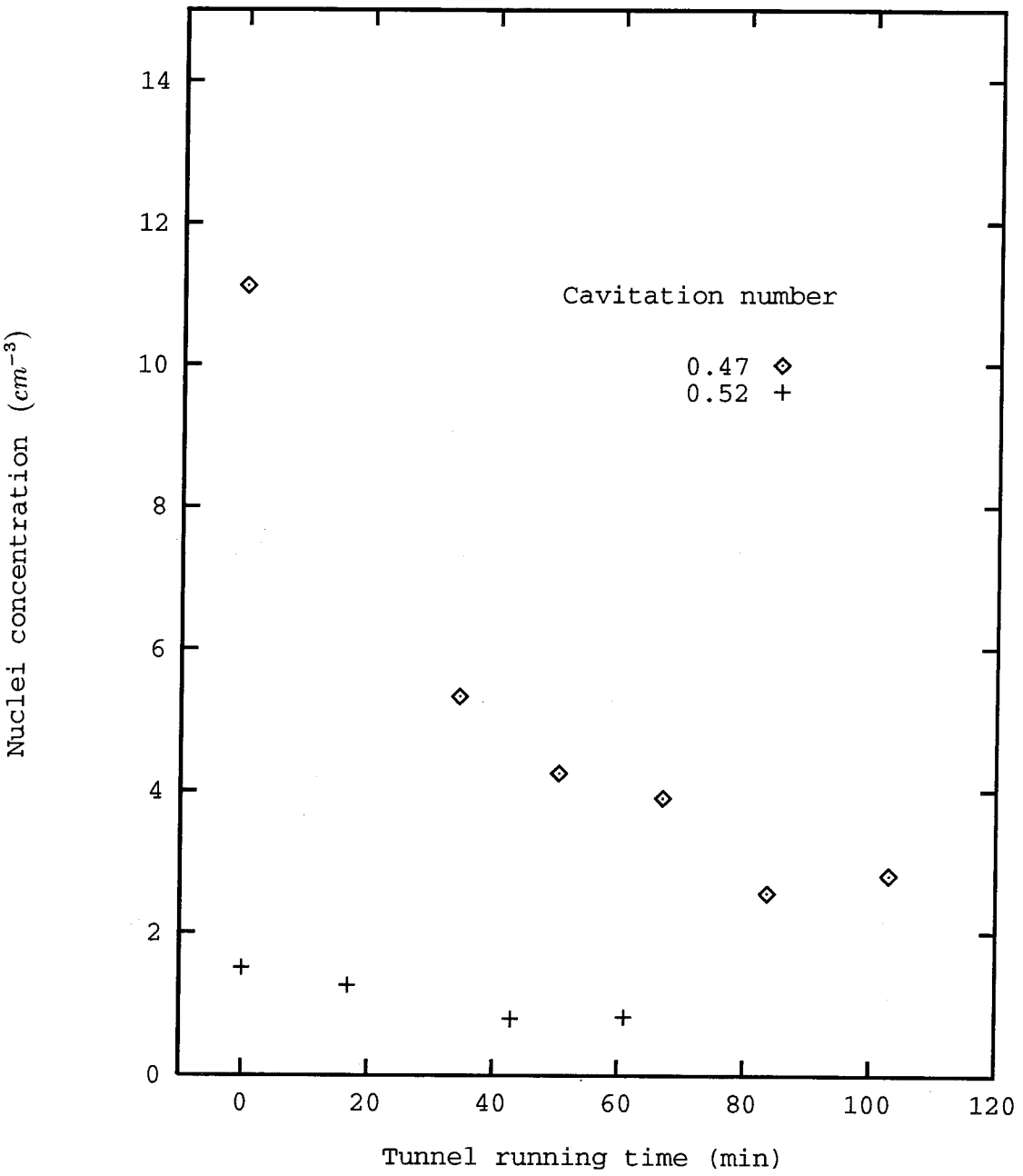

Figure 3.5: Changes in the nuclei concentration with the tunnel running time in the High Speed Water Tunnel at Caltech at two different cavitation numbers: $\sigma = 0.47$ ($\diamond$) and $\sigma = 0.52$ (+).

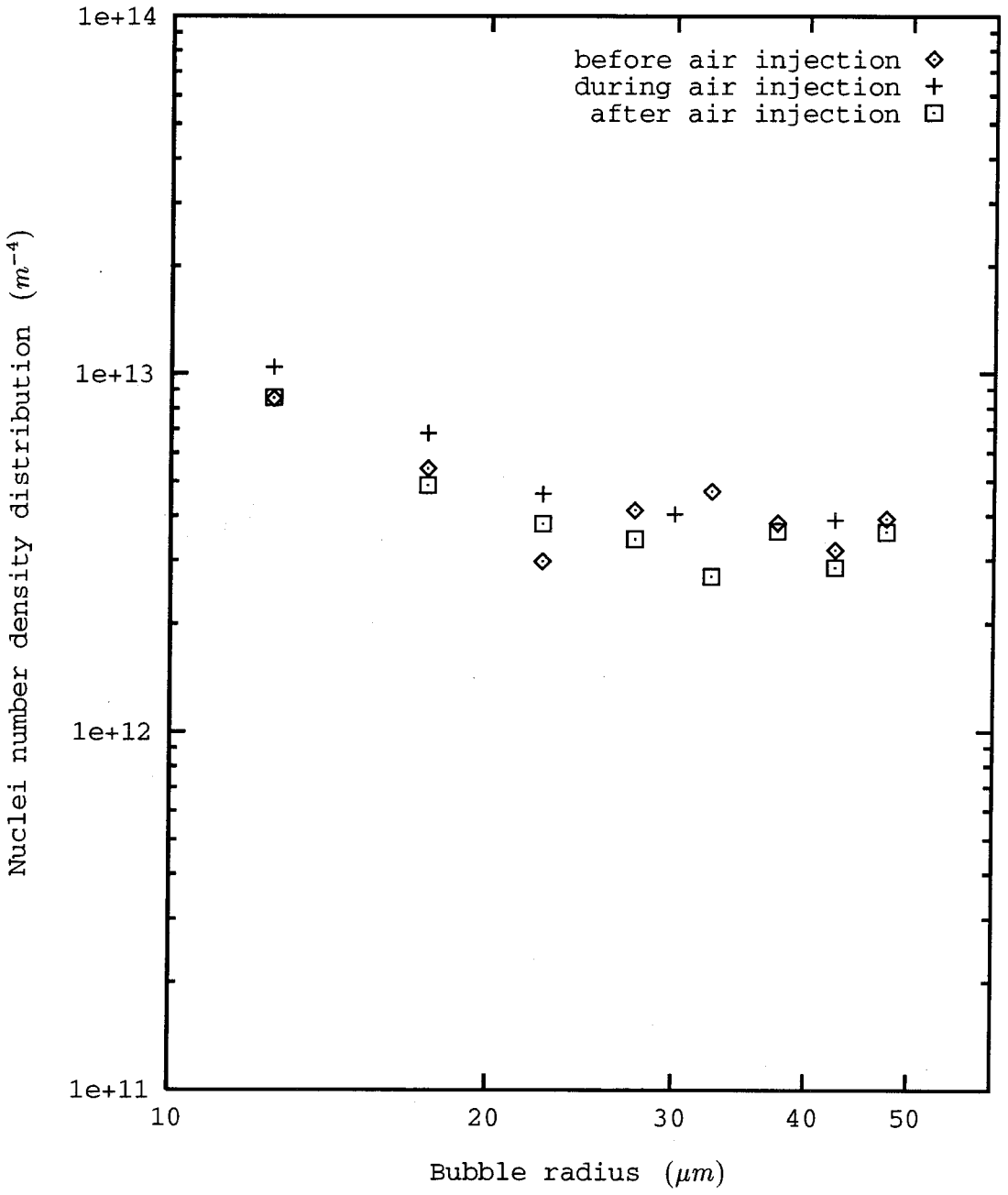

Figure 3.6: The effect of the air injection on the free stream nuclei distribution in the Low Turbulence Water Tunnel at $U = 3.16m/sec$, $p = 109kPa$, $\sigma = 23.66$.

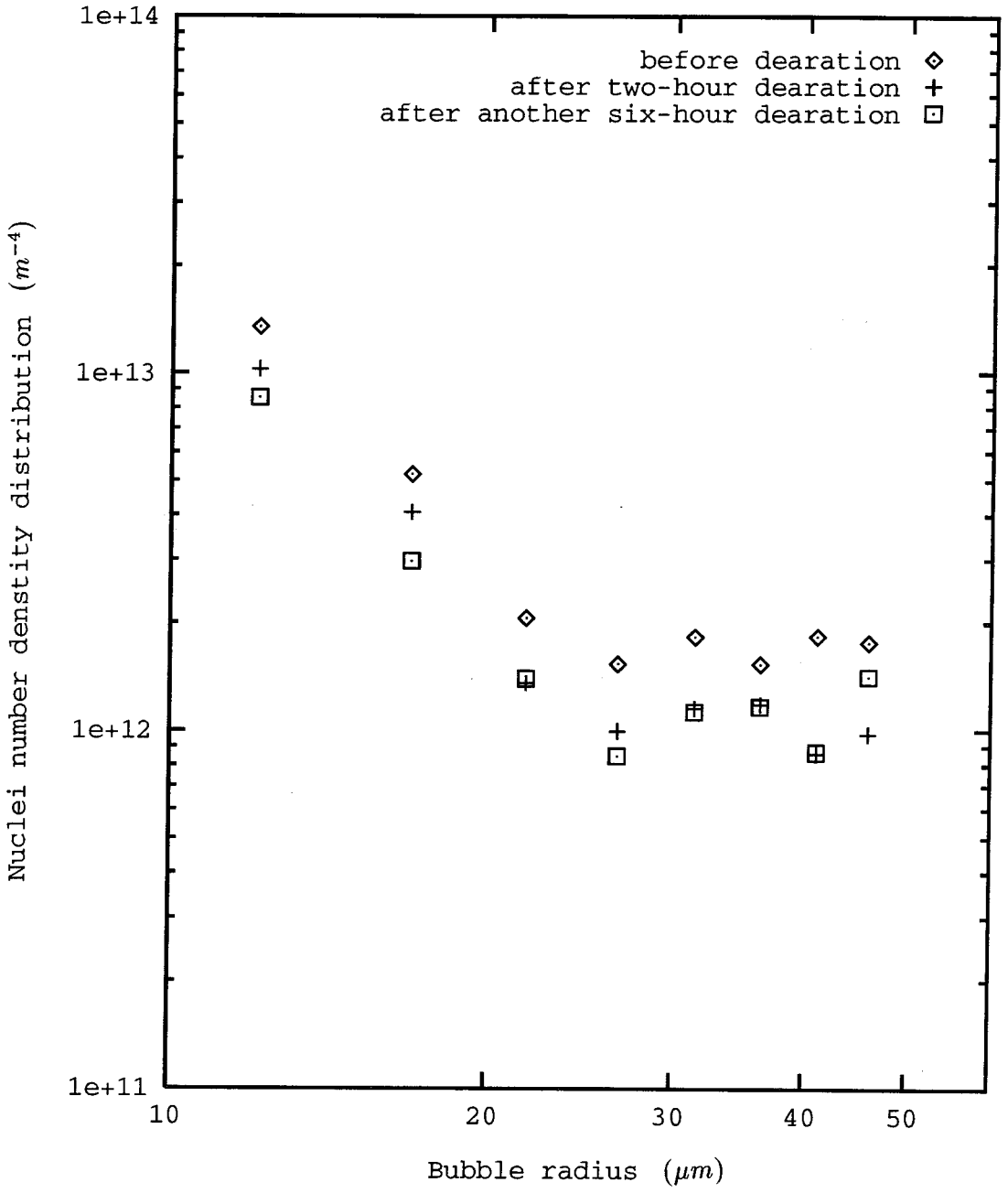

Figure 3.7: The effect of the de-aeration on the free stream nuclei distribution in the Low Turbulence Water Tunnel at $U = 5.12m/sec$, $p = 97kPa$, $\sigma = 7.51$.

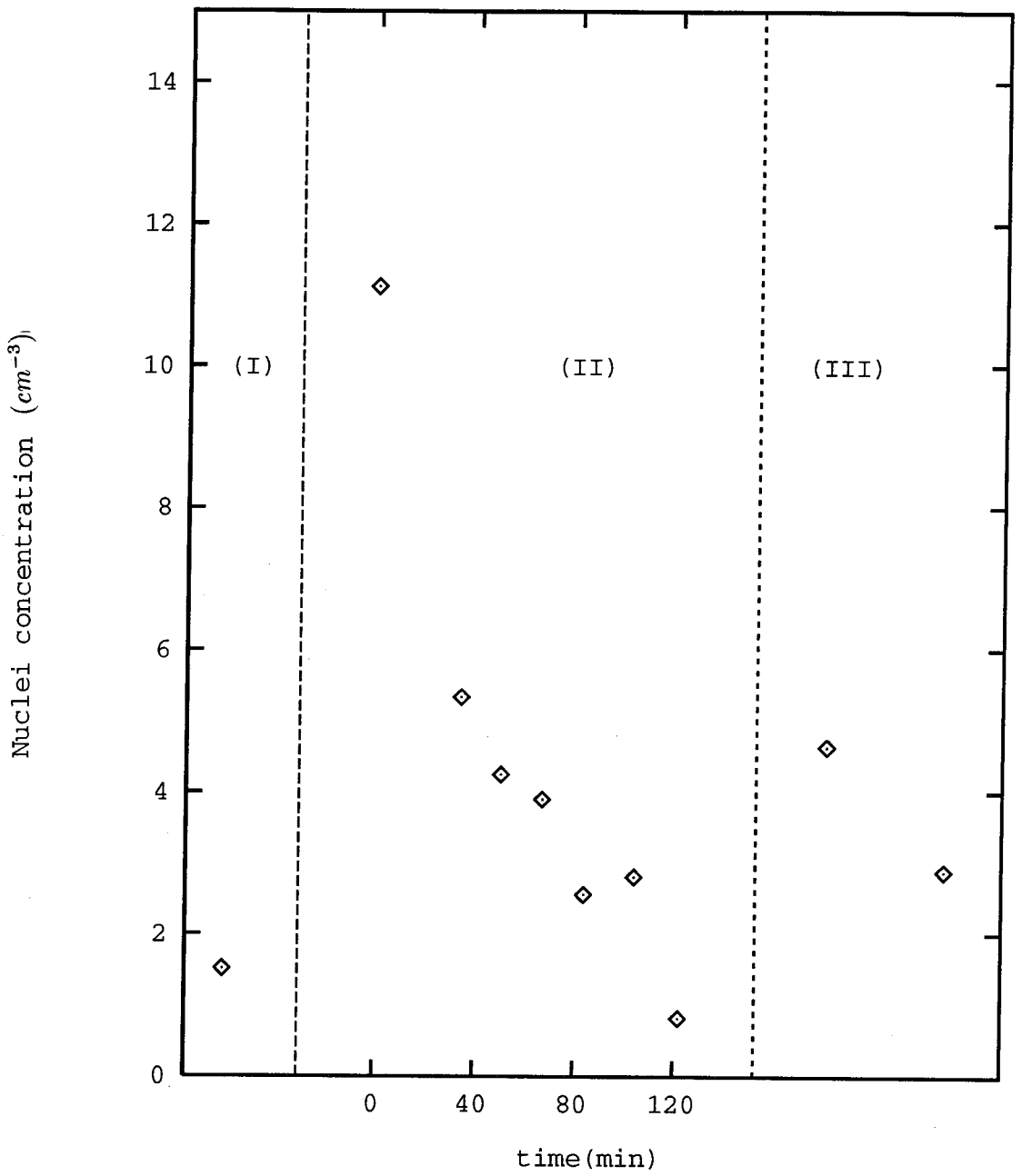

Figure 3.8: Changes in the upstream nuclei concentrations before and after air injection in the High Speed Water tunnel. (I) nuclei concentration before air injection; (II) after air injection, changes in the nuclei concentration with the tunnel running time, and (III) nuclei concentration after a night rest of the tunnel.

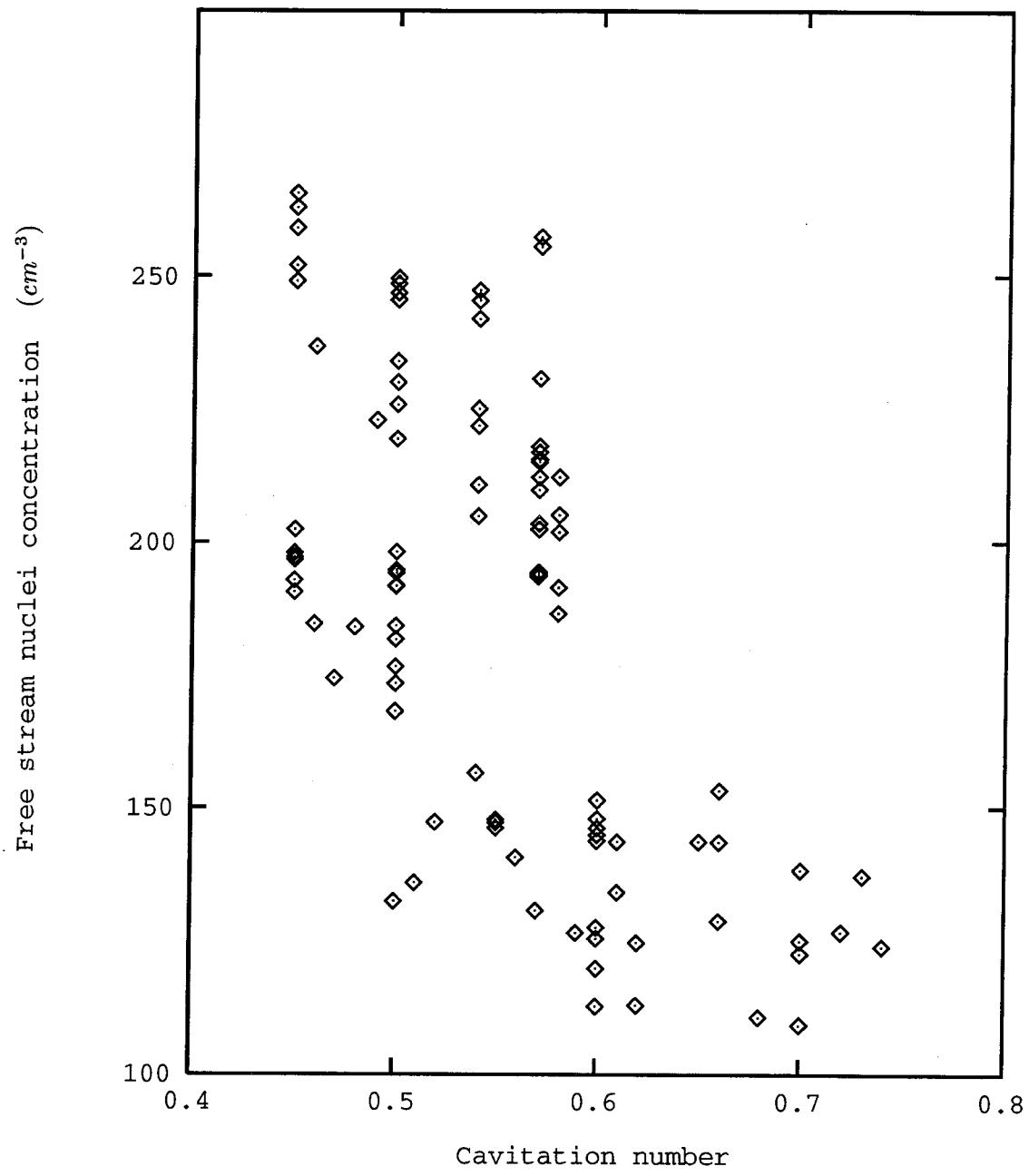

Figure 3.9: Changes in the free stream nuclei concentration in the Low Turbulence Water Tunnel with tunnel operating conditions (cavitation number) at $U = 9m/sec.$

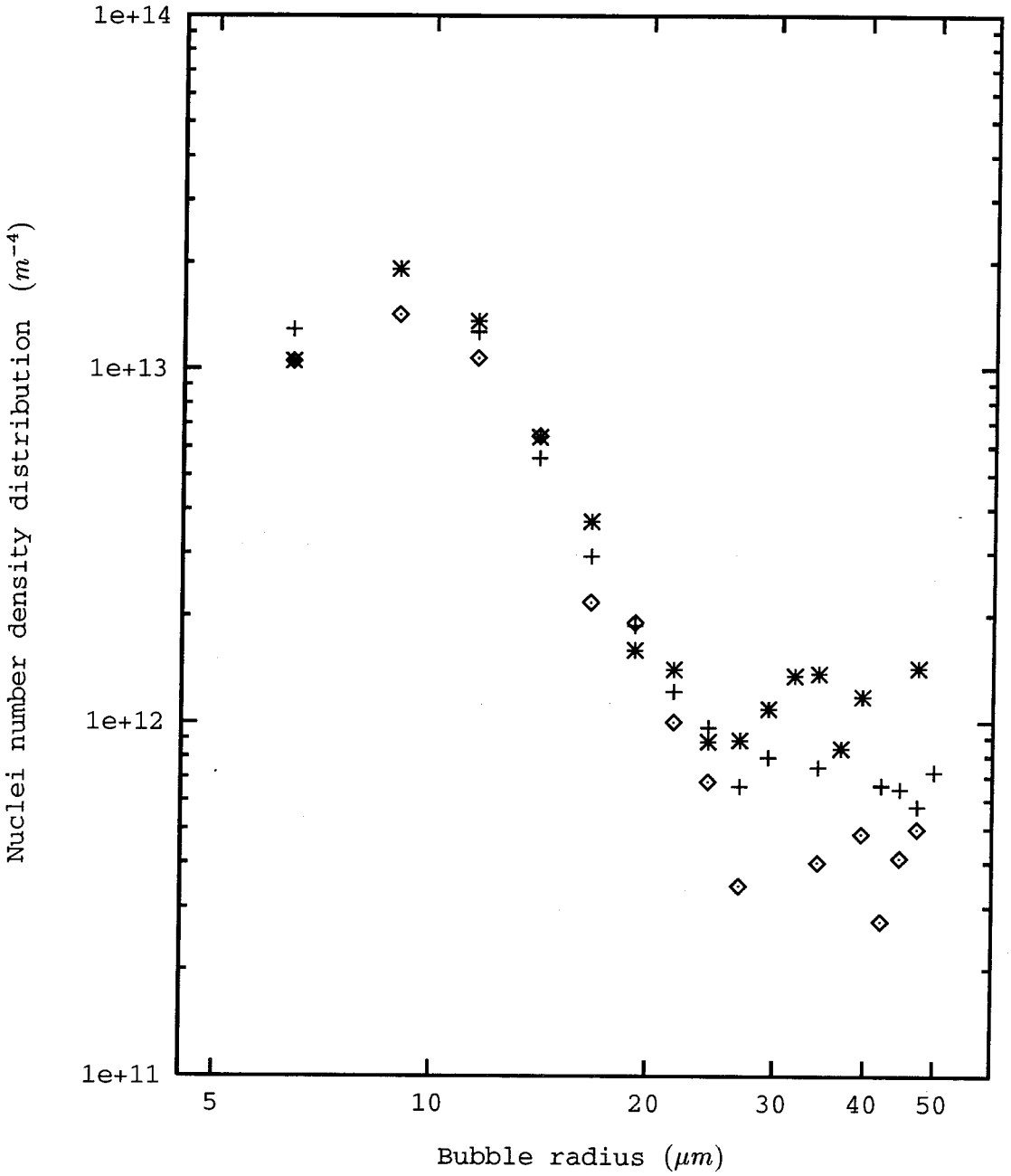

Figure 3.10: Changes in the free stream nuclei number density distribution in the Low Turbulence Water Tunnel at different cavitation numbers, $\sigma = 0.57\,(\diamond)$; $\sigma = 0.50\,(+)$ and $\sigma = 0.45\,(*)$ and at velocity $U = 9.0m/sec.$

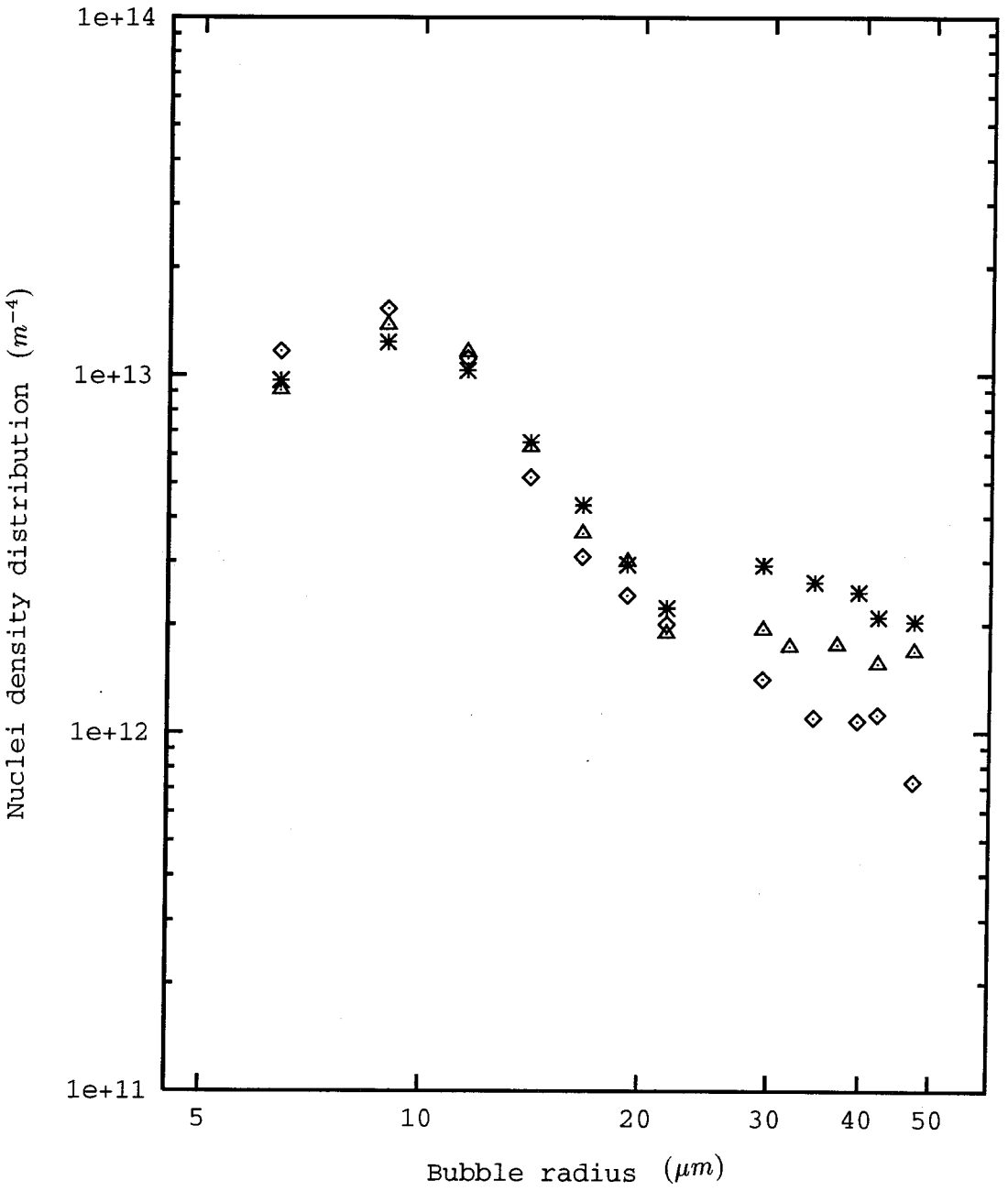

Figure 3.11: Changes in the free stream nuclei number density distribution in the Low Turbulence Water Tunnel at a cavitation number of $\sigma = 0.57$ and a velocity of $U = 9.0m/sec$, but at different cavitation event rates: $E = 3sec^{-1}(\diamond)$; $E = 14sec^{-1}(\triangle)$; $E = 34sec^{-1}(*)$.

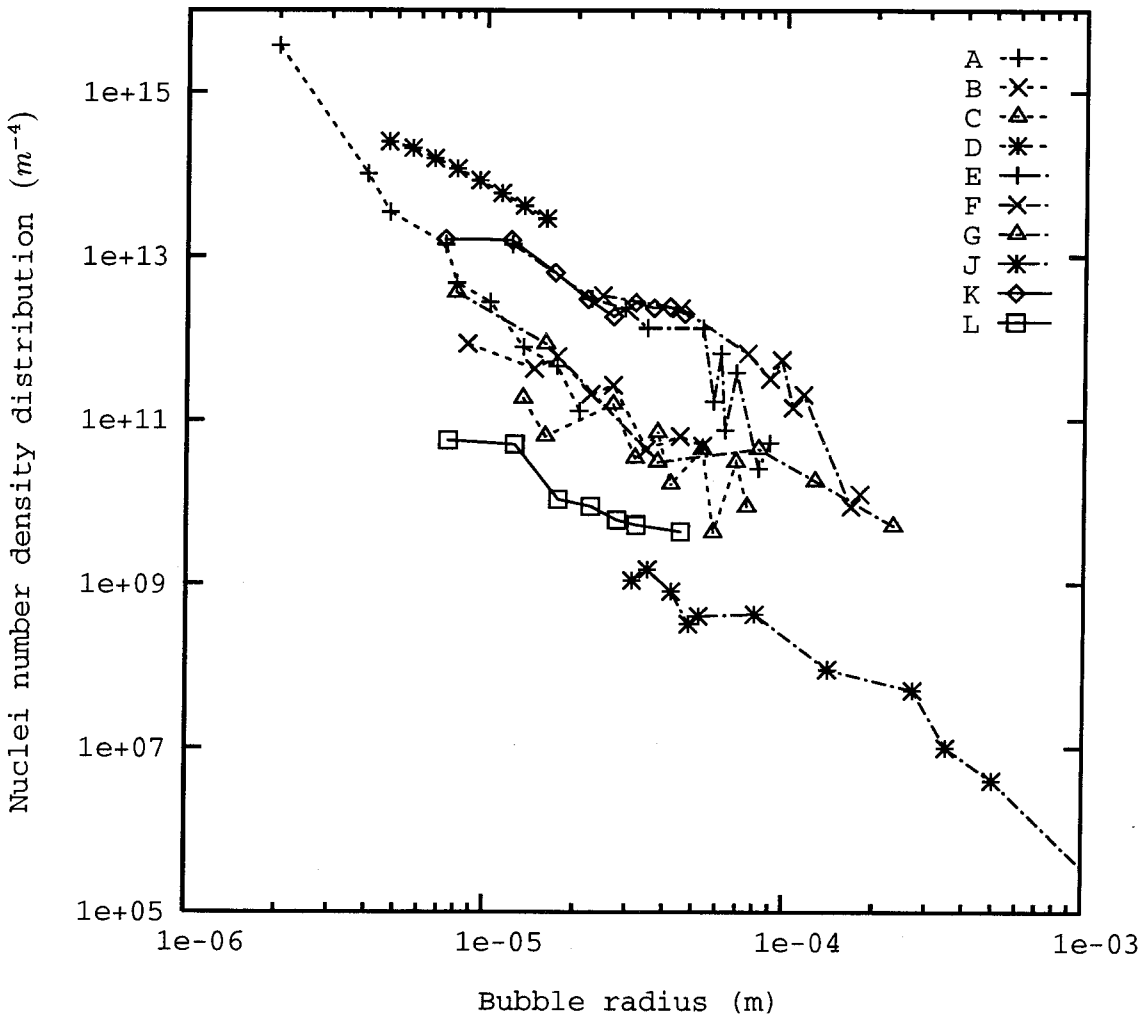

Figure 3.12: A comparison of the nuclei number density distributions in the Low Turbulence Water Tunnel and the High Speed Water Tunnel with measurements in other facilities and in the ocean. (**A**): Peterson *et al.* (1975), light scattering method, (**B**): Peterson *et al.* (1975), holographic method, (**C**): Peterson (1972), (**D**): Feldberg and Schlemenson (1973), (**E**): Arndt and Keller (1976), (**F**): Keller and Weitendorf (1976), (**G**): Gates and Bacon (1978), (**J**): Cartmill and Su (1993), (**K**): present study, LTWT, (**L**): present study, HSWT.

Chapter 4

Observation of Cavitation Event Rate and Noise

4.1 Cavitation Event Rate

Traveling bubble cavitation event rates on a Schiebe headform were observed while the free stream nuclei populations were simultaneously measured in both the Low Turbulence Water Tunnel and the High Speed Water Tunnel at different tunnel operating conditions. Very different cavitation phenomena were observed in these two tunnels. In the Low Turbulence Water Tunnel, traveling bubble cavitation inception occurred at a cavitation number about 0.6 and fully attached cavitation occurred at a cavitation number about 0.45. However, in the High Speed Water Tunnel, traveling bubble cavitation inception occurred at a cavitation number about 0.53 and the cavitation became fully attached at a cavitation number about 0.47, leaving a very narrow range in which traveling bubble cavitation occurred. The delay in cavitation inception in the High Speed Water Tunnel is probably due to the fact that

fewer nuclei are convected to the low pressure region under the same operating condition since the High Speed Water Tunnel has fewer nuclei than the Low Turbulence Water Tunnel. However, the appearance of fully attached cavitation at a larger cavitation number in the High Speed Water Tunnel is not fully understood.

Figure 4.1 shows the variation of cavitation event rates with the cavitation number in the Low Turbulence Water Tunnel. The event rates are distinguished for various nuclei concentration ranges. As shown in the figure, the cavitation event rate increased dramatically as the cavitation number was decreased. Note, however, that the event rate can vary by as much as a decade at the same cavitation number. Clearly, larger free stream nuclei concentrations correspond to larger cavitation event rates.

We chose to define the cavitation inception number, σ_i, as the cavitation number for which a certain event rate (say $10 events/sec$) occurs. Then, as seen in figure 4.1, the cavitation inception number increases with the free stream nuclei concentration. At the typical criterion of $10 events/sec$, the cavitation inception number, σ_i, was 0.55 when the nuclei concentration was less than $150 cm^{-3}$. On the other hand, cavitation inception occurred at $\sigma_i = 0.57$ when the concentration was between $200 cm^{-3}$ and $250 cm^{-3}$, and at $\sigma_i = 0.60$ when the nuclei concentration was above $250 cm^{-3}$.

The effect of the upstream nuclei population on the cavitation event rate is also demonstrated in Figure 4.2, where the cavitation event rate is plotted against the upstream nuclei concentration. At two typical cavitation numbers ($\sigma = 0.45$ and $\sigma = 0.57$), the cavitation event rate increased as the free stream nuclei concentration increased. At $\sigma = 0.45$, as the free stream nuclei concentration increased from $191 cm^{-3}$ to $266 cm^{-3}$, the event rate increased from $589 sec^{-1}$ to $891 sec^{-1}$. At $\sigma = 0.57$, as the free stream nuclei concentration

increased from $194cm^{-3}$ to $257cm^{-3}$, the event rate increased from $10.3sec^{-1}$ to $52.4sec^{-1}$. Note that even at the same cavitation number and with the same nuclei concentration, the event rate still varied considerably. This may be due to the differences in the distribution of nuclei size, which is also an important factor in determining the event rate. As demonstrated in Figure 3.11, variations in the shape of the nuclei size distribution in the range above $15\mu m$ lead to variations in the cavitation event rate.

Figure 4.3 shows the changes in the cavitation event rate with cavitation number in the High Speed Water Tunnel. Because the nuclei concentration changed substantially before and after the air injection, the event rates at the same cavitation number changed substantially. Consequently, cavitation inception occurred at quite different cavitation numbers. As expected, the cavitation event rate increased with the upstream nuclei concentration. At a velocity of $9.4m/sec$ and a nuclei concentration of $0.80cm^{-3}$ before the air injection, cavitation inception occurred at a cavitation number of 0.46. After the air injection, the nuclei concentration raised to $12cm^{-3}$. Cavitation inception occurred at a cavitation number of 0.52. It should be kept in mind that in the Low Turbulence Water Tunnel, cavitation inception number was about 0.57, when the nuclei concentration was about $100cm^{-3}$. It should also be noted that the maximum cavitation event rate in the High Speed Water Tunnel was less than $50sec^{-1}$; attached cavitation occurred soon after traveling bubble cavitation inception. This implies that attached cavitation occurs more readily when the nuclei population is low. Li and Ceccio (1994) observed a similar phenomenon on a cavitating hydrofoil. In their observations, when the nuclei concentration in the water was high, traveling bubble cavitation occurred before attached cavitation was observed. But when the nuclei concentration was low, no traveling bubble cavitation was observed before attached cavita-

tion occurred. They ascribe the cause of this phenomenon to laminar boundary separation on the hydrofoil. However, we are not sure about the cause on the Schiebe headform since it does not exhibit laminar boundary layer separation in the region of concern here.

One should also note in Figure 4.3, by comparing the event rates at $U = 9.4m/sec$ and $U = 14.5m/sec$, that, at the same nuclei concentration level ($1.6cm^{-3} < C < 3.0cm^{-3}$), the cavitation event rate decreased with increasing tunnel velocity, which is the inverse of what would be expected. A comparison of typical nuclei number distributions at these two velocities is presented in Figure 4.4. At the same cavitation number ($\sigma = 0.54$), the nuclei number distributions were quite similar. All the numerical and analytical simulations (Ceccio and Brennen, 1992, Meyer *et al.*, 1992, and Liu *et al.*, 1993) predict that the event rate increases with oncoming velocity, provided that the nuclei population remains the same. This velocity effect on the cavitation event rate was also observed by Kuhn de Chizelle *et al.* (1992). Since they were unable to measure the nuclei population in the oncoming flow, Kuhn de Chizelle *et al.* speculated that the free nuclei population was decreased by the increase in the tunnel pressure at a higher speed (for the same cavitation number). The investigations of nuclei population dynamics in a water tunnel by Liu *et al.* (1993) support their speculations. However, the current data shows that the event rate decreases with an increasing tunnel speed even when the nuclei concentrations are at the same level. This phenomenon is not fully understood. A possible explanation is that the PDA mistakenly counted more solid particles as microbubbles at the higher tunnel velocities. Since the population of solid particles increased with speed, perhaps the number of microbubbles decreased even though the total nuclei concentration remained the same. It may also be the case that there exists some, as yet unrecognized, mechanism in the relation between the

nuclei population and the cavitation event rate.

The probability density distributions of the time between two events and of the bubble radius are shown in Figure 4.5 for two different cavitation numbers. At the larger cavitation number ($\sigma = 0.56$), the time between two events is more homogeneously distributed and the probability density of bubble radius has a peak in the small size range. On the other hand, at the lower cavitation number ($\sigma = 0.45$), there are very few smaller bubbles and the time between two events has a peak at a small value. In the analytical model developed later, we will demonstrate that the bubble size is inversely proportional to its off-body distance. This implies that at lower cavitation numbers, a nucleus with potential to cavitate but moving along a streamline which is farther above the surface has less chance to grow because of the increasing interaction with larger bubbles. Therefore, to quantitatively predict cavitation at lower cavitation numbers, the interaction between bubbles should be considered.

4.2 Observation of Cavitation Noise

Though the peak acoustic pressure generated by an individual cavitation event (individual traveling bubble) has been used by many researchers (for example, van der Meulen, 1980) to characterize cavitation noise intensity, it will be argued later in Chapter 6 that the acoustic emission from individual traveling bubble is better characterized by the cavitation pressure impulse, $I(r)$, which is defined as

$$I(r) = \int_{t1}^{t2} (p(t,r) - p_\infty)\, dt \tag{4.1}$$

where $p(t,r)$ and p_∞ are the local pressure and the upstream pressure respectively; t_1 and t_2 are the moments when $p(t,r) = p_\infty$.

The dimensionless impulse, I^*, is defined by

$$I^*(r) = \frac{4\pi}{\rho_L U r_H} I \tag{4.2}$$

where ρ_L is the liquid density; U is the flow velocity and r_H is the headform radius.

Figure 4.6 shows the dimensionless pressure impulse for individual cavitation events measured during the High Speed Water Tunnel experiments. We note that for all the tunnel velocities and upstream nuclei concentrations shown in the figure, the dimensionless pressure impulse first increases as the cavitation number is reduced. However, below a certain cavitation number, the dimensionless pressure impulse starts to decrease. This phenomenon was also observed by Ceccio and Brennen (1992) and Kuhn de Chizelle *et al.* (1992). Arakeri and Shangumanathan (1985) noticed that at low cavitation numbers, the interference effect is strong and the collapse of a bubble is poor over the entire frequency range, thus making the acoustic emission weaker. Also note in Figure 4.6 that at $U = 9.4m/sec$, the dimensionless pressure impulse is larger than at $U = 14.5m/sec$.

4.3 Conclusions

The cavitation event rate is mainly determined by the cavitation number. It increases dramatically as cavitation number is decreased. The free stream nuclei population also has significant effect on the event rate which increases with increasing nuclei concentration. The cavitation event rate can vary by as much as an order in magnitude at the same cavitation number due to the changes in the free stream nuclei population. Both the magnitude and the shape of the nuclei number density distribution are important. A larger nuclei population corresponds to a larger cavitation event rate. The changes in the nuclei size

range above $15\mu m$ especially can result in significant changes in the cavitation event rate. The cavitation inception number based on a certain event rate reflects these variations.

In the past, attempts to correlate the cavitation event rate and the nuclei population (Ceccio and Brennen, 1992, Meyer *et al.*, 1992 and Liu *et al.*, 1993b) have assumed, for lack of better knowledge, that the nuclei number distribution in a given facility has the same magnitude and shape, regardless of the extent of cavitation development on the headform. The present study has demonstrated that substantial changes in free stream nuclei population may occur during cavitation experiments. This causes substantial changes in the event rate. It follows that for more accurate evaluation of cavitation, changes in the nuclei population should be carefully monitored and included in any analytical model which attempts to correlate the cavitation event rate with the free stream nuclei population.

The acoustic emission from traveling bubble cavitation can be characterized by the acoustic impulse. Initially, the dimensionless acoustic pressure impulse increases as the cavitation number is decreased. However, as cavitation number decreases further, the dimensionless acoustic pressure impulse starts to decrease. At the same cavitation number, the dimensionless acoustic pressure impulse also increases as the tunnel velocity is decreased.

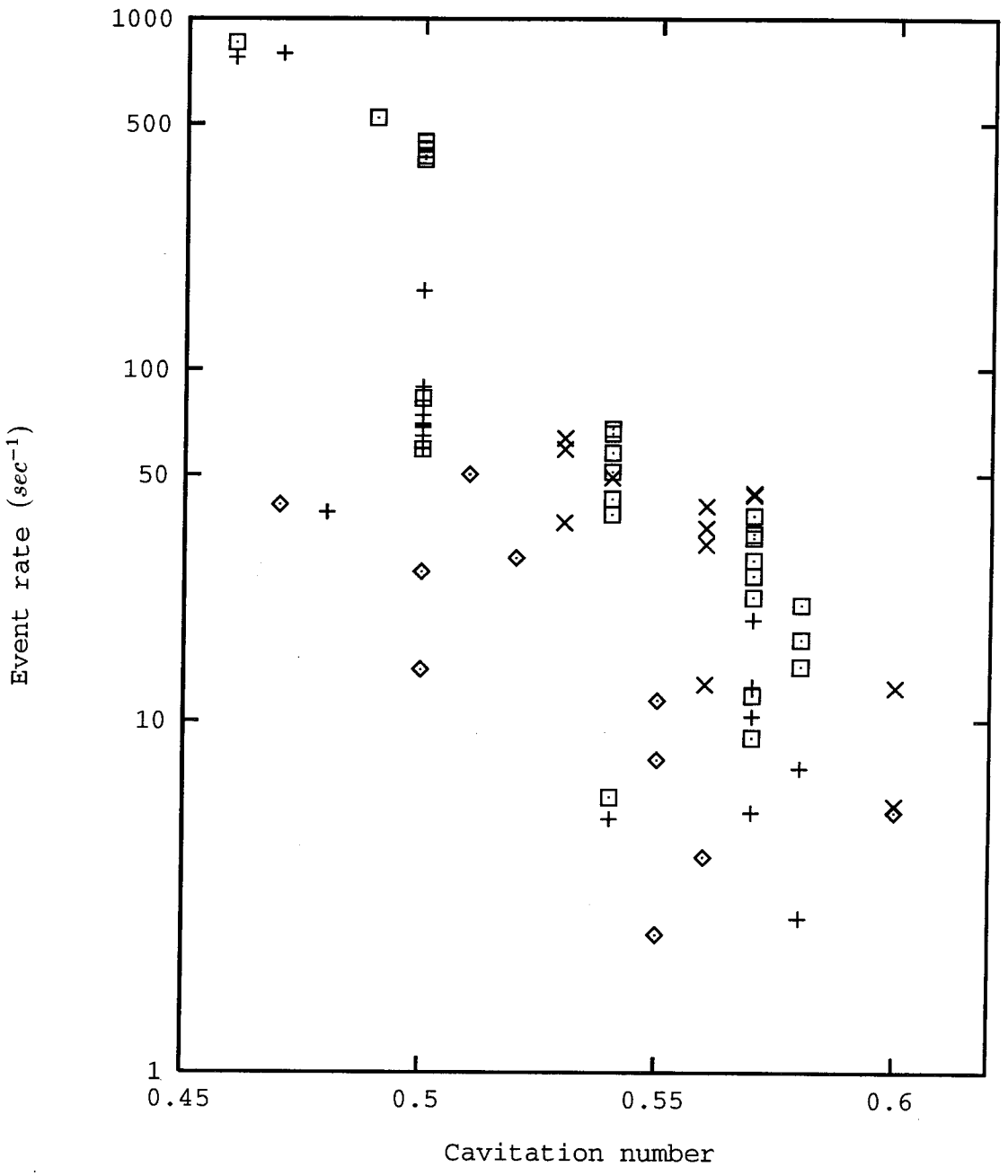

Figure 4.1: Variations of the cavitation event rate on a $5.08cm$ Schiebe body with cavitation number at $U = 9m/sec$ in the Low Turbulence Water Tunnel. The variations of event rates are distinguished for various ranges of free stream nuclei concentration, C, in (cm^{-3}): $C < 150$ ($\diamond$); $150 < C < 200$ ($+$); $200 < C < 250$ ($\square$) and $250 < C$ ($\times$).

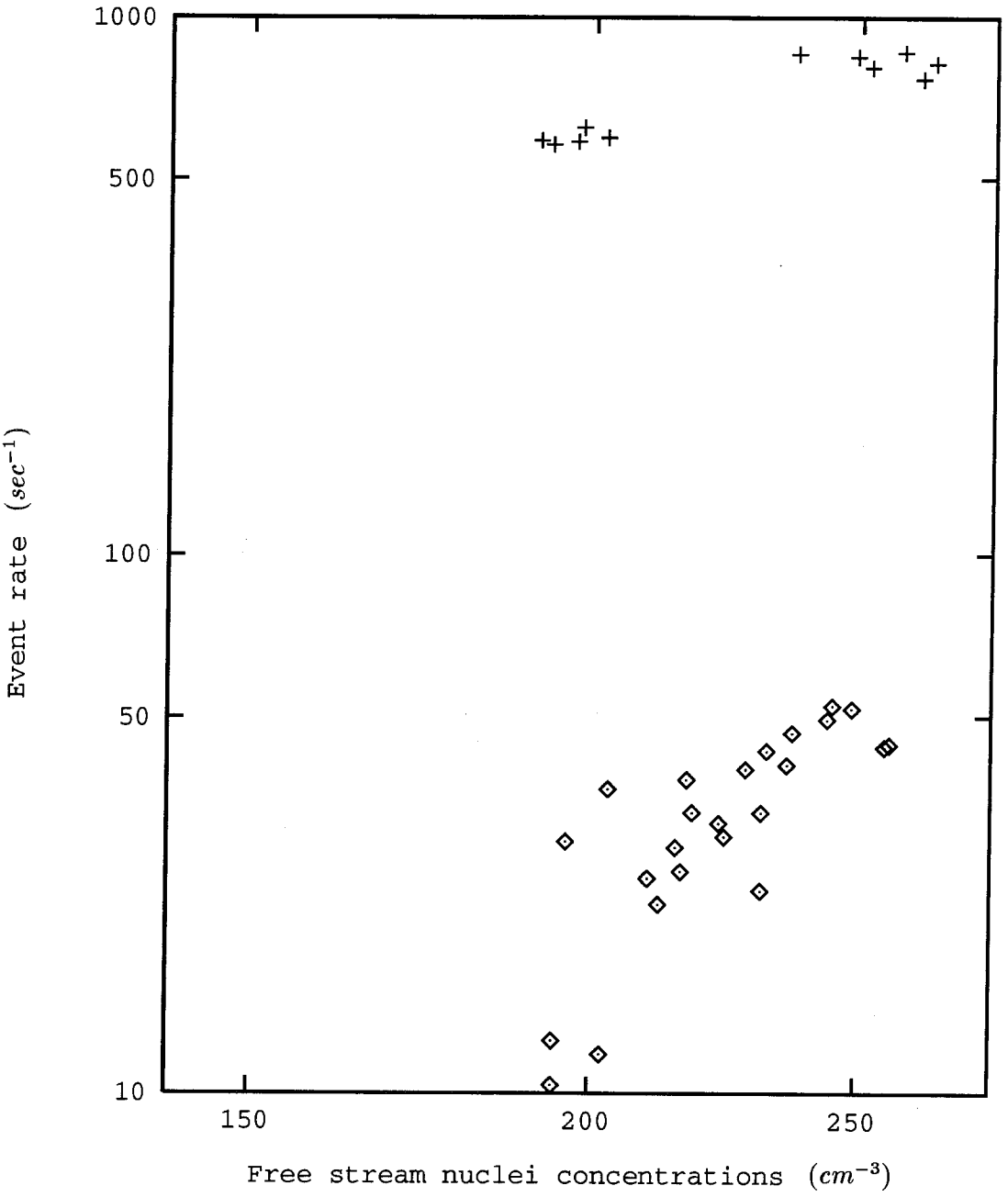

Figure 4.2: Changes in the cavitation event rate on a 5.08cm Schiebe body in the Low Turbulence Water Tunnel as a function of free stream nuclei concentration at $U = 9m/sec$ and two cavitation numbers, $\sigma = 0.57$ ($\diamond$) and $\sigma = 0.45$ (+).

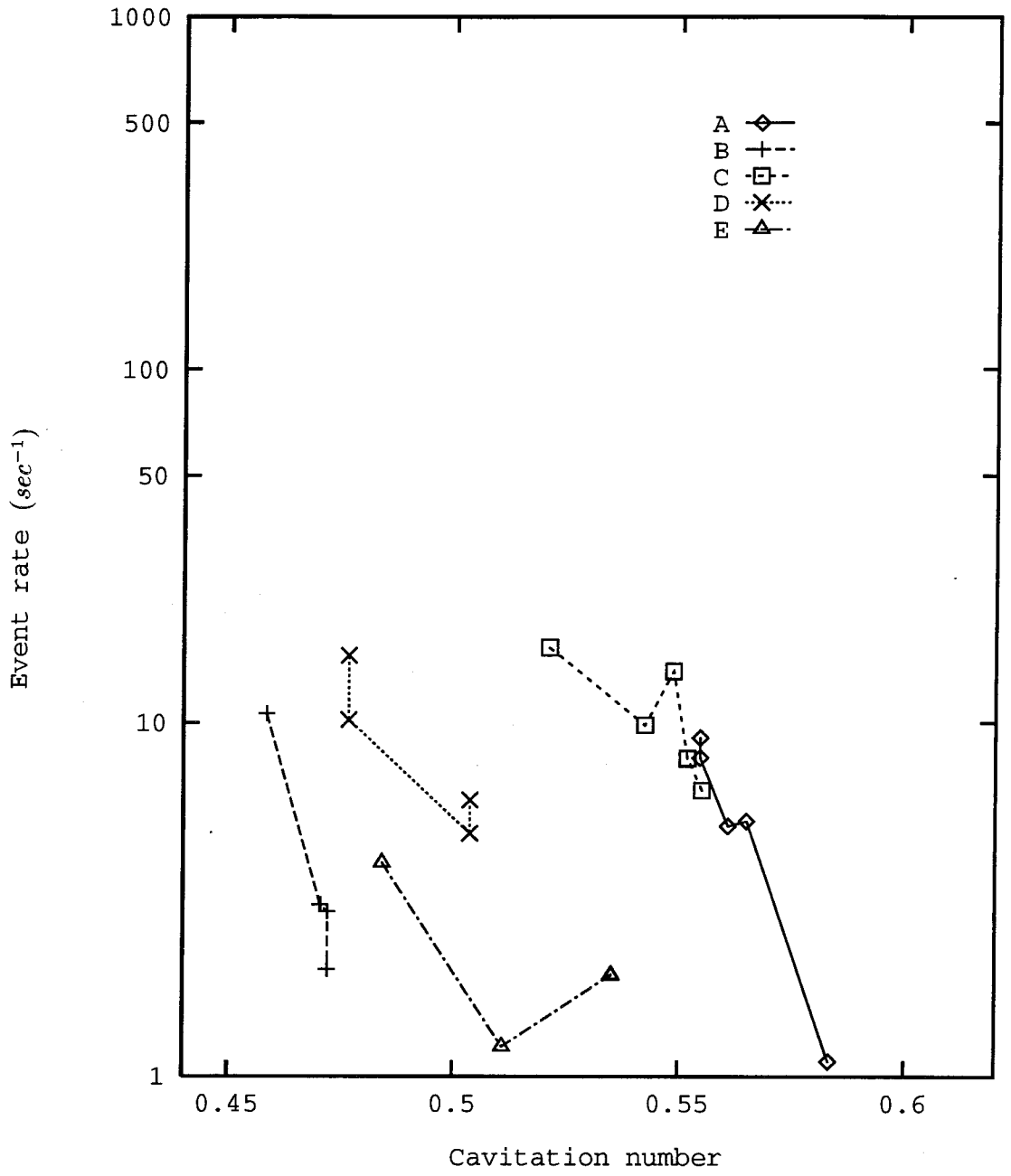

Figure 4.3: Changes of cavitation event rate on a $5.08cm$ Schiebe headform as a function of cavitation number in the High Speed Water Tunnel. The data is plotted for various tunnel speeds and nuclei concentrations as follows: **(A)**: $U = 8.1m/sec$, $3.6cm^{-3} < C < 4.3cm^{-3}$, **(B)**: $U = 9.4m/sec$, $C = 0.8cm^{-3}$, **(C)**: $U = 9.4m/sec$, $1.7cm^{-3} < C < 2.4cm^{-3}$, **(D)**: $U = 12.6m/sec$, $2.0cm^{-3} < C < 3.0cm^{-3}$, **(E)**: $U = 14.5m/sec$, $1.6cm^{-3} < C < 2.9cm^{-3}$.

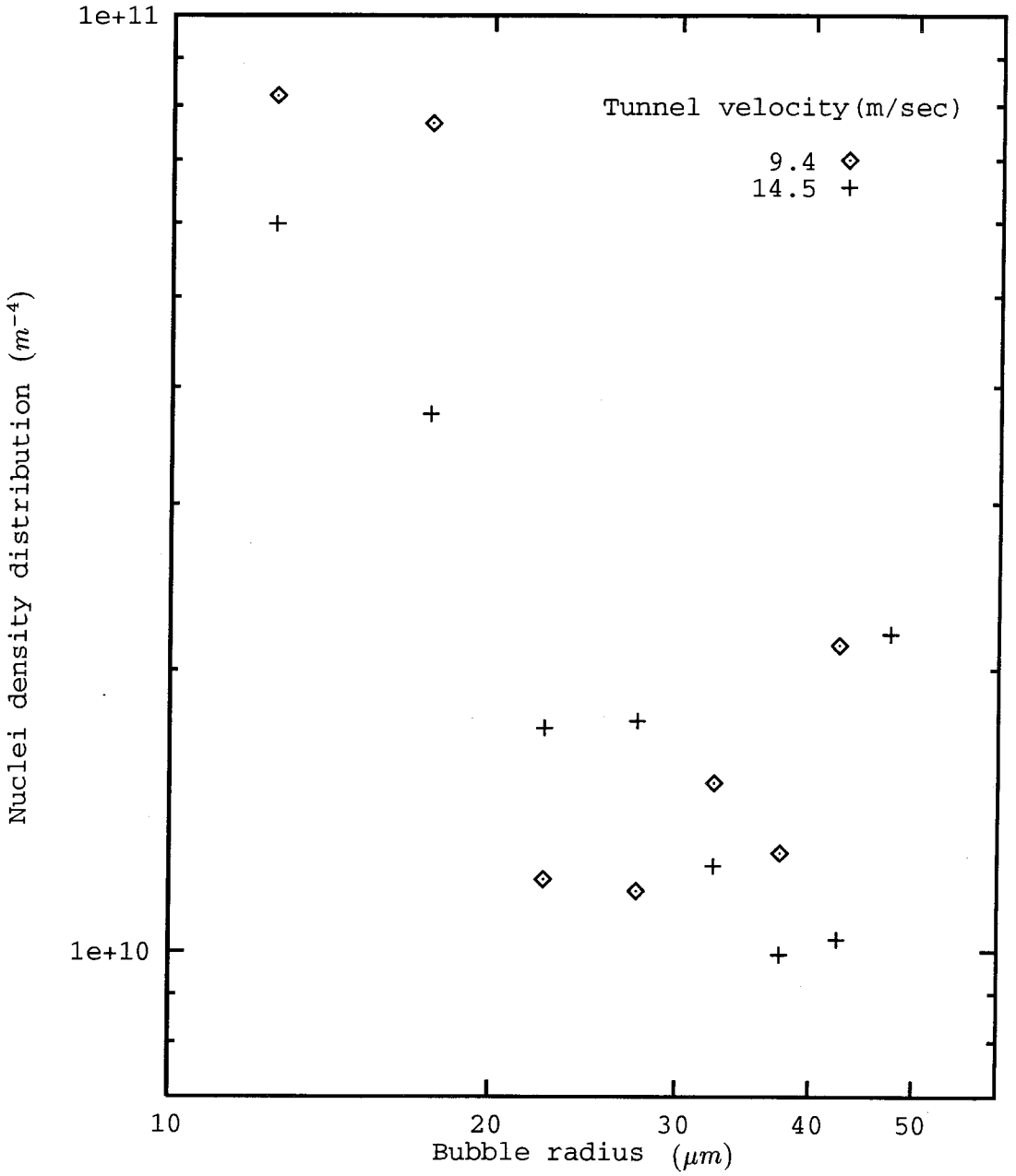

Figure 4.4: A comparison of typical nuclei number density distributions in the High Speed Water Tunnel at a cavitation number of $\sigma = 0.54$ and different tunnel velocities: $9.4 m/sec$ ($\diamond$) and $14.5 m/sec$ (+).

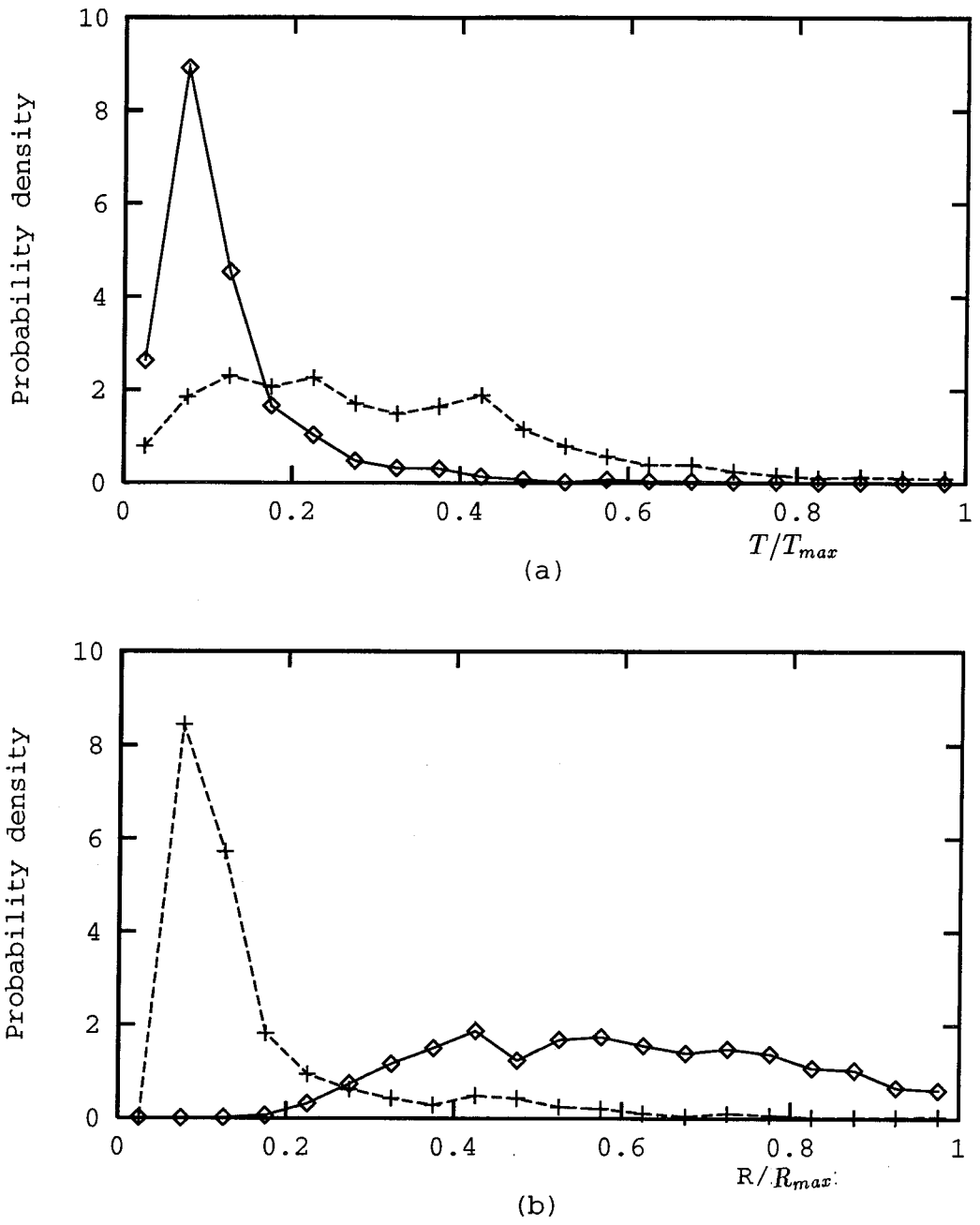

Figure 4.5: Probability density distributions of (a) the time between two events, T, normalized by the maximum time period between two events, T_{max}, and of (b) the bubble radius, R, normalized by the maximum bubble radius, R_{max}, at a velocity of $U = 9m/sec$ and at two different cavitation numbers: $\sigma = 0.45$ ($\diamond$) and $\sigma = 0.56$ (+).

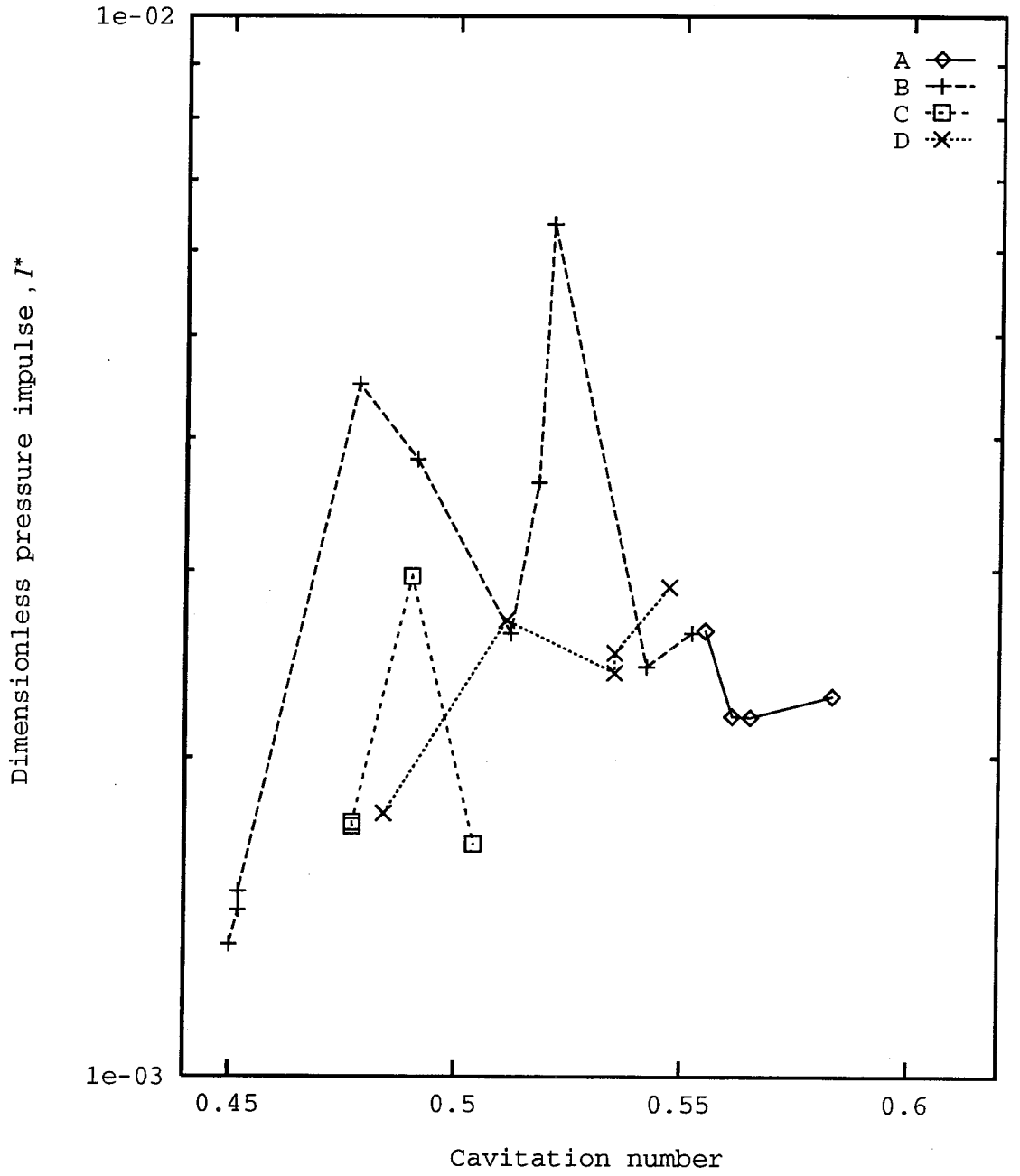

Figure 4.6: Dimensionless pressure impulse as a function of cavitation number measured in the High Speed Water Tunnel at Caltech. The data is plotted for various tunnel speeds and nuclei concentrations as follows: **(A)**: $U = 8.1m/sec$, $2cm^{-3} < C < 3cm^{-3}$, **(B)**: $U = 9.4m/sec$, $C = 0.8cm^{-3}$, **(C)**: $U = 12.6m/sec$, $1.6cm^{-3} < C < 2.9cm^{-3}$, **(D)**: $U = 14.5m/sec$, $1.7cm^{-3} < C < 2.4cm^{-3}$.

Chapter 5

An Analytical Model for Cavitation Event Rate

5.1 Introduction

It has long been recognized that traveling bubble cavitation occurs as a result of micro-sized cavitation "nuclei" being convected into and then out of a low pressure region in a flow. One consequence of this is the recognition that cavitation inception depends on the criterion one establishes in terms of the number of cavitation events occurring per unit time. Because of the difficulties experienced in measuring the nuclei in a water tunnel (see Billet, 1985), there have been relatively few attempts to experimentally verify a relationship between the nuclei population in the oncoming flow and the observed event rates. Two of the earliest attempts were the efforts by Franklin and McMillan (1984) and Ooi (1985) to synthesize the cavitation event rate in a submerged, turbulent jet (see also Pauchet *et al.,* 1992). However, one of the major uncertainties in that flow is the difficulty in characterizing the turbulent

pressure fluctuations experienced by the bubble.

More recently Meyer *et al.* (1989, 1992) have carried out numerical computations of the cavitation event rates on an axisymmetric headform using an assumed nuclei number density distribution in the incident stream. The approximate analytical model presented by Ceccio and Brennen (1992) is similar in concept. The present chapter establishes an approximate analytical model connecting the cavitation event rate with the nuclei distribution. The effects of the boundary layer flow rate, of the bubble screening, of the observable size and of the bubble/bubble interactions are examined and included in the model. Though more approximate than the numerical computations of Meyer *et al.*, the analytical expressions provide insights into the important mechanisms and allow application to more complex flow geometries. It is also possible to include in the calculations more complex effects such as bubble interactions.

5.2 Spherical Bubble Dynamics

The dynamics of bubbles in a liquid responding to an imposed pressure fluctuation have been considered with varying degrees of complexity. The first and the simplest is that of Rayleigh (1917). In Rayleigh's analysis, the medium inside the bubble is liquid vapor and the surrounding liquid is incompressible. Later other effects, such as non-condensable gas, viscosity and surface tension were considered by Plesset (1949), Neppiras and Noltignk (1950, 1951) and Houghton (1963).

The Rayleigh-Plesset equation for spherical bubble dynamics is given by:

$$R\frac{d^2R}{d^2t} + \frac{3}{2}\left(\frac{dR}{dt}\right)^2 = \frac{p_v - p_{b\infty}}{\rho_L} + \frac{p_{G_0}}{\rho_L}\left(\frac{R_0}{R}\right)^{3k} - \frac{4\nu_L}{R}\frac{dR}{dt} - \frac{2S}{\rho_L R} \qquad (5.1)$$

Where R is the bubble radius, R_0 is the initial bubble radius, S is the surface tension, ν_L is the kinetic viscosity, p_{G_0} is the initial pressure of the non-condensable gas, k is the polytropic constant for the gas and p_v and $p_{b\infty}$ are the vapor pressure and pressure at infinity respectively. The pressure at infinity, $p_{b\infty}$, is usually a function of time.

When a nucleus is in equilibrium, the pressure of the non-condensable gas and the vapor pressure in the nucleus balance the external pressure and the surface tension:

$$p_{G_0} = (p_{b\infty} - p_v) + \frac{2S}{R_0} \tag{5.2}$$

By choosing a characteristic length for the flow (r_H), a characteristic time (r_H/U) and a reference pressure p_∞, Equation (5.1) can be non-dimensionalized as follows:

$$R^*\ddot{R}^* + \frac{3}{2}(\dot{R}^*)^2 = \frac{1}{2}(-C_P - \sigma) + \frac{p_{G0}}{\rho_L U^2}\left(\frac{R_0^*}{R^*}\right)^{3k} - \frac{8}{Re}\frac{\dot{R}^*}{R^*} - \frac{4}{We}\frac{1}{R^*} \tag{5.3}$$

Where C_P, σ, We and Re are the pressure coefficient, the cavitation number, the Weber number and the Reynolds number respectively. These numbers and the variables in the above equation are defined as

$$\begin{aligned}
C_P &= \frac{(p_{b\infty} - p_\infty)}{\frac{1}{2}\rho_L U^2} \\
\sigma &= \frac{p_\infty - p_v}{\frac{1}{2}\rho_L U^2} \\
We &= \frac{\rho_L U^2 (2r_H)}{S} \\
Re &= \frac{U(2r_H)}{\nu_L} \\
R^* &= \frac{R}{r_H} \\
t^* &= tU/r_H \\
\dot{R}^* &= \frac{dR^*}{dt^*} \\
\ddot{R}^* &= \frac{d^2R^*}{dt^{*2}}
\end{aligned} \tag{5.4}$$

For the typical experimental conditions of the last chapter, $We \sim 10^5$, $Re \sim 10^6$ and $R_0^* \sim 10^{-3}$. Substituting these values into equation (5.3), we find that the last three terms are much smaller than the first two terms on the left side of equation (5.3) if R^* is much larger than R_0^*. This provides the foundation for an asymptotic solution of equation (5.3) for bubble growth.

With a constant value of $p_{b\infty}$ for $t > 0$, equation (5.1) can be integrated once, provided that the viscosity term is neglected. The integration for $k \neq 1$ yields

$$\begin{aligned} \dot{R}^2 &= \frac{2(p_v - p_{b\infty})}{3\rho_L}\left[1 - (\frac{R_0}{R})^3\right] + \frac{2p_{G_0}}{3(1-k)\rho_L}\left[(\frac{R_0}{R})^{3k} - (\frac{R_0}{R})^3\right] \\ &\quad -\frac{2S}{\rho_L R_0}\left[(\frac{R_0}{R}) - (\frac{R_0}{R})^3\right] \end{aligned} \tag{5.5}$$

where the initial condition (5.2) has been used.

Equation (5.5) shows that the asymptotic growth rate for $R \gg R_0$ is given by

$$\dot{R} \rightarrow \left[\frac{2(p_v - p_{b\infty})}{3\rho_L}\right]^{\frac{1}{2}} \tag{5.6}$$

$$= \left[\frac{1}{3}(-C_P - \sigma)\right]^{\frac{1}{2}} U \tag{5.7}$$

If the duration of the bubble growth is Δt, the asymptotic maximum bubble size is then given by

$$R_{max} = \left[\frac{2(p_v - p_{b\infty})}{3\rho_L}\right]^{\frac{1}{2}} \Delta t \tag{5.8}$$

$$= \left[\frac{1}{3}(-C_P - \sigma)\right]^{\frac{1}{2}} (U\Delta t) \tag{5.9}$$

Figure 5.2 shows a comparison of the asymptotic maximum bubble radius obtained by (5.8) with the maximum bubble radius obtained by numerically solving the Rayleigh-Plesset equation (5.3) for a chosen pressure field:

$$C_P(t) = -0.19e^{(\pi - 2t)}\sin(t)$$

As shown in the figure, the asymptotic approach is a very good estimation of the bubble maximum size.

Equation (5.5) can not be integrated further to yield the bubble radius and time relationship. But it can be written as

$$t = R_0 \int_1^{R/R_0} \left[\frac{2(p_v - p_{b\infty})}{3\rho_L}(1 - x^{-3}) + (\frac{2p_{G_0}}{3(1-k)\rho_L})(x^{-3k} - x^{-3}) - \frac{2S}{\rho_L R_0}(x^{-1} - x^{-3}) \right]^{-1/2} dx \tag{5.10}$$

where x is a dummy variable for R/R_0.

5.3 Cavitation Event Rate

In this section we will use a characteristic free stream nuclei density distribution function, $N(R)$, to synthesize the cavitation event rate on a cavitating, axisymmetric Schiebe headform, as shown in Figure 2.6.

The measurements of the free stream nuclei distribution in the Low Turbulence Water Tunnel and High Speed Water Tunnel at Caltech often have the following characteristic form:

$$N(R) = C \frac{\log_{10} e}{(2\pi)^{1/2} \lambda R} exp(-\frac{(\log R - \log \xi)^2}{2\lambda^2}) \tag{5.11}$$

where C is the nuclei concentration. By adjusting the values of ξ and λ, the distribution function (5.11) can be made to fit most of the observed nuclei distribution functions. It is preferable to the more frequently used power law ($N(R) \sim R^{-n}$, where n is between about 3 and 5) because it allows simulation of the peak in the population which is often observed (at $R = \xi$) and of the fact that the population of large bubbles is very small. Also in this expression, the nuclei concentration appears explicitly expressed and allows direct

evaluation of its effect upon the results.

The problem is to evaluate how many of the nuclei are convected into the region of low pressure near the minimum pressure point on the surface of the body and therefore grow to observable macroscopic vapor bubbles (see Figure 5.1). Some simplifying assumptions allow us to avoid lengthy numerical computations of the bubble dynamics (using the Rayleigh-Plesset equation) for every nucleus size, every streamline, every cavitation number, etc. Meyer *et al.* (1992) conducted a detailed numerical study of this kind which included most of the effects studied here. In this chapter we present a much simpler analytical approach which, though more approximate, is probably as accurate as the current experimental data would merit.

Blake (1949) and Johnson and Hsieh (1966) studied the stability of a cavitation bubble. They found that there is a lower radius limit, below which a bubble will not cavitate, that is to say, will not grow explosively. Ceccio and Brennen (1992) carried out numerical integration of the Rayleigh-Plesset equation and found that for a given cavitation number, σ, and minimum pressure coefficient, C_{PM}, all nuclei above a certain critical size, $R = R_C$, would grow explosively to roughly the same observable bubble size and therefore would be registered as "cavitation events." Furthermore, the critical size, R_C, appeared to be almost independent of the details of the pressure/time history and a function only of the difference between the minimum pressure and the vapor pressure (represented non-dimensionally by $(-C_{PM} - \sigma)$), the upstream velocity, U, the fluid density, ρ_L, and surface tension, S. Specifically,

$$R_C = \frac{8\beta S}{3\rho_L U^2(-C_{PM} - \sigma)} \tag{5.12}$$

fitted the bubble dynamic calculations very well when the empirical parameter $\beta \approx 1$. This

expression corresponds to the appropriate Blake critical nuclei size (Blake, 1949, Daily and Johnson, 1956) and is consistent with the stability analysis put forward by Flynn (1964), Johnson and Hsieh (1966) and the numerical calculations by Meyer *et al.* (1992). Its use saves a great deal of computational effort. Furthermore, it means that we need not concern ourselves with the detailed pressure/time history along the entire length of each streamline but can simply focus on the region around the minimum pressure point.

It is also necessary to determine how the minimum pressure coefficient, C_{PM}, varies from streamline to streamline. Here again we will use a simple analytic expression derived from much more complex computations. A panel method was developed to solve the potential flow around any axisymmetric headform (see Kuhn de Chizelle, 1993). This was used to calculate the potential flow around the Schiebe headform. Such calculations suggested that the pressure gradient, dp/dy, normal to the surface in the vicinity of the minimum pressure point could be approximated by $\rho_L U_M^2/r_K$ where $U_M = U(1 - C_{PMS})^{\frac{1}{2}}$ and C_{PMS} are respectively the velocity and pressure coefficient at the minimum pressure point on the surface of the body and r_K is a measure of the radius of curvature of the streamlines in this region. For the Schiebe body (C_{PMS} =-0.75) it is found that r_H/r_K =2 provides an approximate representation of the variation in the minimum pressure coefficient, C_{PM}, on a streamline with the distance y of that streamline from the surface. The actual variation of C_{PM} with y from the potential flow calculation is shown in Figure 5.3, along with several approximations. With $dp/dy = \rho_L U_M^2/r_K$ it follows that

$$C_{PM} = C_{PMS} + 2y(1 - C_{PMS})/r_K \tag{5.13}$$

This expression allows us to evaluate, from equation (5.12), the critical nuclei size, $R_C(y)$, for each streamline; R_C therefore increases with the distance, y, of the streamline from

the surface. A larger critical size means that fewer of the available nuclei will generate cavitation events. The process is terminated on that streamline which just touches the isobar $C_{PM} = -\sigma$, for then the minimum pressure is equal to the vapor pressure and no cavitation events will occur on this streamline or any outside it. Consequently, we need only be concerned with a region near the surface given by

$$0 < y \leq y_M f_3 \tag{5.14}$$

where

$$y_M = \frac{(-C_{PMS} - \sigma)}{2(1 - C_{PMS})} r_K \tag{5.15}$$

and f_3 =1. Different values of f_3 will be used later to examine the influence of a minimum observable bubble size, R_M.

Using the relations (5.12) and (5.13) and disregarding any possible effects of the boundary layer or of relative motion between the nucleus and the flow, one can then construct an event rate from the nuclei number distribution as follows. The volume flow rate passing through two stream surfaces a distance, dy, apart at the minimum pressure point (see Figure 5.1) is given by

$$2\pi r_S U(1 - C_{PMS})^{\frac{1}{2}} f_1(y) dy \tag{5.16}$$

where $f_1(y)$ =1, but different values will be used later to account for boundary layer effects. The quantity r_S is the radial distance from the axis of symmetry to the minimum pressure point (for the Schiebe body, $r_S/r_H \approx 0.75$). It follows from equation (5.16) that the cavitation event rate, dE, in the stream tube, dy, is given by

$$dE = 2\pi r_S U(1 - C_{PMS})^{\frac{1}{2}} f_1(y) dy \int_{R_C(y)}^{\infty} \frac{N(R)dR}{f_2(R, y)(1 + n_i)} \tag{5.17}$$

where $f_2(R,y)$ =1, but different values will be used later to account for screening effects due to relative motion between the nuclei and the liquid, and $n_i = 0$, but different values will be used later to account for the bubble/bubble interactions. In the above equation it follows from equations (5.12) and (5.13) that

$$R_C(y) = \frac{8\beta S}{3\rho_L U^2}\left[-\sigma - C_{PMS} - \frac{2y(1-C_{PMS})}{r_K}\right]^{-1} \tag{5.18}$$

Note that $R_C(y \to y_M) \to \infty$. It follows that the total cavitation event rate, E, will be

$$E = \int_0^{y_M f_3} 2\pi r_S U(1-C_{PMS})^{\frac{1}{2}} f_1(y) \int_{R_C(y)}^{\infty} \frac{N(R)dR}{f_2(R,y)(1+n_i)} dy \tag{5.19}$$

where $f_3 = 1$, but different values will be used later to account for the observable bubble size effect.

5.3.1 Boundary Layer Effect

The above analysis neglected the effects which the presence of a boundary layer might have on the pressure/time history experienced by a potential cavitation nucleus. Several such effects can be envisaged. These include the fact that the boundary layer will reduce the volume flow rate of fluid traveling close to the headform and thus reduce the supply of nuclei. It may also alter the shape of the isobars near the surface. Here we will explore only the first of these two effects. To do so we assume a simple form for the boundary layer profile near the minimum pressure point namely

$$\frac{u}{u_M} = \begin{cases} 2\left(\frac{y}{\delta}\right) - 2\left(\frac{y}{\delta}\right)^3 + \left(\frac{y}{\delta}\right)^4 & \text{for } y < \delta \\ 1 & \text{for } y \geq \delta \end{cases} \tag{5.20}$$

where δ is the boundary layer thickness. If δ_2 is the momentum thickness, it follows that $\delta_2 = 0.133\delta$ and, using the modified Thwaites method to solve for the laminar boundary

layer thickness (Thwaites, 1949, Rott and Crabtree, 1952) for the Schiebe body, we find that

$$\frac{\delta_2}{r_H} \approx 0.68(\frac{\nu_L}{r_H U})^{\frac{1}{2}} \tag{5.21}$$

Then, to account for the decrease in volume flow rate due to the boundary layer, the expressions (5.16), (5.17) and (5.19) should include values of $f_1(y)$ different from unity:

$$f_1(y) = \begin{cases} 2\left(\frac{y}{\delta}\right) - 2\left(\frac{y}{\delta}\right)^3 + \left(\frac{y}{\delta}\right)^4 & \text{for } y < \delta \\ 1 & \text{for } y > \delta \end{cases} \tag{5.22}$$

with $\delta = 5.10(\nu_L r_H / U)^{\frac{1}{2}}$.

It is also true that the boundary layer will affect the shape of the isobars and therefore cause some alteration of the expressions (5.13), (5.15), and (5.18); we have not included this effect in the present analysis.

5.3.2 Bubble Screening Effect

In their study of the potential cavitation of nuclei, Johnson and Hsieh (1966) recognized that the relative motion between the nuclei and the liquid might play an important role in determining the number of nuclei which enter the region in which the pressure is below the vapor pressure. Specifically, they recognized that a bubble "screening" effect would occur in which the nuclei are forced away from the body due to the large pressure gradients normal to the streamlines in the vicinity of the stagnation point. This outward displacement would be larger for the larger bubbles. Because one is concerned only with streamlines very close to the stagnation streamline and the body surface and because the streamline curvature and therefore the pressure gradient normal to the streamline is much larger in the vicinity of the stagnation point than anywhere else, we may evaluate this screening effect by focusing

attention on the stagnation point flow alone. In order to obtain an estimate of this effect we shall assume that the nuclei under consideration (of radius R) are all sufficiently small that the Reynolds number of the relative motion is much smaller than unity. Then the velocity of the nucleus in a direction normal to the streamline, v_n, is given by

$$v_n = \frac{2}{9}\frac{R^2}{\mu}\left(\frac{\partial p}{\partial n}\right) \tag{5.23}$$

where $\partial p/\partial n$ is the local pressure gradient normal to the streamline. Then the total displacement, ϵ, across the streamlines is given by

$$\epsilon = \int_A^B v_n \, dt = \int_A^B \frac{v_n}{q} ds \tag{5.24}$$

where q is the magnitude of the fluid velocity, the coordinate s is measured along a streamline, A is a point far upstream and B is a location after the large pressure gradients in the vicinity of the stagnation point have been experienced. Note that ϵ will, of course, differ from streamline to streamline and will therefore be a function of r defined as the radial position of the streamline far upstream of the body (see Figure 5.1). Thus

$$\begin{aligned} \frac{\epsilon(r/r_H)}{r_H} &= \frac{2R^2U}{9\nu_L r_H}\int_A^B \frac{1}{\rho_L U^2}\frac{\partial p}{\partial(n/r_H)}\frac{U}{|q|}\, d\left(\frac{s}{r_H}\right) \\ &= \frac{2R^2U}{9\nu_L r_H}\,\Sigma(r/r_H) \end{aligned} \tag{5.25}$$

where $\Sigma(r/r_H)$ is used to denote the dimensionless integral on the previous line.

Since the stagnation point flow is the same on any blunt axisymmetric body, it is appropriate to choose to examine the stagnation region in the potential flow around a sphere in order to evaluate $\Sigma(r/r_H)$. This is a non-trivial calculation, and the details will be omitted here for the sake of brevity (See Appendix B for details). The result is the function $\Sigma(r/r_H)$

presented in Figure 5.4; for convenience this can be approximated by the empirical relation

$$\Sigma(r/r_H) = \Gamma(r/r_H)^\gamma \tag{5.26}$$

where $\Gamma \approx 1.69$, $\gamma \approx 0.5$.

Having evaluated the screening displacement, it can be applied to the evaluation of the event rate in the following way. A nucleus of radius R which is on the streamline at radius r far upstream will, when it reaches the low pressure region, be on the streamline which is the following distance, y, from the body surface:

$$\frac{y}{r_H} = \frac{1}{2(1-C_{PMS})^{\frac{1}{2}}} \frac{r^2}{r_S r_H} + \frac{2}{9}(\frac{R}{r_H})^2 \frac{r_H U}{\nu_L} \Sigma(r/r_H) \tag{5.27}$$

Thus the stream tube between y and $y + dy$ will contain all the nuclei of radius R which were present in the upstream flow between radii r and $r + dr$ (Figure 5.1) where

$$\frac{dy}{r_H} = \frac{r\ dr}{(1-C_{PMS})^{\frac{1}{2}} r_S r_H} f_2(R,y) \tag{5.28}$$

and

$$f_2(R,y) = 1 + \frac{2}{9}(\frac{R}{r_H})^2 (\frac{r_H U}{\nu_L})(1-C_{PMS})^{\frac{1}{2}} (\frac{r_S}{r_H}) \frac{r_H}{r} \Sigma' \tag{5.29}$$

where Σ' denotes $d\Sigma/d(r/r_H)$ and r and y are related by equation (5.27). Since the liquid flow between y and $y + dy$ is still given by the expression (5.16), it follows that the actual number distribution function for the stream tube between y and $y + dy$ is $N_E(R,y)$ where

$$N_E(R,y) = N(R)/f_2(R,y) \tag{5.30}$$

Consequently, the screening effect alters the event rate by introducing an expression for $f_2(R,y)$ which is not equal to one in the expression (5.19), namely that given by equation (5.29).

5.3.3 Observable Bubble Size Effect

Normally, experimental observations can only detect cavitating bubbles when they achieve a certain observable size, say R_M, and in this section we shall incorporate this "observable cavitation bubble size effect" in our analysis. This requires an analysis of the maximum size, R_{max}, achieved by the cavitation bubble.

From spherical bubble dynamics, the asymptotic maximum bubble size is the product of the bubble growth rate and the growth time. The bubble growth rate of a bubble entering the low pressure region at an off-body distance of y is given approximately by

$$\frac{dR}{dt} = \frac{U}{\sqrt{3}}(-\sigma - C_{PM}(y))^{1/2} \tag{5.31}$$

where $C_{PM}(y)$ is given by equation (5.13) and the growth time is given by

$$t_G = \frac{\Delta s}{u_M} = \frac{\Delta s}{r_H} \frac{r_H}{U(1 - C_{PMS})^{1/2}} \tag{5.32}$$

where Δs is the distance a bubble traveled in the low pressure region.

The pressure coefficient near the minimum pressure point can be approximated by

$$\begin{aligned} C_P(y,s) &= C_{PMS} + \frac{2y(1 - C_{PMS})}{r_K} + \frac{C^*_{P1}(s - s_m)^2}{r_H^2} \\ &= C_{PM}(y) + \frac{C^*_{P1}(s - s_m)^2}{r_H^2} \end{aligned} \tag{5.33}$$

where s is a coordinate measured along a streamline, s_m is the minimum pressure location and C_{PM} is the minimum pressure coefficient along a streamline and is given by equation (5.13). Examining the pressure distribution for the Schiebe body, one finds the value of the constant C^*_{P1} to be about 6.2. The boundary of the low pressure region ($C_P = -\sigma$) is therefore a parabola:

$$\frac{y}{r_H} = \frac{C^*_{P1}}{2(1 - C_{PMS})} \frac{r_K}{r_H} \left(\frac{s}{r_H} - \frac{s_m}{r_H}\right)^2 + \frac{(-C_{PMS} - \sigma)}{2(1 - C_{PMS})} \frac{r_K}{r_H} \tag{5.34}$$

By solving equation (5.34), we have

$$\frac{\Delta s}{r_H} = \frac{2(C_{PM}(y) - \sigma)^{1/2}}{C_{P1}^{*1/2}} \tag{5.35}$$

It follows that the maximum size, R_{max}, a cavitating bubble can reach will be given roughly by

$$\frac{R_{max}}{r_H} = \left(\frac{2}{\sqrt{3}C_{P1}^{*1/2}}\right) \frac{(-C_{PM}(y) - \sigma)}{(1 - C_{PMS})^{1/2}} \tag{5.36}$$

Only those bubbles whose maximum size, R_{max}, is greater than a certain radius, R_M, will be considered to be observable cavitation events. By solving $R_{max} \geq R_M$ for y, we have

$$y \leq y_M f_3(R_M/r_H) \tag{5.37}$$

where

$$f_3(\frac{R_M}{r_H}) = 1 - \frac{\sqrt{3}C_{P1}^{*1/2}}{2} \frac{(1 - C_{PMS})^{1/2}}{(-C_{PMS} - \sigma)} (\frac{R_M}{r_H}) \tag{5.38}$$

where y_M is given by (5.15). Notice that as $R_M \rightarrow 0$, $f_3(R_M/r_H) \rightarrow 1$. And when

$$\sigma_{crt} = -C_{PMS} - \frac{\sqrt{3}C_{P1}^{*1/2}(1 - C_{PMS})^{1/2}}{2} (\frac{R_M}{r_H}) \tag{5.39}$$

$f_3(R_M/r_H) = 0$. This means that, if $\sigma \geq \sigma_{crt}$, there will be no bubbles of a size greater than R_M. Hence, σ_{crt} is the threshold cavitation number. For example, for C_{PMS} =-0.75 and R_M/r_H =0.02, σ_{crt} is 0.57, which is far less than $-C_{PMS}$ =0.78.

Now consider the probability density distribution of the bubble maximum size which is resulted from the above deductions. From equation (5.17), the number of bubbles at an off-body distance of y in the stream tube of dy is given by

$$dE = 2\pi r_S U(1 - C_{PMS})^{1/2} f_1 \int_{R_C}^{\infty} \frac{N(R)}{f_2} dR dy \tag{5.40}$$

and from equation (5.36) and (5.13)

$$\frac{dR_{max}}{r_H} = -\frac{4}{\sqrt{3}C_{P1}^{*1/2}}\frac{(1-C_{PMS})^{1/2}dy}{r_K} \tag{5.41}$$

Combining equations (5.40), (5.41) and (5.19) yields the probability distribution of the maximum bubble size, $P_{max}(R_{max})$, given implicitly by

$$P_{max}(R_{max}) = \left(\frac{\sqrt{3}C_{P1}^{*1/2}}{4(1-C_{PMS})^{1/2}}(\frac{r_K}{r_H})\right)\frac{f_1(y)\int_{R_C(y)}^{\infty}\frac{N(R)}{f_2(R,y)}dR}{\int_0^{y_M} f_1(y)\int_{R_C(y)}^{\infty}\frac{N(R)}{f_2(R,y)}dRdy} \tag{5.42}$$

and

$$\frac{R_{max}}{r_H} = \left(\frac{2}{\sqrt{3}C_{P1}^{*1/2}}\right)\frac{(-C_{PM}(y)-\sigma)}{(1-C_{PMS})^{1/2}} \tag{5.43}$$

where y varies from 0 to y_M.

5.3.4 Effect of Bubble/Bubble Interactions

As a bubble grows in the low pressure region, the pressure field close to the bubble is changed by the rate of growth of the bubble. Within a certain distance close to the growing bubble, the pressure perturbation due to bubble growth increases the local pressure above the critical pressure for a nuclei to cavitate. Nuclei within this volume will not cavitate. Though other features may contribute to the bubble interaction effect, this is probably the dominant contribution and the most readily estimated.

To quantify this effect, we need to calculate the liquid volume in which the local pressure is increased above the Blake critical pressure by the bubble growth. First, consider the dynamics of a small nucleus with initial radius R_0, subjected to low pressure, $p_{b\infty}$. The pressure perturbation due to the bubble growth is given by

$$\frac{p(r)-p_{b\infty}}{\rho_L} \approx \frac{R}{r}(R\ddot{R}+2(\dot{R})^2) \tag{5.44}$$

where r is the distance from the center of the growing bubble. When $R \gg R_0$, substituting equations (5.1) and (5.6), we have

$$p(r) - p_{b\infty} = \frac{4}{3}\frac{R}{r}(p_v - p_{b\infty}) \tag{5.45}$$

For a nucleus to cavitate, the pressure around it must be less than Blake critical pressure, given by

$$p_c = p_v - \frac{4S}{3}\left[\frac{2S}{3p_{G0}R_0^3}\right]^{\frac{1}{2}} \tag{5.46}$$

Substituting the initial condition (5.2) into the above equation, we can estimate the critical pressure coefficient, $C_{P_{crt}}$, for a bubble with initial radius R_0 to cavitate:

$$C_{P_{crt}} = -\sigma - \sigma' \tag{5.47}$$

where σ' is given by

$$\sigma' = \frac{1}{3}\left(\frac{8S}{\rho_L U^2 R_0}\right)\left[\frac{1}{6}\left(\frac{8S}{\rho_L U^2 R_0}\right)\frac{1}{\sigma + \left(\frac{8S}{\rho_L U^2 R_0}\right)}\right]^{\frac{1}{2}} \tag{5.48}$$

For a nucleus to cavitate, the local pressure must be smaller than the Blake critical pressure. Solving $p(r) > p_c$ by combining equation (5.47) and equation (5.45), we have the range, r, from the center of the growing bubble, within which other nuclei will not cavitate.

$$r < \frac{4}{3}\frac{(-C_P - \sigma)}{(-C_P - \sigma - \sigma')}R \tag{5.49}$$

Now consider the situation on a Schiebe headform. The minimum pressure a nucleus experiences is the minimum pressure on the bubble trajectory, $C_{PM}(y)$. The bubble size at the point where the pressure reaches the minimum pressure is approximately half of the maximum bubble size, $R_{max}/2$. Thus on a Schiebe body, the nuclei within a certain distance from the center of a growing bubble will not cavitate due to the bubble/bubble interaction

effect. We denote this distance as the effective radius, r_e, and it is given by:

$$r_e \approx \frac{4}{3}\frac{(-C_{PM}(y)-\sigma)}{(-C_{PM}(y)-\sigma-\sigma')}\left(\frac{R_{max}}{2}\right) \tag{5.50}$$

Note in equation (5.48) σ' depends on R_0 and $C_{PM}(y)$ is a function of y. Therefore, r_e is a function of y and R_0.

The number of nuclei which will not cavitate due to the pressure perturbation surrounding a growing bubble is

$$n_i = \int_0^\infty \frac{4}{3}\pi\left[r_e^3 - \left(\frac{R_{max}}{2}\right)^3\right] N(R_0)dR_0 \tag{5.51}$$

Therefore, among $1+n_i$ nuclei, only one nucleus will cavitate. Consequently, the effective nuclei number density distribution is given by

$$\frac{N(R)}{1+n_i} \tag{5.52}$$

where

$$n_i = \frac{1}{6}\pi R_{max}^3 \int_0^\infty \left[\frac{64}{27}\left(\frac{-C_{PM}(y)-\sigma}{-C_{PM}(y)-\sigma-\sigma'}\right)^3 - 1\right] N(R_0)dR_0 \tag{5.53}$$

Where σ' is defined by (5.48), R_{max} is defined by (5.36), $C_{PM}(y)$ is defined by (5.13) and $N(R_0)$ is the nuclei number density distribution.

The effect of bubble interactions, n_i, is proportional to the cube of the maximum bubble size. From equation (5.36), R_{max} is proportional to the headform size. This means that for a small headform bubble, interactions may not be very important for the cavitation event rate. But, for a large headform, bubble interactions may be very important. Also note that when $n_i \gg 1$, $1+n_i \approx n_i$. Then the effective nuclei number density distribution can be written approximately as

$$\frac{N(R)}{\frac{1}{6}\pi R_{max}^3 \int_0^\infty \left[\frac{64}{27}\left(\frac{-C_{PM}(y)-\sigma}{-C_{PM}(y)-\sigma-\sigma'}\right)^3 - 1\right] N(R_0)dR_0}$$

Note that $N(R)$ appears in both the numerator and the denominator. Though they can not cancel each other, the nuclei concentration in the distribution will cancel. This means that when bubble interactions becomes very large ($n_i \gg 1$), due to large nuclei concentration or maximum bubble size, the event rate becomes almost independent of the nuclei concentration.

5.4 Results of the Analytical Model

In this section we shall evaluate the various effects on the cavitation event rate and compare the results of the analytical model with the experimental observations.

To evaluate the various effects, we select a particular nuclei number distribution of the form given by equation (5.11), namely

$$\begin{aligned} C &= 100 cm^{-3} \\ \xi &= 9.8\ \mu m \\ \lambda &= 0.49 \end{aligned} \tag{5.54}$$

These values produce a shape which is similar to that of many of the nuclei number distributions measured in the Low Turbulence Water Tunnel and the High Speed Water Tunnel. As we concluded in Chapter 3, the nuclei concentrations could vary substantially in different water tunnels. Thus the value of 100 cm^{-3} is about 100 times bigger than that measured in the High Speed Water Tunnel. This particular nuclei concentration is also consistent with the measurement done by other researchers. It is larger than that proposed by Billet (1985), but is less than the observations in the Low Turbulence Water Tunnel. When viewing the analytical results, one should remember that the cavitation event rates simply scale with

the concentration, C, and therefore the results for other values of the nuclei concentration are easily obtained.

Ceccio and Brennen (1992) performed experimental observations of traveling cavitation bubble on a Schiebe headform of $5.08cm$ in diameter. They found that the electrode instrumentation used to detect the cavitation events could only detect bubbles with a radius approximately greater than $1mm$. This value is used as the minimum detectable bubble size, R_M, in all calculations.

First, we present in Figure 5.5 typical results for a $5.08cm$ Schiebe headform at a velocity of $9m/sec$ showing the characteristic effects of the boundary layer volume flow (f_1), of the bubble screening (f_2), of the observable cavitation bubble size (f_3) and of the interactions between bubbles (n_i). Note that all these effects can cause a significant reduction in the event rate and, together, can account for an order of magnitude reduction in the event rate. Among all the effects, the bubble screening effect causes the largest reduction in the event rate. At large cavitation numbers, the effect of bubble interactions causes little or no reduction in cavitation event rate. However, at low cavitation numbers, it causes significant reduction. As for the boundary layer flow rate effect, its effect is more obvious at larger cavitation numbers since the boundary layer thickness is comparable with the maximum off-body distance, y_M, at large cavitation numbers. Also note that the observable cavitation bubble size restriction sets up a sharp threshold at a cavitation number of about 0.6.

The effects of the boundary layer flow rate and the bubble screening varied slightly with flow velocity and headform scale. The effect of the bubble/bubble interactions, however, varied significantly with headform size since the bubble size increases with headform size. As the headform size increases, the reduction of cavitation event rate at low cavitation

numbers due to bubble interactions increases with the cube of the headform radius. For the values chosen, at a cavitation number of $\sigma = 0.46$, the bubble interaction factor, n_i, is about 0.9 for a headform radius of $2.5cm$. However, at the same cavitation number, if the headform radius is $25cm$, the bubble interaction factor, n_i, is 900, which produces a significant reduction in the cavitation event rate. However, the cavitation on the headform will usually become fully attached long before the bubble interactions get so intensive.

The event rates predicted by equation (5.19) for two different body sizes and three different flow velocities are shown in Figure 5.6. The effects of the boundary layer flow rate, the bubble screening, the observable bubble size and the bubble/bubble interactions are included in the calculations. It can be seen that the cavitation event rate rises dramatically as the cavitation number is decreased. It follows that the cavitation inception number will change with the headform size. But the maximum cavitation event rates are of the same order for different headform sizes because the larger bubble interactions on the larger headform significantly reduce the event rate at lower cavitation numbers. Also plotted in the figure are the experimental observations of cavitation event rates in the Large Cavitation Channel in Memphis by Kuhn de Chizelle *et al.* (1992). The nuclei population was not measured in those experiments. However, the comparisons show that even with the assumed characteristic nuclei distribution in the calculations, the model still qualitatively predicts the scaling of the event rate with the headform size and the cavitation number. But there are also two substantial discrepancies. First, the tunnel velocity effect produced by the model is not consistent with that observed experimentally, having a different sign in the experiments. Second, the calculated event rates are about an order of magnitude larger than those observed experimentally at lower cavitation numbers.

The information on event rates can be used to produce cavitation inception numbers simply by selecting a certain event rate criterion for inception. Figure 5.7 shows the predicted cavitation inception numbers for various body sizes and various velocities based on an arbitrarily chosen critical event rate of $10 events/sec$. Also plotted in the figure are the experimental observations of Kuhn de Chizelle *et al.* (1992). Comparing the predicted and measured cavitation inception numbers, we note that the trends with changing headform size are consistent. Moreover, the predicted values are also close to those experimentally observed. But the change of the predicted inception numbers with velocity are the reverse of those observed experimentally.

The predicted maximum bubble size as a function of the cavitation number is shown in Figure 5.8. Also plotted are the observations of the maximum bubble size on three different Schiebe headforms observed by Kuhn de Chizelle *et al.* (1992). Since the actual bubble is not spherical, the experimental observed bubble radius is defined as the equivalent radius of a sphere that has the same volume of the actual bubble. As shown the figure, substantial agreement is achieved between the predicted and observed dimensionless maximum bubble size.

The predicted maximum bubble size distribution on the headform is shown in Figure 5.9. Experimental observations by Ceccio and Brennen (1992) are also plotted in the figure. As shown in the figure, the predicted maximum bubble size range is quite similar to that observed. And the predicted values of the distribution are also similar to those observed. However, the shape of the predicted maximum bubble size distribution departs from the experimental observations in the number of peaks. The observed distributions often show several maxima, but these peaks can not be simulated by the model.

Using the characteristic nuclei number density distribution, we identified a number of major effects, all of which tend to reduce the cavitation event rate. Now we compare the predicted cavitation event rates with those experimentally observed. Figure 5.10 and 5.11 present comparisons between the experimentally measured event rates and the predictions using the simultaneously measured nuclei distributions (both the concentration and the shape). Note that the event rates are in rough agreement at the larger cavitation numbers, but that a progressively increasing discrepancy develops as the cavitation number decreases and the event rate increases.

5.5 Conclusions

The present chapter describes an investigation of the relationship between the nuclei number distributions in a water tunnel and the cavitation event rates on some axisymmetric headforms. A simple analytical model is presented for the connection between the nuclei distribution and the event rate. Similar in concept to the numerical model presented by Meyer *et al.* (1992), it has the advantage of ease of calculation and adaptation to other flows. The effects of the reduction in volume flow due to the boundary layer, of the bubble screening near the stagnation point, of the interactions between bubbles and of a minimum observable cavitation bubble size are examined and included in the model. Among all these effects, the bubble screening effect results in the largest reduction in the cavitation event rate and the effect of the bubble/bubble interactions becomes more important with increasing body size and decreasing cavitation number. The result of the combination of these effects can be a reduction in the event rate of an order of magnitude.

The scaling of the predicted cavitation event rate with body size, cavitation number and

nuclei population agrees with the experimental observations. At larger cavitation numbers, the predicted cavitation event rates agree quantitatively with the experimental observations in the Low Turbulence Water Tunnel and the High Speed Water Tunnel. However, two outstanding issues still remain. First, the observed event rates at lower cavitation numbers are about an order in magnitude smaller than one would predict based on the actual nuclei distributions. This may be due to the fact that only a fraction of the observed nuclei actually cavitate or it may be due to some other effect which is not included in the model. A more detailed study is needed to confirm this. Second, the changes in the event rate with tunnel velocity can not be explained at present.

It is clear that the cavitation inception criteria are a natural consequence of the event rate variations described above. When the model for the event rates is used with some chosen criterion to predict the cavitation inception number, the results are consistent with those observed experimentally insofar as the trend with headform size is concerned. The trend with velocity is, of course, at odds with the experiments because of the same discrepancy in the event rate.

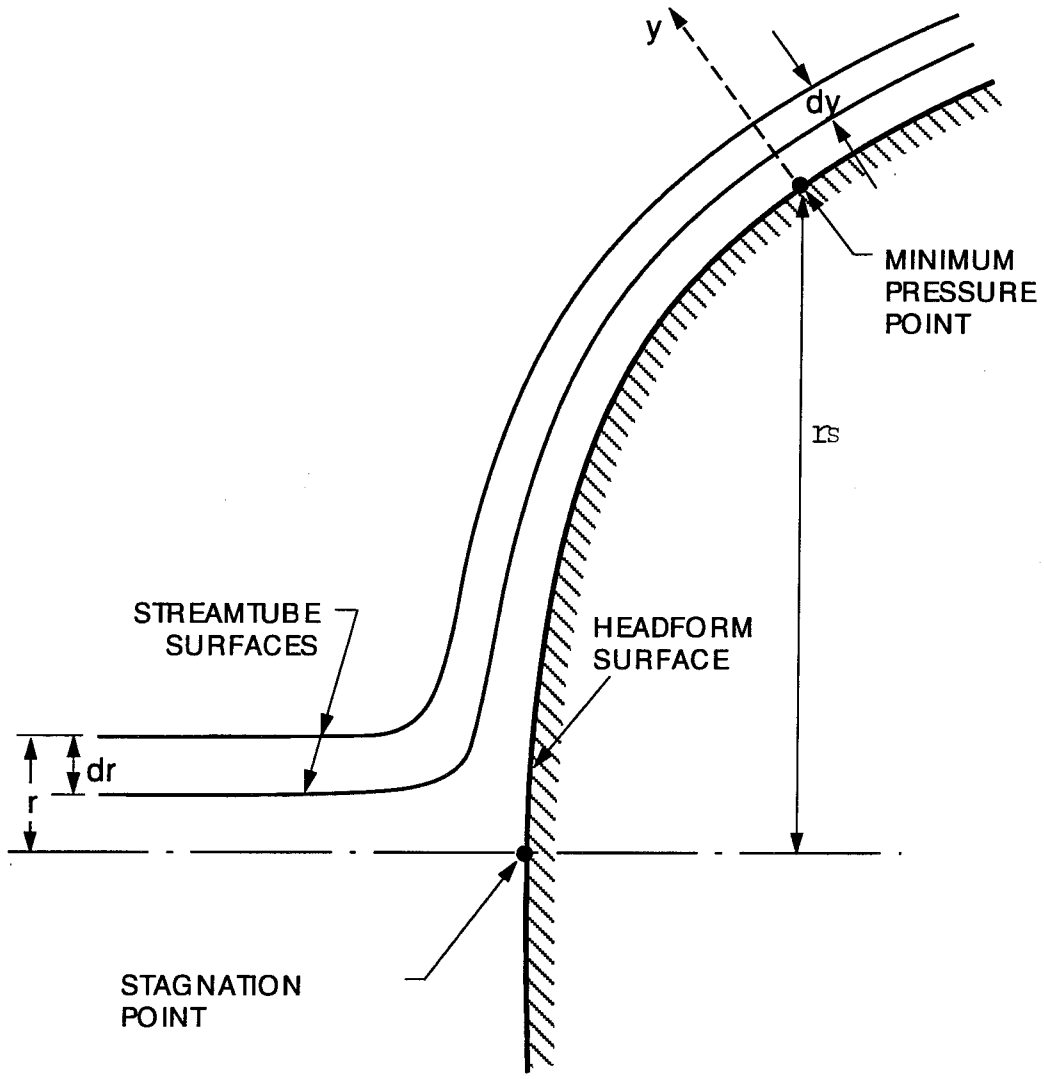

Figure 5.1: A schematic showing typical annular stream tube upstream and in the neighborhood of the minimum pressure point.

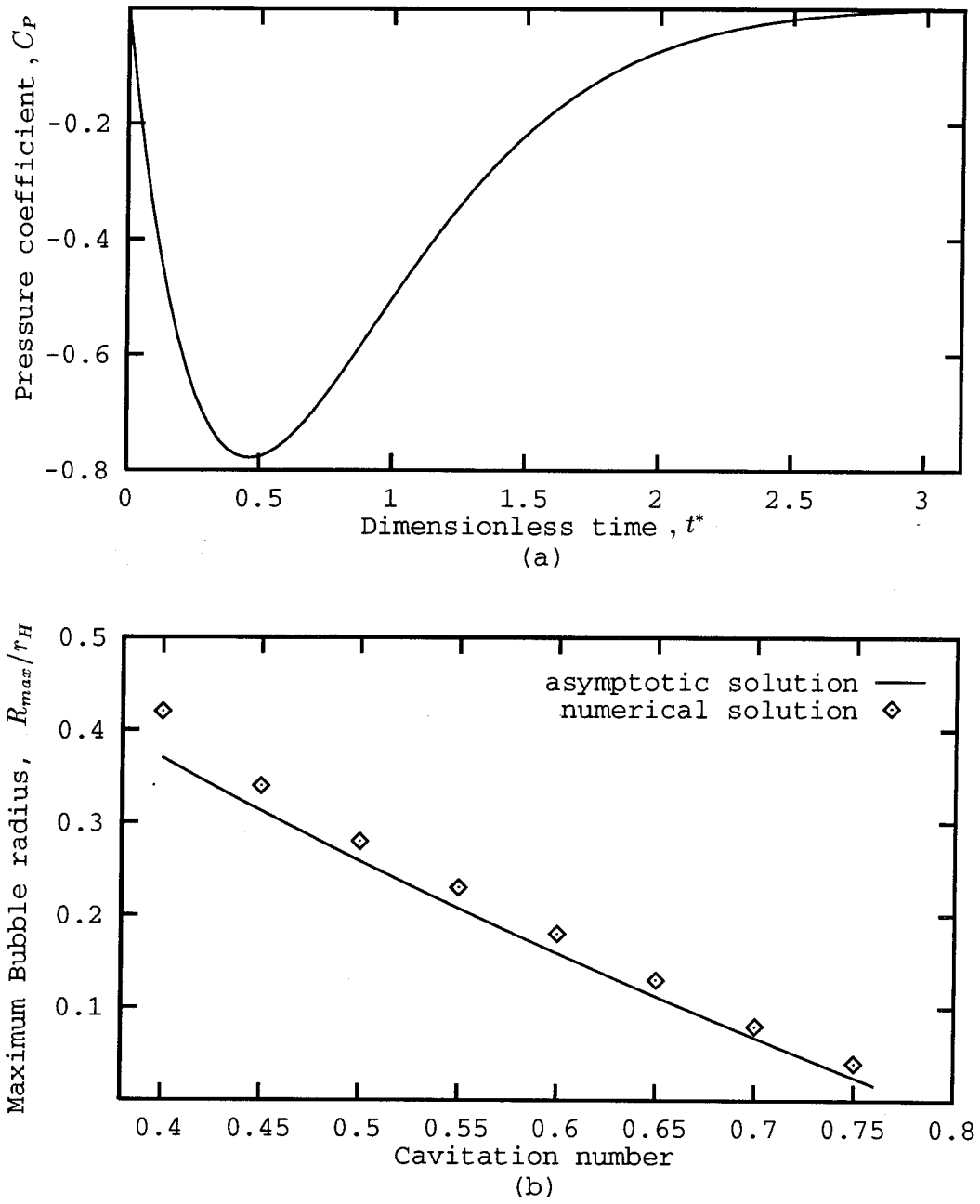

Figure 5.2: A comparison of the maximum bubble sizes obtained by asymptotic equation and numerical solution of Rayleigh-Plesset equation: (a) the pressure distribution used in the calculation; (b) the maximum bubble size plotted against cavitation number.

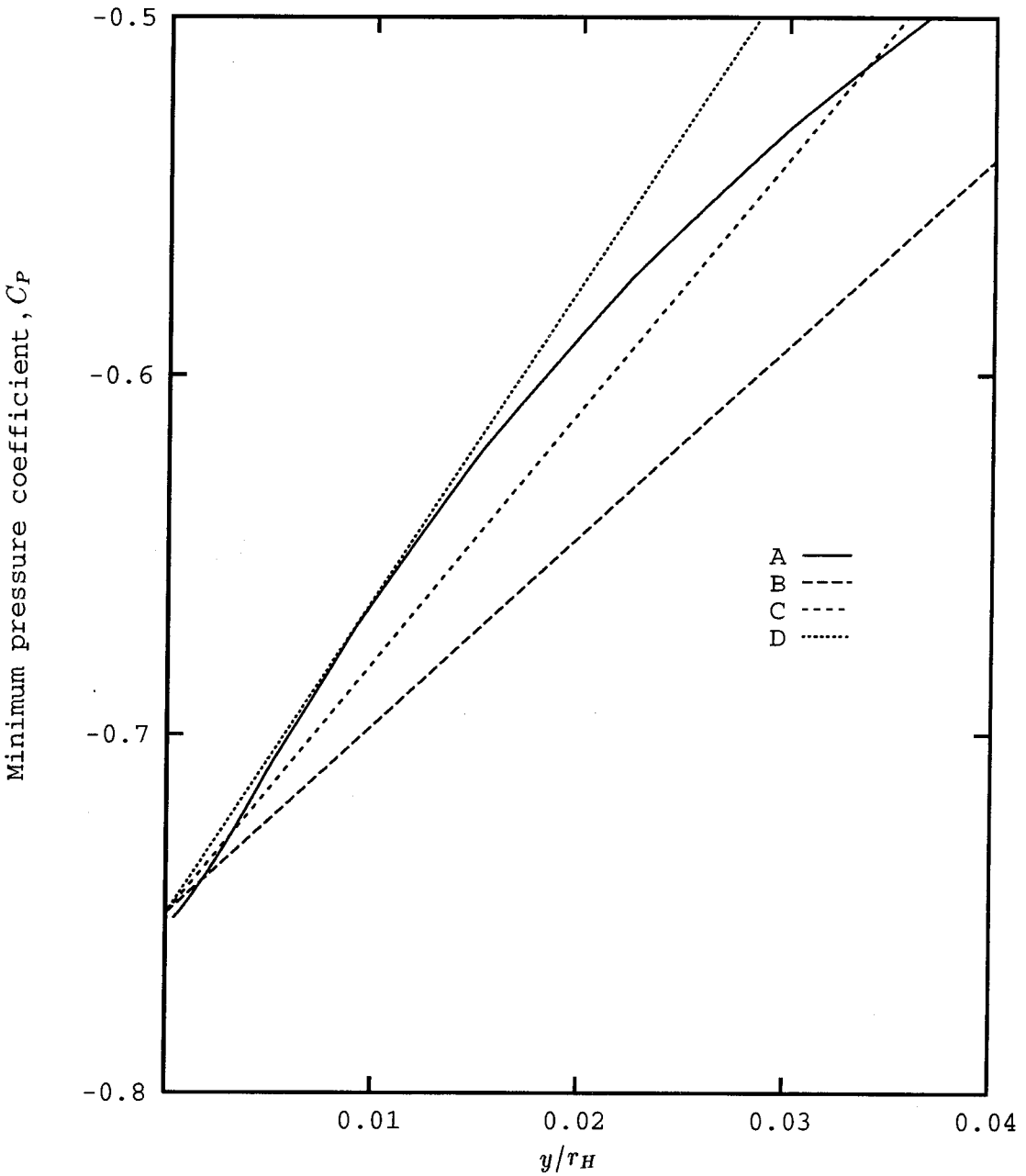

Figure 5.3: Variation in the minimum pressure coefficient, C_{PM}, on a streamline with the distance y of that streamline from the surface of the body near the minimum pressure point. **(A)**: Potential flow solution, **(B)**: $r_H/r_K = 1.5$, **(C)**: $r_H/r_K = 2.0$, **(D)**: $r_H/r_K = 2.5$.

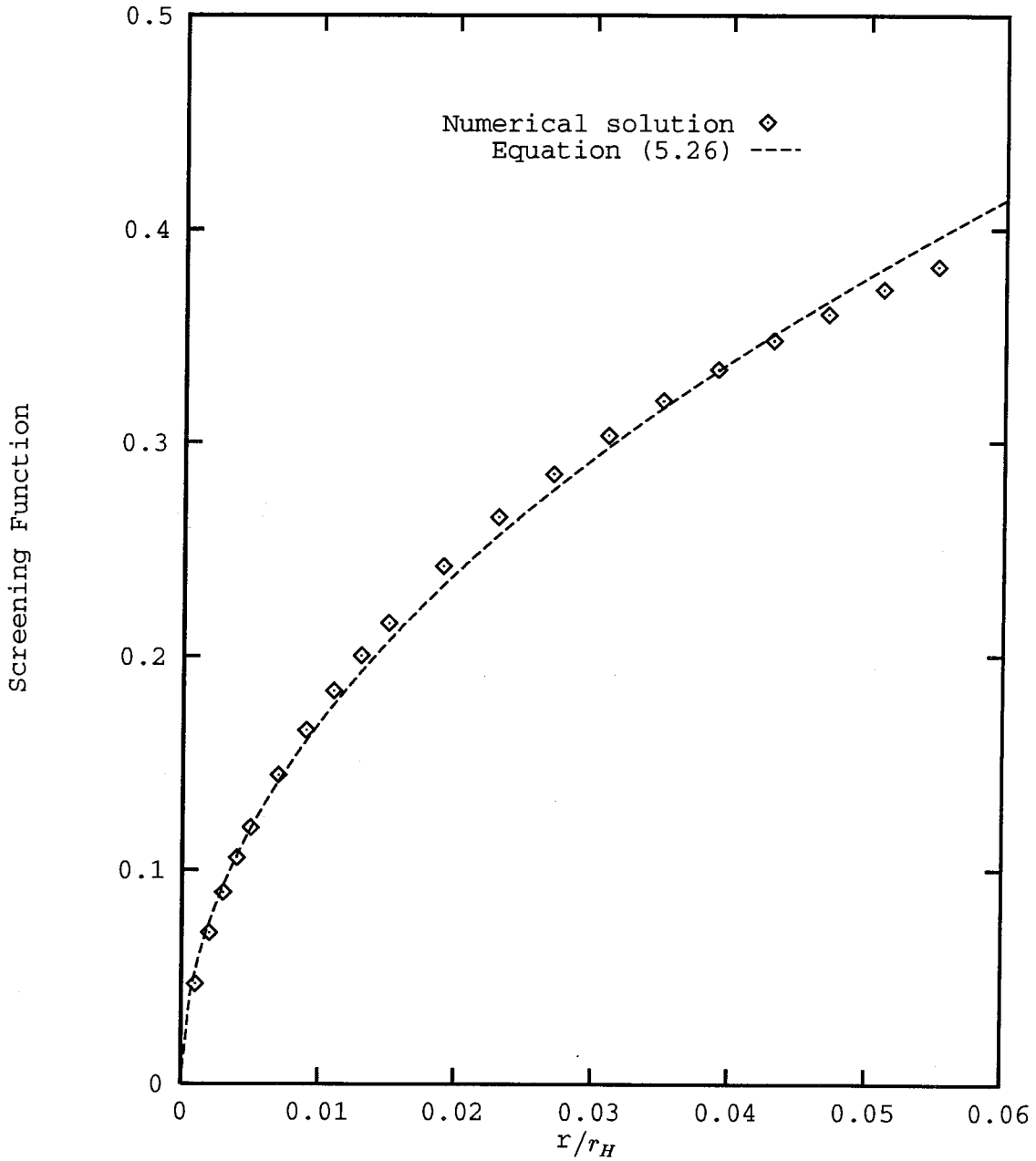

Figure 5.4: The function $\Sigma(r/r_H)$ for the stagnation point flow in the potential flow around a sphere.

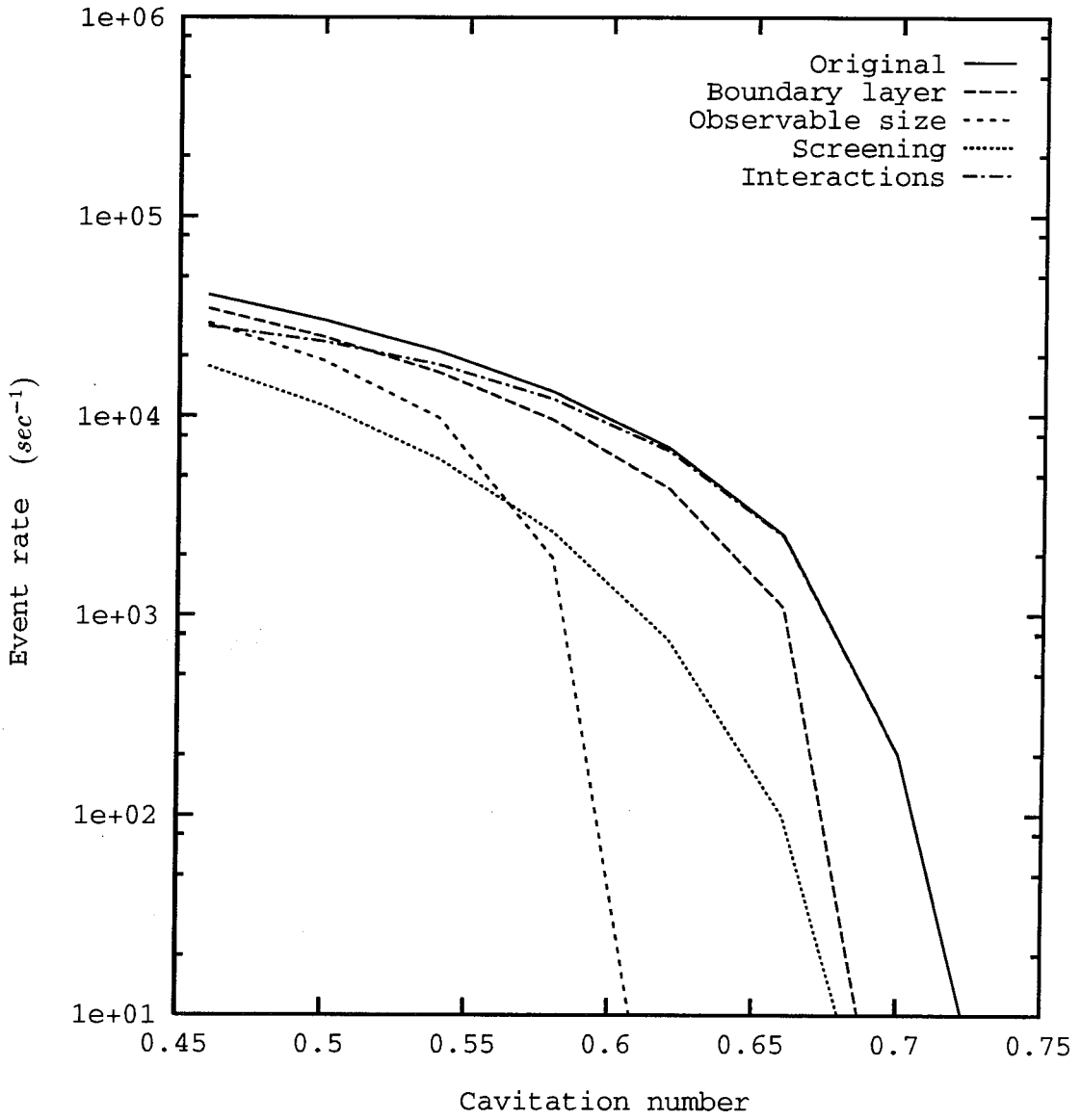

Figure 5.5: Typical event rates calculated using an assumed but typical nuclei distribution for flow around a 5.08cm Schiebe body at a velocity of 9m/sec. **Original**: Basic method not including the additional effects included in other lines. **Boundary layer**: As original but including the boundary layer flux effect. **Observable size**: As original but including only "observable" bubbles larger than 1mm in radius. **Screening**: As original but including the bubble screening effect. **Interactions**: As original but including the bubble interaction effect.

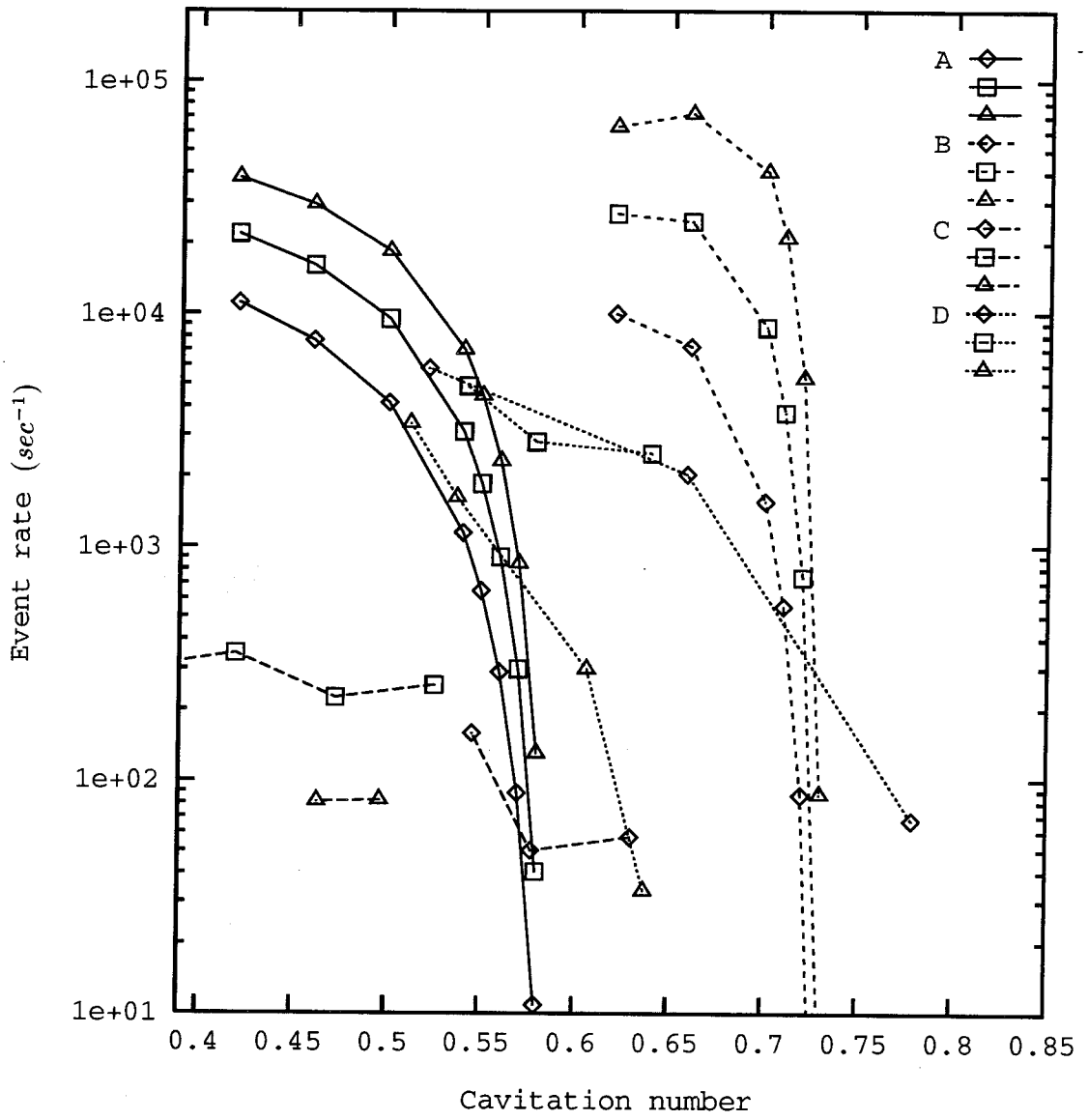

Figure 5.6: Calculated cavitation event rates on Schiebe headforms for the $5cm$ (**A**) and $50cm$ (**B**) headforms at $9m/sec$ ($\diamond$), $11.5m/sec$ ($\square$) and $15m/sec$ ($\triangle$). The effects of the boundary layer flow rate, bubble screening, bubble interactions and finite bubble size are included in the calculations. Also plotted are the observations of Kuhn de Chizelle *et al.* (1992) on Schiebe headforms ($5cm$: **C** and $50cm$: **D**).

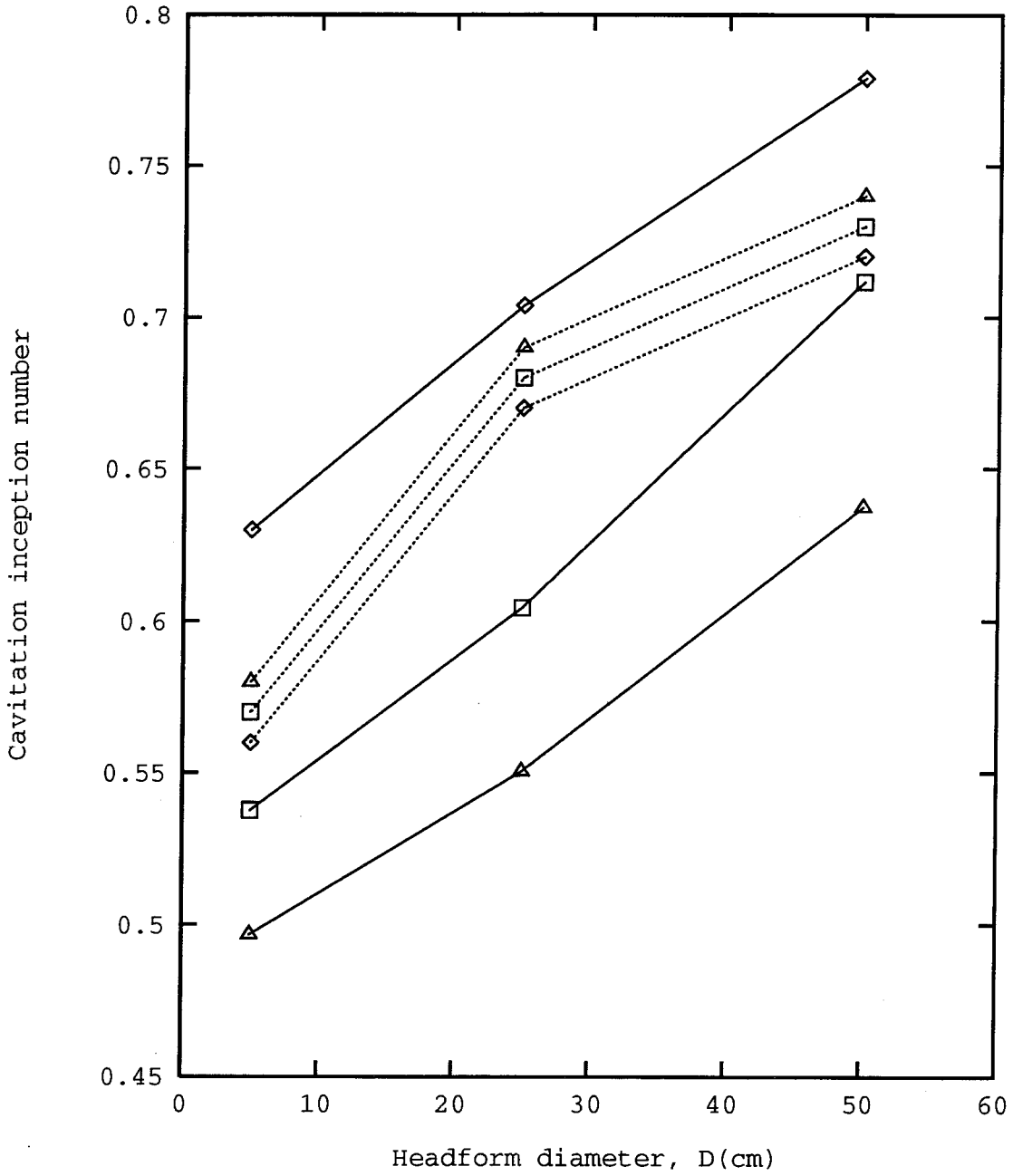

Figure 5.7: A comparison of the predicted (dotted lines) and observed (solid lines, Kuhn de Chizelle *et al.*, 1992) cavitation inception numbers for various tunnel velocities (9 m/sec ($\diamond$), 11.5 m/sec ($\square$), and 15 m/sec ($\triangle$)) and headform diameters.

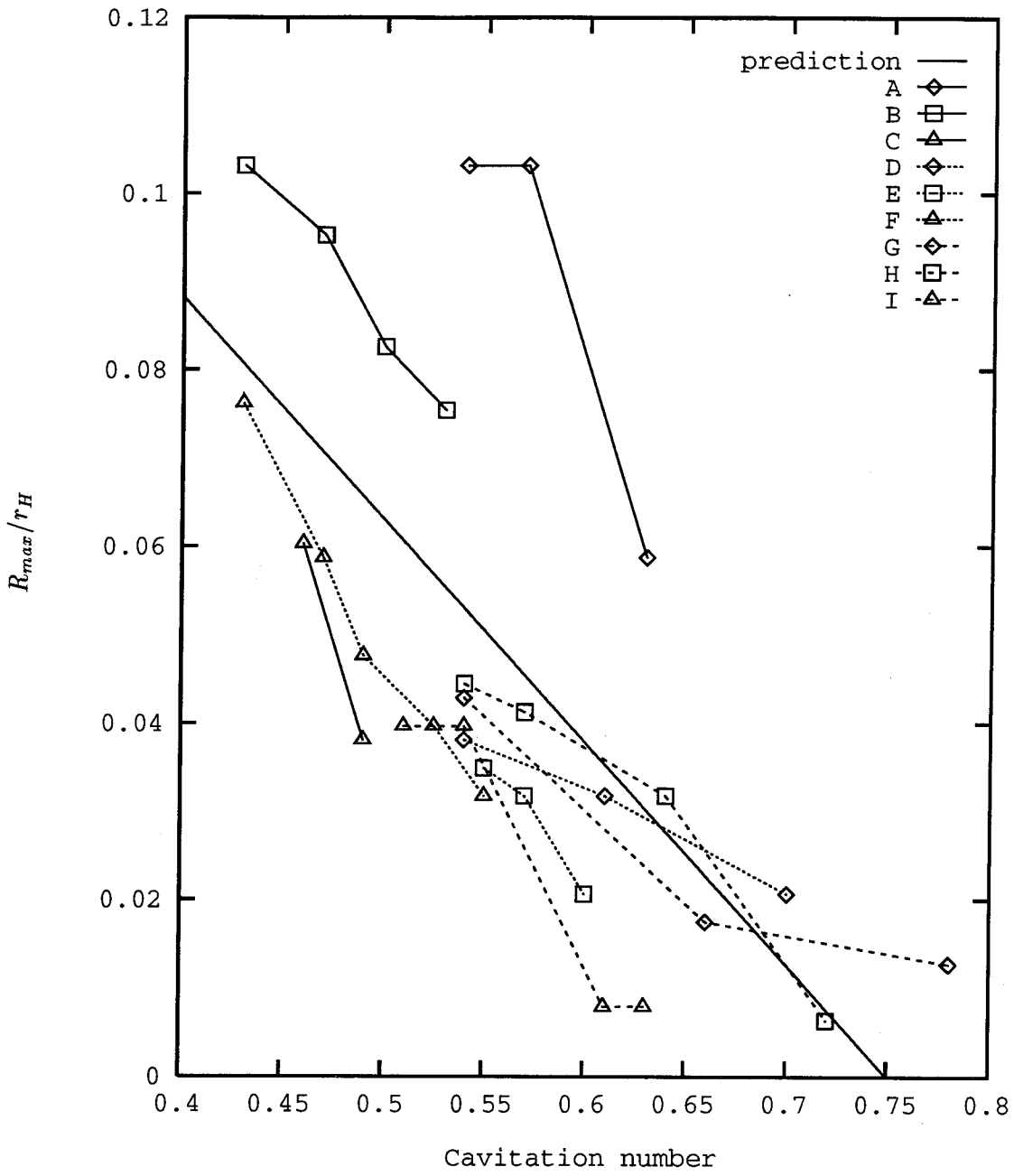

Figure 5.8: Variations of maximum bubble size with the cavitation number. Also plotted are experimental observations on three different size Schiebe bodies (5*cm*: solid lines (**A, B, C**); 25*cm*: dotted lines (**D, E, F**); 50*cm*: dotted lines (**G, H, I**)) at different velocities (9 m/sec (◇), 11.5 m/sec (□), and 15 m/sec (△)).

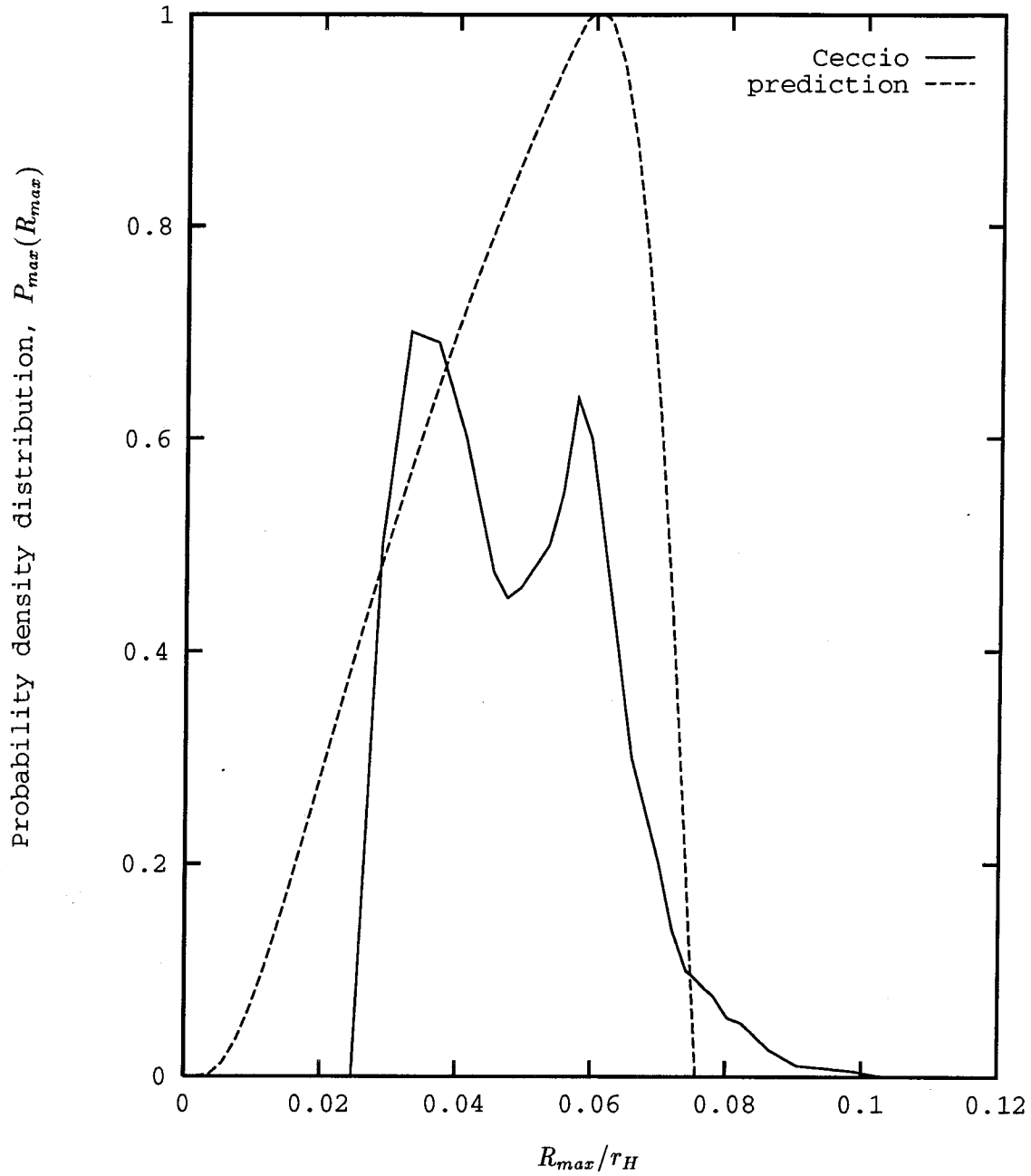

Figure 5.9: The predicted probability density distribution (dashed line) of maximum bubble size on the Schiebe headform at a velocity of $9m/sec$ and a cavitation number of 0.45. Also plotted are experimental observations (solid line) of Ceccio and Brennen (1992).

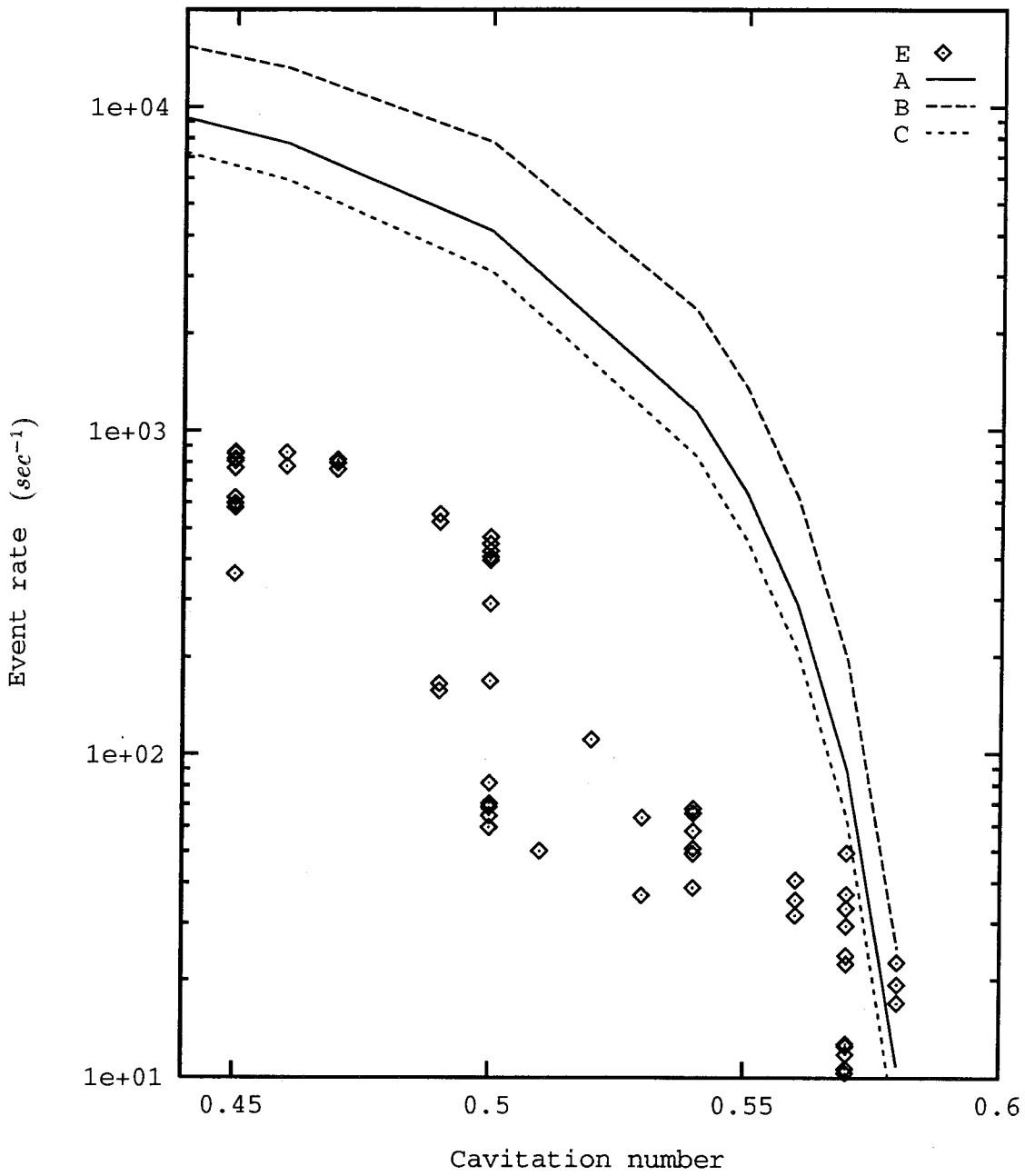

Figure 5.10: A comparison of observed cavitation event rates ($\diamond$) on a 5.08cm Schiebe body in the Low Turbulence Water Tunnel at a speed of $9m/sec$ with anticipated event rates based on simultaneously measured nuclei distributions. The numerical results are plotted as (**A**): event rates calculated using intermediate nuclei concentrations, (**B**): event rates calculated using the largest nuclei concentrations, (**C**): event rates calculated using the smallest nuclei concentrations.

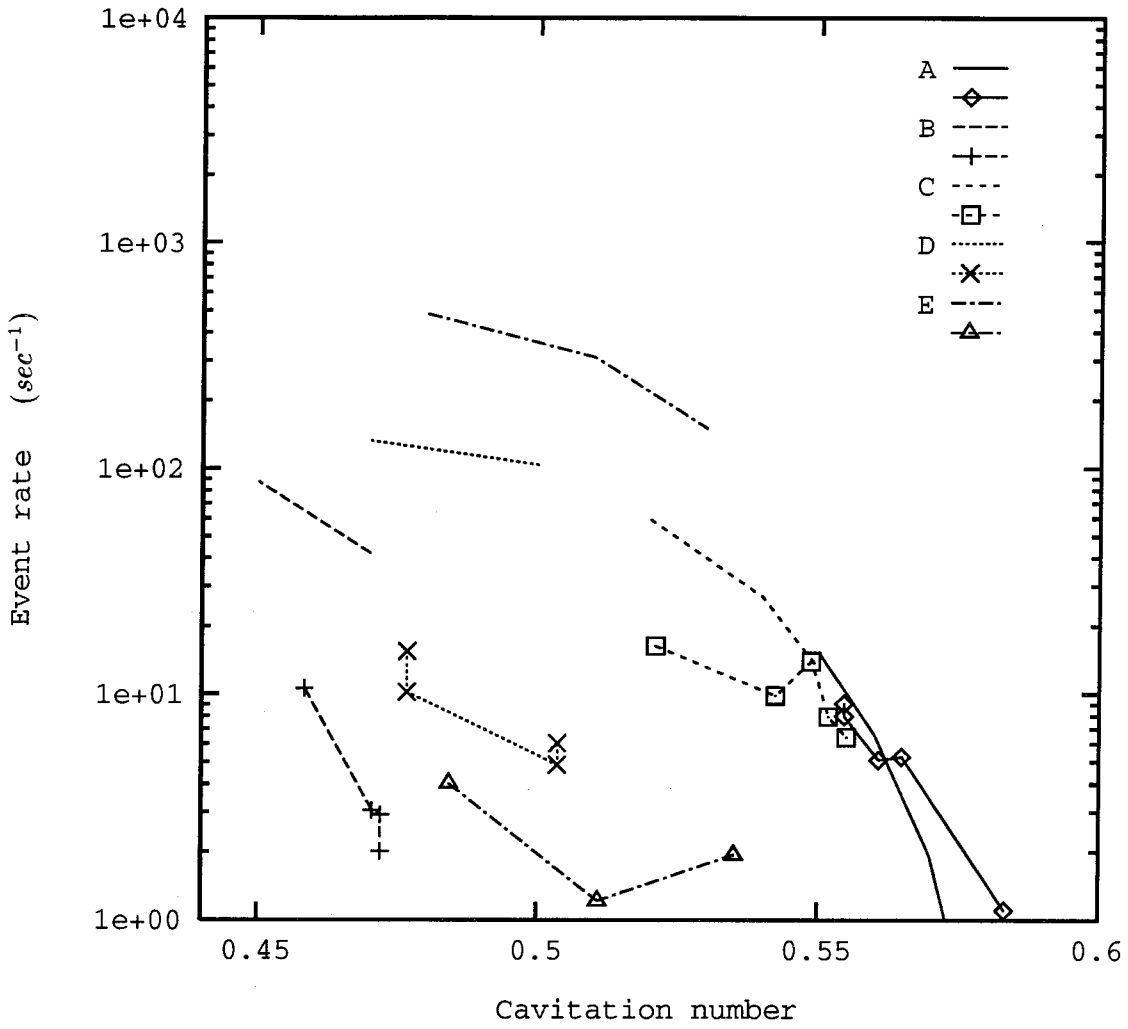

Figure 5.11: A comparison of observed cavitation event rates (lines with symbols) on a $5.08cm$ Schiebe body in the High Speed Water Tunnel at various speeds and nuclei concentrations with the anticipated event rates (corresponding lines without symbol) based on simultaneously measured nuclei distributions. The data is plotted for various tunnel speeds and nuclei concentrations as follows: (**A**): $U = 8.1m/sec$, $3.6 < C < 4.3cm^{-3}$, (**B**): $U = 9.4m/sec, C = 0.8cm^{-3}$, (**C**): $U = 9.4m/sec$, $1.7 < C < 2.4cm^{-3}$, (**D**): $U = 12.6m/sec$, $2.0 < C < 3.0cm^{-3}$, (**E**): $U = 14.5m/sec$, $1.6 < C < 2.9cm^{-3}$.

Chapter 6

Cavitation Noise

6.1 Introduction

Acoustics of cavitation has been a subject of research for more than fifty years. It is known that the violent collapse of cavitation bubbles results in the production of noise as well as the possibility of material damage to nearby solid surfaces (see Harrison, 1952, Chahine, 1979, Marboe *et al.*, 1986, Blake, 1987, Kumar and Brennen, 1991, 1993, Ceccio and Brennen, 1992, and Kuhn de Chizelle *et al.*, 1992). The noise takes the form of positive pulses or spikes. One bubble can produce several pulses or no pulse. The majority of the noise is generated by the violence of the first collapse; the growth phase contributes no measurable noise pulse. The rebound produces a rough bubble that may also collapse to produce a noise pulse of lesser magnitude. It also has been observed that the damage to the nearby surface is largely due to the first pulse. Thus the first pulse is most important for describing the cavitation acoustic intensity. To quantify the first pulse, some researchers have used the peak acoustic pressure. But the peak pressure is difficult to measure accurately since the collapse

happens in a very short period of time (usually less than $100\mu sec$) and is heavily influenced by the compressibility of the surrounding liquid. Here we use the acoustic pressure impulse, which can be measured more accurately and is less influenced by the compressibility of the liquid.

There are two different theoretical approaches to the acoustics of cavitating bubbles. The first one is based on the Rayleigh-Plesset equation and does not include the compressibility of the liquid. The other one is based on the Kirkwood-Bethe equation, in which the compressibility of the liquid is included (Akulichev *et al.* 1968, Esipov and Naugol'nykh, 1972, 1973, and Baiter, 1974). Baiter (1974) argued that the high frequency range of the cavitation noise spectrum is governed by cavitation shock wave noise; while at low frequencies, both monopole type (incompressible model) and shock wave noise (compressible model), may contribute to the cavitation noise spectrum. If the pressure impulse is used to characterize the cavitation acoustic intensity, the two theories will give similar results. Consequently, we choose the incompressible Rayleigh-Plesset model for simplicity.

6.2 Acoustic Impulse

A sketch of the typical variations of the bubble volume and the acoustic pressure with time is presented in Figure 6.1. The amplitude of the acoustic pressure pulse generated from a collapsing bubble can be defined by the impulse, $I(r)$, which is measured at a distance of r from location of the bubble.

$$I(r) = \int_{t_1}^{t_2} (p(t,r) - p_{b\infty})\, dt$$

where p and $p_{b\infty}$ are the local pressure and the pressure at infinity respectively; t_1 and t_2 are the moments when $p(t,r) - p_{b\infty} = 0$.

A dimensionless impulse is defined by

$$I^*(r) = \frac{4\pi}{\rho_L U r_H} I \tag{6.1}$$

Regarding a cavitation bubble as an acoustic monopole, the acoustic pressure produced in the far field is

$$p(r,t) - p_{b\infty} = \frac{\rho_L}{4\pi r} \frac{d^2 V(t - \frac{r}{c_0})}{dt^2} \tag{6.2}$$

where $V = \frac{4}{3}\pi R^3$ is the bubble volume.

It follows that the dimensionless impulse, I^*, is

$$\begin{aligned} I^*(r) &= \frac{1}{U r_H^2} (\frac{r_H}{r}) \int_{t_1}^{t_2} \frac{d^2 V}{dt^2} dt \\ &= \frac{1}{U r_H^2} (\frac{r_H}{r}) \left[\left(\frac{dV}{dt} \right)_{t_2} - \left(\frac{dV}{dt} \right)_{t_1} \right] \end{aligned} \tag{6.3}$$

Referring to Figure 6.1, we consider the volume changes of a typical cavitation bubble on a Schiebe headform. A bubble with initial radius R_0 and air content p_{G_0} begins to grow after it encounters the low pressure. When it reaches the maximum radius, R_{max}, the pressure of the gas inside the bubble is equal to P_{G_M}. After entering the high pressure region, the bubble collapses under a certain pressure p_x. Its volume shrinks dramatically in a very short time. Furthermore, we assume that $\dot{V}(t)$ is symmetric at t_1 and t_2, i.e., $\dot{V}(t_1) = -\dot{V}(t_2)$. Then from equation (6.3) we have

$$\begin{aligned} I^*(r) &= \frac{-2}{U r_H^2} (\frac{r_H}{r}) \left(\frac{dV}{dt} \right)_{t_1} \\ &= \frac{-8\pi}{U r_H^2} (\frac{r_H}{r}) \left(R^2 \dot{R} \right)_{t_1} \end{aligned} \tag{6.4}$$

If the bubble radius at times t_1 is denoted as R_x and the bubble wall velocity is denoted as $\dot{R}_x$, from $\ddot{V}(t_1) = 0$ we have

$$R_x^2 \ddot{R}_x + 2R_x \dot{R}_x^2 = 0 \tag{6.5}$$

Substitute Rayleigh-Plesset equation (5.1) into the above equation, and we have

$$\frac{\dot{R}_x^2}{2} = \frac{(p_x - p_v)}{\rho_L} + \frac{2S}{\rho_L R_x} - \frac{p_{G_M}}{\rho_L}\left(\frac{R_{max}}{R_x}\right)^{3k} \tag{6.6}$$

From equation (5.5),

$$\dot{R}_x^2 = \frac{2(p_v - p_x)}{3\rho_L}\left[1 - (\frac{R_{max}}{R_x})^3\right] + \frac{2p_{G_M}}{3\rho_L(1-k)}\left[(\frac{R_{max}}{R_x})^{3k} - (\frac{R_{max}}{R_x})^3\right] - \frac{2S}{\rho_L R_x}\left[1 - (\frac{R_{max}}{R_x})^2\right] \tag{6.7}$$

Combining equation (6.6) and (6.7), we have

$$\begin{aligned}&\left[\frac{p_x - p_v}{3} - \frac{P_{G_M}}{3(1-k)} + \frac{S}{R_{max}}\right]\left(\frac{R_{max}}{R_x}\right)^3 \\ &+\frac{p_{G_M}(4-3k)}{3(1-k)}\left(\frac{R_{max}}{R_x}\right)^{3k} - \frac{3S}{R_{max}}\left(\frac{R_{max}}{R_x}\right) - \frac{4(p_x - p_v)}{3} = 0\end{aligned} \tag{6.8}$$

For most situations of bubble collapse, p_x is close to the upstream pressure, p_∞. For example, Kuhn de Chizelle *et al.* (1992) observed that the pressure, p_x, at which a cavitation bubble collapses on a Schiebe headform is given approximately by

$$C_{Px} + \sigma = 0.6(-C_{PMS} - \sigma) \tag{6.9}$$

This indicates p_x is the same order of magnitude as p_∞. Because R_{max} is much bigger than the original bubble radius R_0, we can make the following estimates of the relative magnitudes:

$$\begin{aligned}p_x - p_v &\gg \frac{S}{R_{max}} \\ p_x - p_v &\gg p_{G_M}\end{aligned} \tag{6.10}$$

Substituting equation (6.10) into equation (6.8) and neglecting the smaller terms, we have

$$\frac{R_{max}}{R_x} \approx 4^{1/3} \approx 1.58 \tag{6.11}$$

Ceccio and Brennen (1992) did numerical computations of a cavitation bubble on a Schiebe body. The results from their computations for R_{max}/R_x are about 1.64, which is close to the above asymptotic estimation. Note that at t_1 the bubble radius is about half the maximum bubble radius. Fitzpatrick and Strasberg (1956) argued that the compressibility of the liquid is important only in the later stage of the process of a bubble collapse, when the bubble radius is much less than the original radius ($R/R_0 < 0.01$). Since at t_1, the starting point of the pressure impulse, the bubble radius is close to the original bubble radius, the compressibility of the liquid is negligible. Thus the impulse predicted by incompressible model should be very close to the actual situation.

Substituting equation (6.11) and equation (6.7) into equation (6.3) and neglecting the smaller terms, we have the dimensionless pressure impulse:

$$I^* = 3.20\pi \left(\frac{r_H}{r}\right) (C_{Px} + \sigma)^{1/2} \left(\frac{R_{max}}{r_H}\right)^2 \tag{6.12}$$

This expression can be used to calculate the pressure impulse for general bubble collapse, provided that the maximum bubble radius and the environment pressure are known.

Many researchers (Fitzpatrick and Strasberg, 1956, Hamilton, 1982, Vogel, 1989, Kuhn de Chizelle *et al.*, 1993 and Brennen 1994) have anticipated that the noise correlates with the maximum bubble volume. Consequently, we also write equation (6.12) in the form

$$I^* = 1.23\pi \left(\frac{r_H}{r}\right) (C_{Px} + \sigma)^{1/2} \left(\frac{V_{max}}{r_H^3}\right)^{2/3} \tag{6.13}$$

where $V_{max} = \frac{4}{3}\pi R_{max}^3$ is the maximum bubble volume.

Using equation (6.9), we obtain the dimensionless pressure impulse for a Schiebe body,

$$\begin{aligned} I^* &= 2.48\pi \left(\frac{r_H}{r}\right)(-C_{PMS}-\sigma)^{1/2}\left(\frac{R_{max}}{r_H}\right)^2 \\ &= 0.96\pi \left(\frac{r_H}{r}\right)(-C_{PMS}-\sigma)^{1/2}\left(\frac{V_{max}}{r_H^3}\right)^{2/3} \end{aligned} \tag{6.14}$$

The upper limit for the pressure impulse on a Schiebe body is obtained by substituting the equation (5.36) with $y = 0$ into equation (6.12).

$$\begin{aligned} I_m^* &= 2.48\pi(\frac{r_H}{r})(-C_{PMS}-\sigma)^{1/2}\left[\frac{2}{\sqrt{3}C_{P1}^{*\frac{1}{2}}}\frac{(-C_{PMS}-\sigma)}{(1-C_{PMS})^{1/2}}\right]^2 \\ &= \frac{10.39}{C_{P1}^*(1-C_{PMS})}(\frac{r_H}{r})(-C_{PMS}-\sigma)^{5/2} \end{aligned} \tag{6.15}$$

6.3 Impulse Width and Magnitude

The impulse width is defined as the time between t_1 and t_2. It is also the time it takes for the bubble to shrink from R_x to 0. From equation (5.10), the impulse width, t_i, is

$$t_i = R_{max}\int_{R_x/R_{max}}^{0} -\left[\frac{2(p_v-p_x)(1-x^{-3})}{3\rho_L}+\frac{2p_{G_M}(x^{-3k}-x^{-3})}{(1-k)\rho_L}-\frac{2S(x^{-1}-x^{-2})}{\rho_L R_{max}}\right]^{-\frac{1}{2}} dx \tag{6.16}$$

Substituting $R_x/R_{max} = 0.63$ into (6.16), we have

$$t_i = R_{max}\int_{0.63}^{0} -\left[\frac{2(p_v-p_x)(1-x^{-3})}{3\rho_L}+\frac{2p_{G_M}(x^{-3k}-x^{-3})}{(1-k)\rho_L}-\frac{2S(x^{-1}-x^{-2})}{\rho_L R_{max}}\right]^{-\frac{1}{2}} dx \tag{6.17}$$

The integrand approaches zero as x approaches zero. Therefore, the major contribution to the above integral occurs when x is close to 0.63. When $x \sim 0.63$ the last two terms are relatively small (referring to equation (6.10)) and can be neglected. Therefore,

$$t_i \approx R_{max}\int_{0.63}^{0} \frac{-dx}{\sqrt{(\frac{1}{x^3}-1)\frac{2(p_x-p_v)}{3\rho_L}}} \tag{6.18}$$

It follows that

$$t_i = 0.232\frac{R_{max}}{U}\frac{1}{(C_{Px}+\sigma)^{1/2}} \tag{6.19}$$

Equation (6.19) can be applied to calculate the duration for general bubble collapse. Since the last two terms in the integral (6.17) are neglected in the approximation, equation (6.19) overestimates the impulse width. Blake (1977) and Arakeri (1985) used a similar expression, but with a constant of order unity.

Using equation (6.9), the impulse width for bubble collapse on a Schiebe headform, can be expressed as

$$t_i = 0.300\frac{R_{max}}{U}\frac{1}{(-C_{PMS}-\sigma)^{1/2}} \tag{6.20}$$

and the dimensionless impulse width is given by

$$t_i^* = \frac{t_i U}{r_H} \tag{6.21}$$

$$= 0.300\left(\frac{R_{max}}{r_H}\right)\frac{1}{(-C_{PMS}-\sigma)^{1/2}} \tag{6.22}$$

We can also write the impulse width as a function of the maximum bubble volume:

$$t_i^* = 0.186\left(\frac{V_{max}}{r_H^3}\right)^{1/3}\frac{1}{(-C_{PMS}-\sigma)^{1/2}} \tag{6.23}$$

The average acoustic pressure level is easily obtained by dividing the impulse, I, by the impulse width, t_i,

$$\bar{p}_i = \frac{I}{t_i} \tag{6.24}$$

$$= 3.45\rho_L U^2(\frac{r_H}{r})(C_{Px}+\sigma)\left(\frac{R_{max}}{r_H}\right)$$

According to this expression, the average acoustic pressure generated by a cavitating bubble is proportional to the bubble size and to the difference between the vapor pressure and the environment pressure.

6.4 Total Acoustic Emission

The total acoustic pressure level for cavitation on a headform is the product of the acoustic impulse of a single bubble and the event rate, given by (5.19).

$$\begin{aligned} p_l &= I\dot{E} \\ &= \frac{\rho_L U r_H}{4\pi} 2.48\pi(-C_{PMS}-\sigma)^{1/2}\left(\frac{r_H}{r}\right)\left(\frac{R_{max}}{r_H}\right)^2 \\ &\quad \int_0^{y_M f_3} 2\pi r_S U(1-C_{PMS})^{\frac{1}{2}} f_1(y) \int_{R_C(y)}^{\infty} \frac{N(R)dR}{f_2(R,y)(1+n_i)} dy \end{aligned} \tag{6.25}$$

where f_1, f_2, f_3, n_i and R_C are defined in last chapter. The event rate expression includes the effects of boundary layer flow rate, bubble screening, finite bubble size and bubble interactions. This is a complicated expression. In order to have some insight into the influence of the physical parameters on the acoustic pressure level, we examine first the simple event rate with $f_1 = 1$, $f_2 = 1$, $f_3 = 1$, $n_i = 0$. Then by using equation (5.36), we have

$$p_l = \rho_L U^2 r_H^3 C \left[\left(\frac{r_H}{r}\right)\right] F_C \tag{6.26}$$

where F_C denotes the combinations of the effects of the headform shape, upstream pressure and the shape of the upstream nuclei number density distribution.

$$F_C = 1.95\left[\left(\frac{r_S}{r_H}\right)\left(\frac{r_K}{r_H}\right)\frac{(-C_{PMS}-\sigma)^{3/2}}{(1-C_{PMS})^{1/2}}\left(\frac{R_{max}}{r_H}\right)^2\right]\left[\int_{R_C}^{\infty}\frac{N(R)}{C}dR\right] \tag{6.27}$$

In equation (6.27) the terms in the first brace represent the effects of headform shape and upstream pressure; the second term represents the effect of the shape of the upstream nuclei density distribution and the critical radius.

For this simple situation, equation (6.26) yields a sound pressure level which scales with U^2 and with r_H^3. This scaling with velocity does correspond roughly to that which has been observed in some experiments on traveling bubble cavitation, for example those of Blake, Wolpert and Geib (1977) and Arakeri and Shangumanathan (1985). The former observe that $p_l \propto U^m$ where m is between 1.5 and 2.

There are, however, complicating factors which can alter these scaling relationships. For example, we have discussed the effect of bubble interactions on the event rate in the last chapter. The discussion also applies to the noise produced. As n_i increases, event rate will become less dependent on nuclei concentration. Therefore, the scaling with nuclei concentration is only valid at large cavitation numbers and small nuclei concentrations. At very small cavitation numbers or large nuclei concentrations, the acoustic pressure level does not scale with nuclei concentration at all. The scaling with velocity is also complicated by the critical bubble radius, R_C, the boundary layer effect and the screening effect. Since both the R_C and the boundary layer thickness decrease as the velocity increases, they tend to make the power, m, somewhat greater than 2. On the other hand, the bubble screening effect increases with the velocity; it tends to make the power, m, less than 2. Similar arguments can be applied to the scaling with headform size.

6.5 Comparisons of Predictions and Observations

We compare the predicted non-dimensional pressure impulse with the observations on the Schiebe headform in the High Speed Water Tunnel in Figure 6.2. During the experiments, the hydrophone was placed at the center of the headform, thus the distance between the hydrophone and the bubble is about the radius of the headform, i.e., $r = r_H$. From equation (6.15),

$$I_m^* = \frac{10.39}{C_{P1}^*(1 - C_{PMS})}(-C_{PMS} - \sigma)^{5/2} \tag{6.28}$$

As shown in the figure, the prediction of the upper limit of pressure impulse covered all experimental results. But the observed pressure impulses are generally smaller that the predicted maximum pressure impulse. The discrepancy increases with a decreasing cavitation number. This is mainly because the interferences between bubbles increase as the cavitation number is decreased. Therefore, the acoustic emission from the collapse of a bubble is weaker at lower cavitation numbers, but this effect is not included in the analytical model.

From equation (6.14), the pressure impulse scales with the two thirds of power of the bubble volume. The variation in the pressure impulse with maximum bubble volume is shown in Figure 6.3. Also plotted in the figure are the experimental observations of Ceccio and Brennen (1992). The trends in the variations of the pressure impulse with maximum bubble volume agree with the experimental observations. At low cavitation numbers the predicted dimensionless pressure impulse quantitatively agrees with the experimental data. However, at large cavitation numbers, the magnitude of the prediction is larger than the observed. This discrepancy is probably due to the assumption that the bubble remains spherical during its collapse. It seems probable that a spherical collapse is the most efficient producer of noise and that the experimentally observed departures from sphericity lead to a

substantial reduction in the noise produced. Kuhn de Chizelle *et al.* (1992) observed that, at low cavitation numbers, the bubble is more spherical than at large cavitation numbers. Thus, at low cavitation numbers, bubble collapse is closer to a spherical bubble collapse.

A comparison of the predicted pressure impulse width with the experimental observations of Ceccio and Brennen (1992) is shown in Figure 6.4. As we can see in the figure, the predictions agree with the experimental observations well, even though the experimental data shows some variations.

6.6 Conclusions

The predicted non-dimensional pressure impulse is a function of maximum bubble volume and cavitation number. It qualitatively predicts the upper limit for the acoustic emission. At lower cavitation numbers, the predicted pressure impulse quantitatively agrees with experimental observations; at larger cavitation numbers it over-predicts the impulse due to the non-spherical bubble collapse at those cavitation numbers. Since the acoustic emission of a spherically symmetric collapse is probably the most efficient noise producing mechanism for a given bubble volume, the analysis of the single bubble pressure impulse overestimates the impulse. Even with this assumption, the prediction of the magnitude of the pressure impulse agrees with the observations. The predicted impulse width also agrees with the experimental observations.

The advantage of the analysis presented is that it reveals the dependence of the acoustic emission on the flow parameters. The total acoustic emission is proportional to the square of the flow velocity and the cube of headform size though various effects such as the boundary layer flow rate effect and the bubble screening effect will modify this scaling.

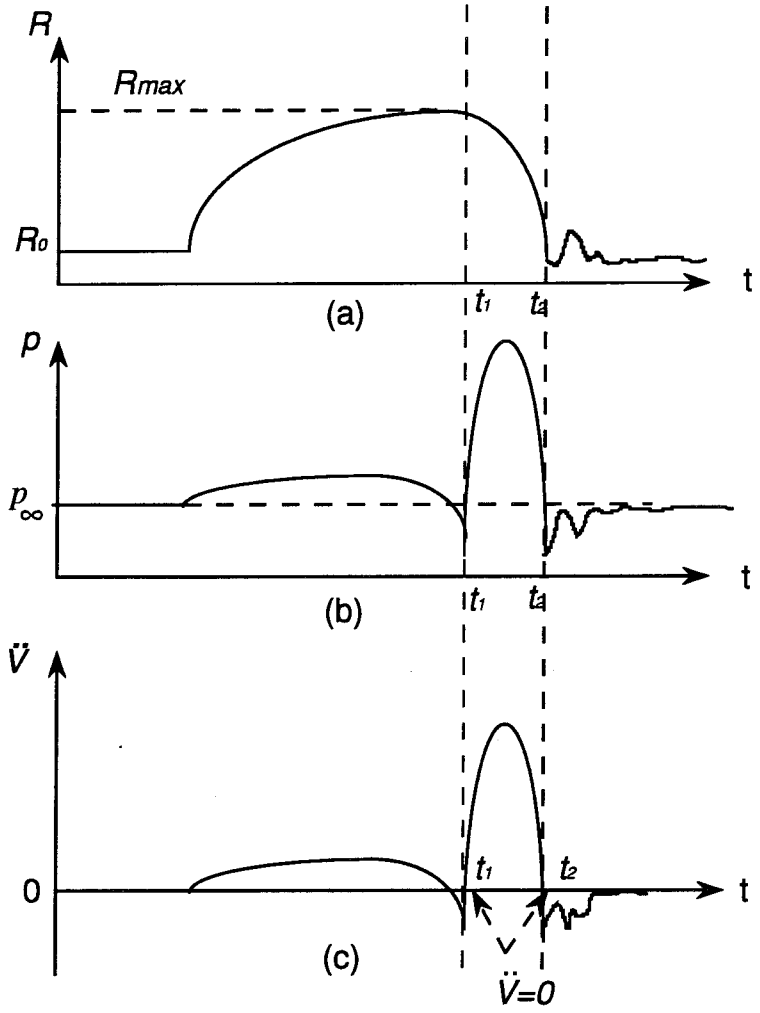

Figure 6.1: A sketch of the variations of the bubble volume and the emitted acoustic pressure as a function of time. (a) Variation of the bubble radius with time, (b) Acoustic pressure generated, (c) Variation of the bubble volume with time.

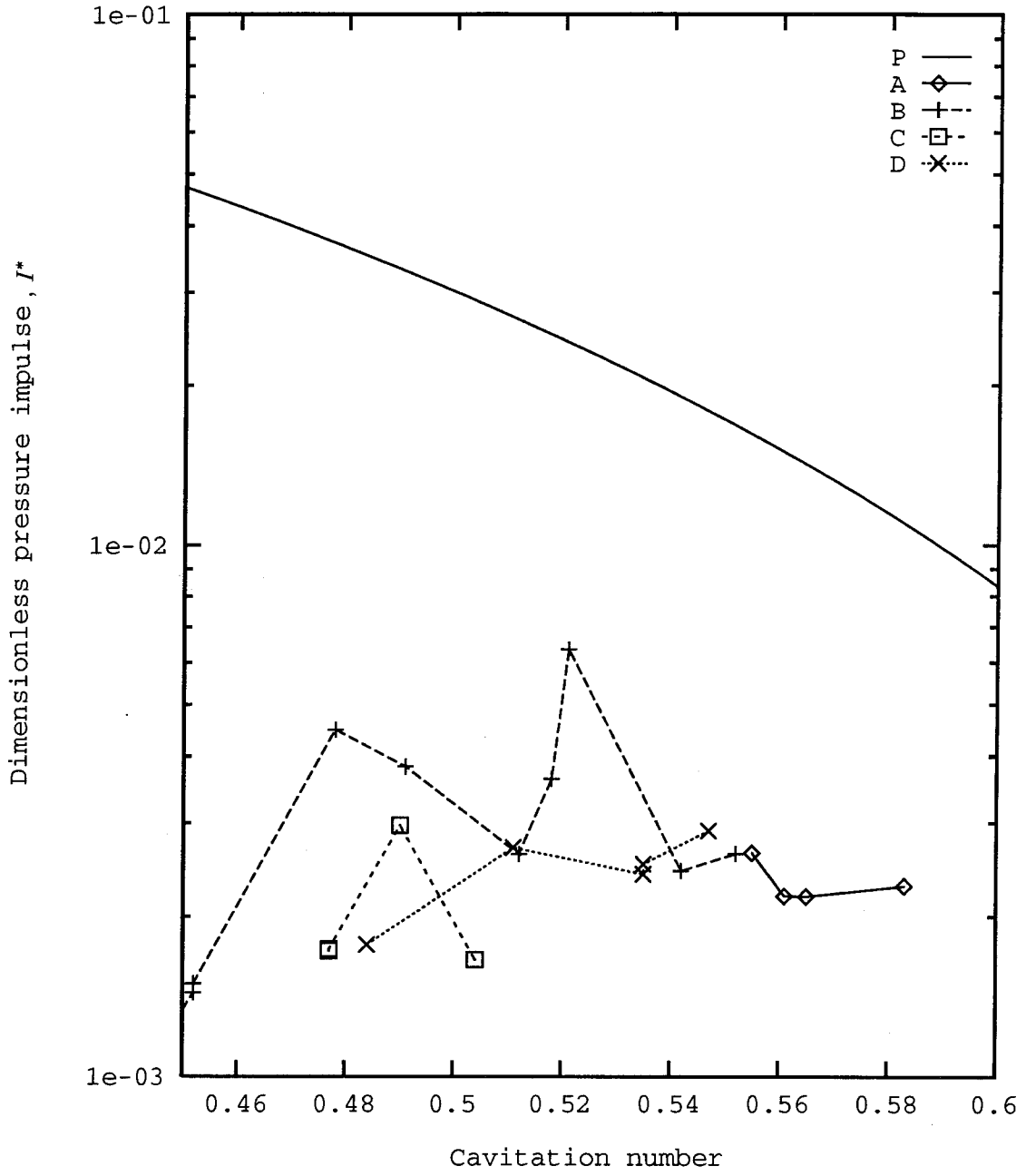

Figure 6.2: A comparison of the predicted (**P**) upper limit of the pressure impulse (I_m^*) and measured pressure impulses in the High Speed Water Tunnel as a function of cavitation number at different tunnel velocities: (**A**): $U = 8.1m/sec$, (**B**): $U = 9.4m/sec$, (**C**): $U = 12.6/sec$, (**D**): $U = 14.4m/sec$.

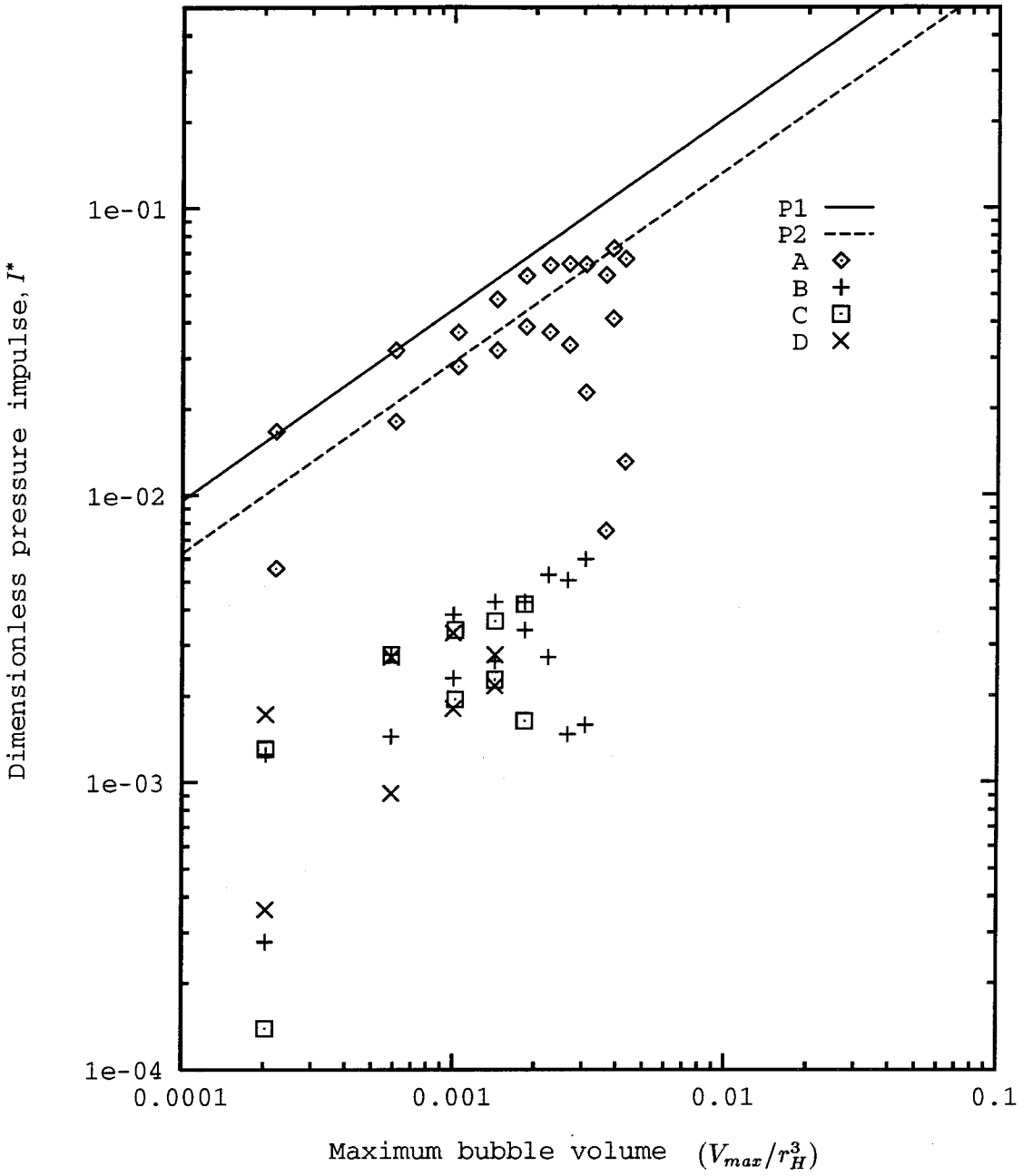

Figure 6.3: Comparisons of the predicted dimensionless pressure impulses, I^*, with experimental measurements on a $5.08cm$ headform by Ceccio and Brennen (1992) as a function of maximum volume of the bubble (divided by r_H^3) at different cavitation numbers. (**P1**): Prediction at $\sigma = 0.4$, (**P2**): Prediction at $\sigma = 0.6$, (**A**): $\sigma = 0.42$, (**B**):$\sigma = 0.45$, (**C**):$\sigma = 0.50$, (**D**):$\sigma = 0.55$.

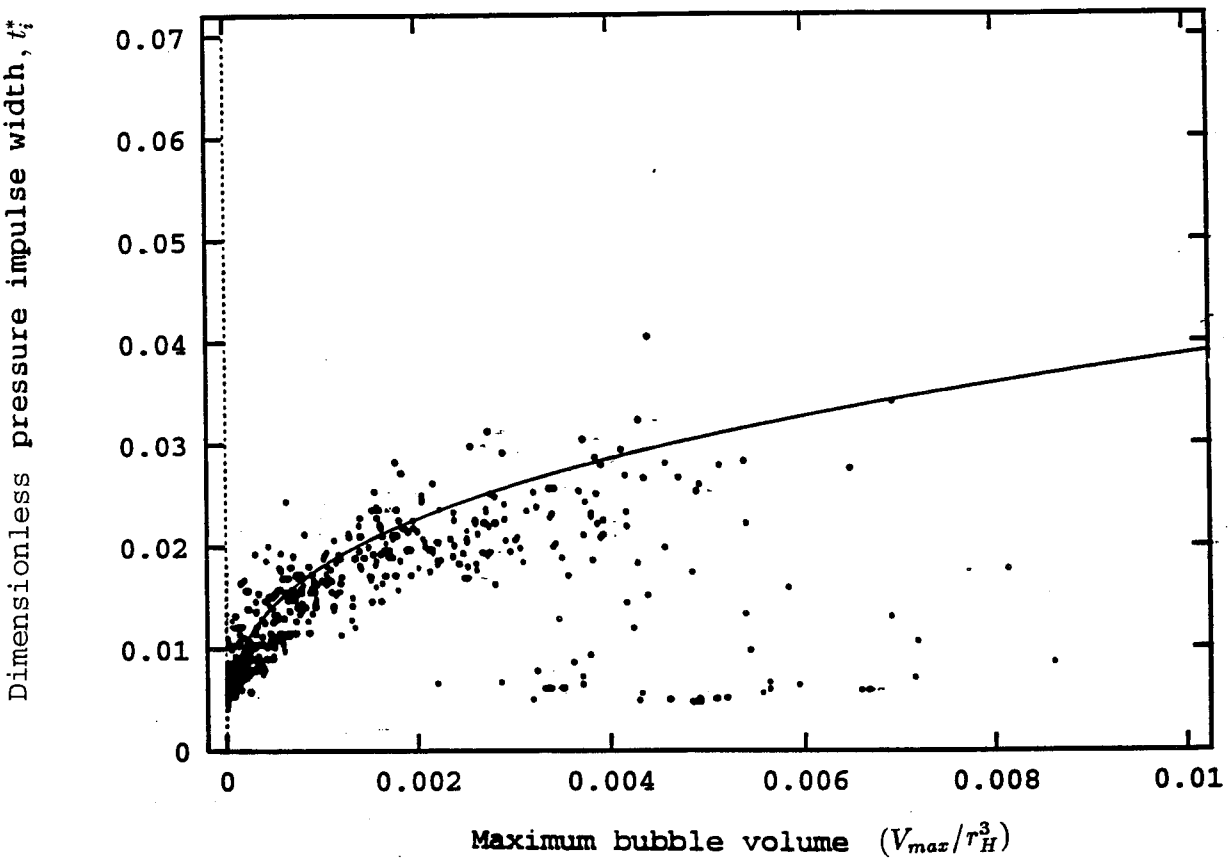

Figure 6.4: A comparison of the predicted (solid line) and the measured (dots) pressure impulse width for single bubble cavitation on a Schiebe headform with $r_H = 2.5cm$, $U = 9m/sec$ and $\sigma = 0.45$. The measurements were from Ceccio and Brennen (1992).

Chapter 7

Summary and Discussions

In this study a Phase Doppler Anemometer was calibrated using a holographic method for measuring the nuclei population in water. Substantial agreement was achieved between the measurements by the Phase Doppler Anemometer and by the holographic method. The Phase Doppler Anemometer was later used to study nuclei population dynamics in water tunnels and its effects on cavitation on an axisymmetric body.

Substantial differences in the nuclei number density distributions were found in two water tunnels. The differences in nuclei populations between the High Speed Water Tunnel and the Low Turbulence Water Tunnel can be as much as two orders in magnitude, though the shapes of the nuclei number density distributions are similar.

Although it has been found that the nuclei populations in different facilities are quite different, it has often been assumed that the nuclei population in a given tunnel is relatively constant during a cavitation experiment. In the present investigations, dramatic changes in the nuclei population in the same tunnel were found in the Low Turbulence Water Tunnel and in the High Speed Water Tunnel. The changes in the nuclei population can be as

much as an order of magnitude and are influenced by the tunnel design, the air content, the tunnel running time, the tunnel operating condition and the cavitation development in the working section.

The most dominant effect on the nuclei population comes from the tunnel design. In our experiments, the Low Turbulence Water Tunnel and the High Speed Water Tunnel differ in that the High Speed Water Tunnel has a resorber. Consequently, the nuclei population dynamics in these two tunnels showed very different characteristics. In the Low Turbulence Water Tunnel, the tunnel operating conditions have a strong effect on the nuclei population. Nuclei populations changed constantly with tunnel operating conditions. On the other hand, the nuclei population in the High Speed Water Tunnel was almost independent of the tunnel operating condition.

Since the tunnel design and the flow field in the tunnel are quite complex, we can not claim that these trends would necessarily occur in other tunnels. But the following observations on the effect of the tunnel design on the nuclei population dynamics seem to have generality. In a tunnel which has a resorber or a device to suppress the free air bubbles in the water before the flow re-enters the working section, the nuclei population probably will not be influenced by the tunnel operating condition, but will decrease with the tunnel running time regardless of the tunnel operating condition. On the other hand, if a tunnel does not have such a device, the nuclei population in the tunnel water will depend on the operating condition, and running the tunnel at different cavitation numbers will have different effects on the nuclei concentration. At low cavitation numbers, the concentration increases within a couple of minutes; at intermediate cavitation numbers, the nuclei concentration remains almost constant and at large cavitation numbers, the

nuclei concentration decreases over a long time. There appears to be an asymptotic nuclei concentration for each specific operating condition and the time constant associate with the approach to this condition is of the order of 100 minutes.

De-aeration and air injection also change the nuclei population. De-aeration will decrease the nuclei concentration while air injection can increase the nuclei population. But the effectiveness depends very much on the flow rate of de-aeration and air injection. The air injection and de-aeration systems used in the High Speed Water Tunnel are very effective; however, in the Low Turbulence Water Tunnel, the de-aeration system is less effective and the air injection system had very little effect on the nuclei population due to the very small flow rate in the air injection system.

For the first time, simultaneous measurement of the cavitation event rate on a headform and the nuclei population in the oncoming stream were performed at different water tunnel operating conditions. The experiments were carried out in the aforementioned two water tunnels to study the influence of the nuclei population on cavitation, since the High Speed Water Tunnel is nuclei poor, but the Low Turbulence Water Tunnel is nuclei rich. The cavitation event rate is mainly determined by the cavitation number. It increases dramatically as cavitation number is decreased. The free stream nuclei population also has a significant effect on the event rate which increases with increasing nuclei concentration. The shape of the nuclei number density distribution is also important. It is observed that the cavitation event rate can vary by as much as an order in magnitude at the same cavitation number due to the changes in the free stream nuclei population. The cavitation inception number based on a certain event rate reflects these variations.

At the same nuclei concentration level and the same cavitation number, it is observed

that the cavitation event rate decreases with an increasing tunnel velocity, which is the inverse of what would be expected since one would expect that more nuclei are convected to the low pressure region at a higher speed. All the numerical and analytical simulations (Ceccio and Brennen, 1992, Meyer *et al.*, 1992, and Liu *et al.*, 1993) predict that the event rate increases with the velocity, provided that the nuclei population remains the same. This velocity effect on the cavitation event rate was also observed by Kuhn de Chizelle *et al.* (1992). Since they were unable to measure the nuclei population in the oncoming flow, Kuhn de Chizelle *et al.* speculated that the free nuclei population was decreased by the increase in tunnel pressure at a higher speed (for the same cavitation number). The investigations of nuclei population dynamics in the Low Turbulence Water Tunnel support these speculations. However, the current data also shows that the event rates decrease with increasing tunnel speed even when the nuclei concentrations are at the same level. This phenomenon is not fully understood. A possible explanation is that there are more solid particles in the water at the higher speed. The increased population of solid particles could effect the event rate, or the PDA could have mistakenly counted more solid particles as microbubbles so that the actual microbubble population decreased even though the total nuclei concentration remained the same. It may also be the case that there exists some, as yet unrecognized, mechanism in the relation between the nuclei population and the cavitation event rate.

An asymptotic analytical model based on the spherical bubble assumption and the Rayleigh-Plesset theory was developed to relate the free stream nuclei population to the cavitation event rate and the acoustic noise. Similar in concept to the numerical model presented by Meyer *et al.* (1992), the model for the cavitation event rate has the advantage of ease of calculation and adaptation to other flows. It also includes complications such as

the effects of the boundary layer flow rate, the bubble screening, the bubble interactions and the observable bubble size. Among all these effects, bubble screening results in the largest reduction in the cavitation event rate and the effect of the bubble interactions becomes more important with increasing body size. The result of the combination of these effects can be a reduction in the event rate of an order of magnitude.

The scaling of the predicted cavitation event rate with body size, cavitation number and nuclei population agrees with the experimental observations. At larger cavitation numbers, the predicted cavitation event rates agree quantitatively with the experimental observations in the Low Turbulence Water Tunnel and the High Speed Water Tunnel. However, two outstanding issues still remain. First, the observed event rates at lower cavitation numbers are about an order in magnitude smaller than one would predict based on the actual nuclei distributions. This may be due to the fact that only a fraction of the observed nuclei actually cavitate or it may be due to some other effect which is not included in the model. A more detailed study is needed to confirm this. Second, the changes in the event rate with tunnel velocity can not be explained at present.

It is clear that the cavitation inception criteria are a natural consequence of the event rate variations described above. When the model for the event rates is used with some chosen criterion to predict the cavitation inception number, the results are consistent with those observed experimentally insofar as the trend with headform size is concerned. The trend with velocity is, of course, at odds with the experiments because of the discrepancy discussed in the context of the event rate. Nevertheless, it is shown that the cavitation inception values predicted using a certain critical event rate are consistent with those observed experimentally.

The acoustic emission from traveling bubble cavitation can be characterized by the acoustic impulse. Initially, the dimensionless acoustic pressure impulse increases as the cavitation number is decreased. However, as the cavitation number decreases further, the dimensionless acoustic pressure impulse starts to decrease. At the same cavitation number, the dimensionless acoustic pressure impulse also increases as the tunnel velocity decreases.

The predicted non-dimensional pressure impulse is a function of maximum bubble volume and cavitation number. It qualitatively predicts the upper limit for the acoustic emission. At lower cavitation numbers, the predicted pressure impulse quantitatively agrees with experimental observations; at larger cavitation numbers it over-predicts the impulse due to the non-spherical bubble collapse at those cavitation numbers. Since the acoustic emission of a spherically symmetric collapse is probably the most efficient noise producing mechanism for a given bubble volume, the analysis of the single bubble pressure impulse overestimates the impulse. Even with this assumption, the prediction of the magnitude of the pressure impulse agrees with the observations. The predicted impulse width also agrees with the experimental observations.

The advantage of the analysis presented is that it reveals the dependence of the acoustic emission on the flow parameters. The total acoustic emission is proportional to the square of the flow velocity, and the cube of headform size though various effects such as the boundary layer flow rate effect and the bubble screening effect will modify this scaling.

References

Acosta, A. J. and Parkin, B. R., "Cavitation inception – a selective review," *J. Ship Res.*, 19, pp. 193–205, 1975.

Akulichev, V. A., Boguslavskii, Y. Y., Ioffe, A. I. and Naugol'nykh, K. A., "Radiation of finite-amplitude spherical waves," *Soviet Physics Acoustics*, 13(3), pp. 281–285, 1968.

Arakeri, V. H. and Shangumanathan V., "On the evidence for the effect of bubble interference on cavitation noise," *J. Fluid Mech.*, 159, pp. 131–150, 1985.

Arndt, R. E. A. and Keller, A. P., "Free gas content effects on cavitation inception and noise in a free shear flow," *Proc. IAHR Symp. on Two Phase Flow and Cavitation in Power Generation Systems*, pp. 3–16, Grenoble, France, 1976.

Baiter, H. J., "Aspects of cavitation noise," *Proc. Symp. on High Powered Propulsion of Ships*, pp. 1–39, Wageningen, The Netherlands, 1974.

Billet, M. L., "Cavitation nuclei measurement – a review," *Proc. ASME Cavitation and Multiphase Flow Forum*, pp. 31–38, 1985.

Billet, M. L., "The importance and measurement of cavitation nuclei," *Proc. ASCE Advances in aerodynamics, fluid mechanics and hydraulics*, 1986.

Blake, W. K., "The onset of cavitation in liquids: I," *Technical report, Tech. Memo. No. 12*, Acoustics Res. Lab., Harvard University, 1949.

Blake, W. K., Wolpert, M. J. and Geib, F. E., "Cavitation noise and inception as influenced by boundary layer development on a hydrofoil," *J. Fluid Mech.*, 80, pp. 617–640, 1977.

Blake, W. K., "Cavitation bubbles near boundaries," *Ann. Rev. Fluid Mech.*, 19, pp. 99–123, 1987.

Brennen, C. E., "Cavitation and bubble dynamics," Oxford Univ. Press, 1994.

Cartmill, J. W. and Su, M. Y. "Bubble size distribution under saltwater and freshwater breaking waves," *J. Dynamics of Atmospheres and Oceans*, 20, pp. 25-31, 1993.

Ceccio, S. L. and Brennen, C. E., "Observations of the dynamics and acoustics of traveling bubble cavitation," *J. Fluid Mechanics*, 233, pp. 633–660, 1992.

Chahine, G. L., Courbiere, P. and Garnaud, P., "Correlation between noise and dynamics of cavitation bubbles," *Proc. 6th Conf. on Fluid Machinery*, 199, pp. 155–176, Budapest, 1979.

Daily, J. W. and Johnson, V. E., "Turbulence and boundary layer effects on cavitation inception from gas nuclei," *Trans. ASME*, 78, pp. 1695–1706, 1956.

Esipov, I. B. and Naugol'nykh, K. A., "Expansion of a spherical cavity in a liquid," *Soviet Physics Acoustics*, 18(2), pp. 233–238, 1972.

Esipov, I. B. and Naugol'nykh, K. A., "Collapse of a bubble in a compressible liquid," *Soviet Physics Acoustics*, 19(2), pp. 187–188, 1973.

Feldberg, L. A. and Shlemenson, K. T., "The holographic study of cavitation nuclei," *Proc. IUTAM, Symp. on Non-Steady Flow of Water at High Speeds*, pp. 106–111, Leningrad, USSR(English version), 1973.

Fitzpatrick, H. M. and Strasberg, M., "Hydrodynamic sources of sound," *Proc. 1st ONR Symp. on Naval Hydrodynamics*, pp. 241-280, Washington D. C., 1956.

Flynn, H. G., "Physics of acoustic cavitation in liquids," *Physical Acoustics*, editor W. P. Mason, Academic Press, 1964.

Franklin, R. E. and McMillan, J., "Noise generation in cavitating flows, the submerged jet," *ASME J. Fluids Eng.*, 106, pp. 336–341, 1984.

Gates, E. M., "The influence of free stream turbulence, freestream nuclei populations and drag reducing polymer on cavitation inception on two axisymmetric bodies," *Technical report, Rep. E182-2*, California Institute of Technology, 1977.

Gates, E. M. and Acosta, A. J., "Some effects of several free-stream factors on cavitation inception on axisymmetric bodies," *Proc. 12th ONR Symp. on Naval Hydrodynamics*, pp. 86–108, 1978.

Gates, E. M. and Bacon, J., "A note on the determination of cavitation nuclei distributions by holography," *J. of Ship Research*, 22(1), pp. 29–31, 1978.

Gindroz, B. and Billet, M. L., "Nuclei and propeller cavitation inception," *Proc. ASME Symp. on Cavitation and Gas-Liquid Flow in Fluid Machinery and Devices, ASME FED-Vol. 190*, pp. 251–260, Lake Tahoe, 1994.

Hamilton, M. F., Thompton, D. E. and Billet, M. L., "An experimental study of traveling bubble cavitation and noise," *Proc. ASME Int. Symp. on Cavitation Noise*, pp. 25–33, 1982.

Harrison, M., "An experimental study of single bubble cavitation noise," *J. Acoust. Soc. Am.*, 28, pp. 776–782, 1952.

Holl, J. W. and Kornhauser, A. L., "Thermodynamic effects on desinent cavitation on hemispherical nosed bodies in water at temperatures from 80°F to 260°F," *ASME J. Basic Eng.*, 92, pp. 44–58, 1970.

Holl, J. W. and Treaster, A. L, "Cavitation hysteresis," *ASME J. Basic Eng., Series D*, 88(1), pp. 199–212, 1966.

Houghton, G., "Theory of bubble pulsation and cavitation," *J. Acoust. Soc. Am.*, 35, pp. 1387–1393, 1963.

Johnson, C. A., "Cavitation Inception on Headforms, Further Tests," *Proc. 12th ITTC*, pp. 381–392, Rome, Italy, 1969.

Johnson, V. E. and Hsieh, T., "The influence of the trajectories of gas nuclei on cavitation inception," *Proc. 6th ONR Symp. on Naval Hydrodynamics*, pp. 163–182, Washington D. C., 1966.

Katz, J., "Cavitation phenomena within regions of flow separation," *J. Fluid Mech.*, 140, pp. 379–463, 1984.

Keller, A. P., "The influence of the cavitation nucleus spectrum on cavitation inception, investigated with a scattered light counting method," *ASME J. Basic Eng.*, 94, pp. 917–925, 1972.

Keller, A. P., "Investigations concerning scale effects of the inception of cavitation," *Proc. I. Mech. E. Int. Conf. on Cavitation*, pp. 917–925, 1974.

Keller, A. P. and Weitendorf, E. A., "Influence of undissolved air content on cavitation phenomena at the propeller blades and on induced hull pressure amplitudes," *Proc. IAHR*

Symp. on Two Phase Flow and Cavitation in Power Generation Systems, pp. 65–76, Grenoble, France, 1976.

Knapp, R. T. and Hollander, A., "Laboratory investigations of the mechanisms of cavitation," *Trans. ASME.*, 70, p. 419, 1948.

Kuhn de Chizelle, Y. P., "Hydrodynamics, acoustics and scaling of traveling bubble cavitation," *Ph.D. Dissertation*, Division of Engineering and Applied Sciences, California Institute of Technology, 1993.

Kuhn de Chizelle, Y. P., Ceccio, S. L., Brennen, C. E. and Gowing, S., "Scaling experiments on the dynamics and acoustics of traveling bubble cavitation" *Proc. 3rd I. Mech. E. Int. Conf. on Cavitation*, pp. 165–170, Cambridge, England, 1992.

Kuhn de Chizelle, Y. P., Ceccio, S. L., Brennen, C. E. and Shen, Y., "Cavitation scaling experiments with headforms: bubble acoustics," *Proc. 19th Symp. on Naval Hydrodynamics*, pp. 72–84, Seoul, Korea, 1992.

Kuhn de Chizelle, Y. P., Ceccio, S. L., Brennen, C. E. and Shen, Y., "Cavitation scaling experiments with headforms: bubble dynamics," *Proc. 2nd Int. Symp. on Propeller and Cavitation*, pp. 272–279, Hangzhou, China, 1992.

Kuiper, G., "Scale effects on propeller cavitation inception," *Proc. 12th ONR Symp. on Naval Hydrodynamics*, pp. 400–429, Washington D.C., 1978.

Kumar, S. and Brennen, C. E., "Nonlinear effects in the dynamics of clouds of bubbles," *J. Acoust. Soc. Am.*, 89, pp. 707–714, 1991.

Kumar, S. and Brennen, C. E., "Some nonlinear interactive effects in bubbly cavitating clouds," *J. Fluid Mech.*, 253, pp. 565–591, 1993.

Le Goff, J. P. and Lecoffre, Y., "Nuclei and cavitation," *Proc. 14th Symp. on Naval Hydrodynamics*, National Academy Press, pp. 215–242, 1983.

Li, C. Y. and Ceccio, S. L., "Observations of the interactions of cavitation bubbles with attached cavities," *Proc. ASME Symp. on Cavitation and Gas-Liquid Flow in Fluid Machinery and Devices, ASME FED-Vol. 190*, pp. 283–290, Lake Tahoe, 1994.

Lindgren, H. and Johnson, C. A., "Cavitation inception on headforms: ITTC comparative experiments," *Proc. 11th ITTC*, pp. 219–232, 1966.

Liu, Z., Kuhn de Chizelle, Y. and Brennen, C. E., "Cavitation event rate and nuclei distributions," *Proc. ASME 4th Int. Symp. on Cavitation Inception, ASME FED-Vol. 177*, pp. 13–23, New Orleans, 1993.

Liu, Z., Sato, K. and Brennen, C. E., "Cavitation nuclei population dynamics in a water tunnel," *Proc. ASME Cavitation and Multiphase Flow Forum*, ASME FED-Vol. 153, pp. 119–125, Washington D. C., 1993.

Marboe, R. C., Billet, M. L. and Thompson, D. E., "Some aspects of traveling bubble cavitation noise," *ASME Int. Symp. on Cavitation and Multiphase Flow Noise*, pp. 119–126, 1986.

Meyer, R. S., Billet, M. L. and Holl, J. W., "Free stream nuclei and cavitation," *Proc. ASME Int. Symp. on Cavitation Inception*, pp. 55–62, 1989.

Meyer, R. S., Billet, M. L. and Holl, J. W., "Free stream nuclei and traveling bubble cavitation," *ASME J. Fluids Eng.*, 114, pp. 672–679, 1992.

Morgan, W. B., "Air content and nuclei measurement," *Proc., 13th ITTC*, 1, pp. 657–674, Berlin/Hamburg, Germany, 1972.

Neppiras, E. A. and Noltignk, B. E., "Cavitation produced by ultrasonics," *Proc. Phys. Soc.*, B 63, pp. 658–674, London, 1950.

Neppiras, E. A. and Noltignk, B. E., "Cavitation produced by ultrasonics: Theoretical conditions for the onset of cavitation," *Proc. Phys. Soc.*, B 64, pp. 1032–1038, London, 1951.

Oldenziel, D. M., "A new instrument in cavitation research: the cavitation susceptibility meter," *ASME J. Fluids Eng.*, Vol. 104, pp. 136–142, 1982.

Ooi, K. K., "Scale effects on cavitation inception in submerged water jets: A new look," *J. Fluid Mech.*, 151, pp. 367–390, 1985.

Oshima, R., "Theory of scale effects on cavitation inception on axially symmetric bodies," ASME J. Basic Eng., 83, pp. 379–398, 1961.

Parkin, B. R., "Scale effects in cavitating flow," *Ph.D. Dissertation*, California Institute of Technology, 1952.

Pauchet, A., Retaileau, J. and Woillez, J., "The prediction of cavitation inception in turbulent water jets," *Proc. ASME Cavitation and Multiphase Flow Forum, ASME FED-Vol. 135*, pp. 149–158, 1992.

Peterson, F. B., "Hydrodynamic cavitation and some considerations of the influence of free gas content," *Proc. 9th ONR Symp. on Naval Hydrodynamics*, 2, pp. 1131–1186, Paris, France, 1972.

Peterson, F. B., Danel, F., Keller, A. and Lecoffe, Y., "Determination of bubble and particulate spectra and number density in a water tunnel with three optical techniques," *Proc. 14th ITTC*, 2, pp. 27–52, Ottawa, Canada, 1975.

Plesset, M. S., "The dynamics of cavitation bubbles," *J. Appl. Mech.*, 16, pp. 277–282, 1949.

Plesset, M. S. and Prosperetti, A., "Bubble dynamics and cavitation," *Ann. Rev. Fluid Mech.*, 9, pp. 145–185, 1977.

Rayleigh, Lord (Strutt, John William), "On the pressure developed in a liquid during the collapse of a spherical cavity," *Philos. Mag.*, 34, pp. 94–98, 1917.

Ripken, J. R. and Killen, J. M., "A study of the influence of gas nuclei on scale effects and acoustic noise for incipient cavitation in a water tunnel," *Technical Report, Rep. 27-B.49*, St. Anthony Falls Hydraulic Lab., 1959.

Ripken, J. R. and Killen, J. M., "Gas bubbles: their occurrence, measurement, and influence in cavitation testing," *Proc. IAHR Symp. on Two Phase Flow and Cavitation in Power Generation Systems*, pp. 37–57, Sandai, Japan, 1962.

Rott, N. and Crabtree, L. F., "Simplified laminar boundary layer calculations for bodies of revolution and for yawed wings," *J. Aero. Sci.*, 19, pp. 553–565, 1952.

Saffman, M. and Buchhave, P., "Simultaneously measurement of size, concentration and velocity of spherical particles by a laser Doppler method," *Proc. 2nd Int. Symp. on Applications of Laser Anemometry to Fluid Mechanics*, Lisbon, 1984.

Sato, K., Liu, Z. and Brennen, C. E., "The microbubble distribution in the wake of a cavitating circular cylinder," *Proc. ASME Cavitation and Multiphase Flow Forum, ASME FED-Vol. 153*, pp. 75–80, 1993.

Schiebe, F. R., "Measurement of the cavitation susceptibility of water using standard bodies," *Technical Report, Rep. 118* , St. Anthony Falls Hydraulic Lab., 1972.

Tanger, H. and Weitendorf, E. A., "Applicability tests for the phase Doppler anemometer for cavitation nuclei measurements," *ASME J. Fluids Eng.*, 114(3), pp. 443–449, 1992.

Thwaites, B., Approximate calculations of the laminar boundary layer," *Aero. quart.*, 1, pp. 245–280, 1949.

van der Meulen, J. H. J., "Boundary layer and cavitation studies of NACA 16-012 and NACA 4412 hydrofoils," *Proc. 13th ONR Symp. on Naval Hydrodynamics*, Tokyo, Japan, 1980.

van der Walle, F., "On the growth of nuclei and related scaling factors in the cavitation inception," *Proc. 17th ONR Symp. on Naval Hydrodynamics, The Hague*, pp. 195–217, 1989.

Vogel, A., Lauterborn, W. and Timm, R., "Optical and acoustic investigations of dynamics of the laser-produced cavitation bubbles near a solid boundary layer," *J. Fluid Mech.*, 206, pp. 299–338, 1989.

Weitendorf, E. A. and Tanger, H., "Cavitation investigations in two conventional tunnels and the hydrodynamics and cavitation tunnel HYKAT," *Proc. ASME Symp. on Cavitation Inception, ASME FED-Vol. 177*, pp. 73–90, New Orleans, 1993.

Appendix A

Procedures for Adjusting Phase Doppler Anemometer

In this Appendix, we record the detailed instruction for the alignment of the PDA system. It is written in the form of instructions for the others but also documents the procedures used during the present experiments.

A.1 Alignment of the Transmitting Laser and Optics

Follow the procedure below step by step to align the transmitting laser and optics. But first keep in mind that laser beam could be extremely dangerous. Make sure that the area where the laser beams appear is well marked and clear of other personnel. Always wear a goggle and DO NOT look at any laser beam or its reflections directly at any time.

First put the mounting bench on a solid and flat ground. Mount the laser on the bench. Make sure the laser is pointing to a safe direction. Turn on the laser. Adjust the screws

under the laser box while moving the check plate with a pinhole forward and backward on the bench. Make sure the laser beam is parallel to the bench axis. Fix the laser tightly. If the laser position moves in the later steps, the transmitting laser and optics need to be realigned.

Mount the reference mirror on a stable support in a distance at least two meters from the position where the front lenses will be placed when the system is assembled (See figure A.1). Make sure that the reflection beam is also pointing to a safe direction. Tilt the mirror so that the incident and reflected beams are following the same path.

Mount the Bragg Cell on the bench. Use the two circular plates with a pinhole to adjust the Bragg Cell so that the transmitting and the reflected laser beams go through the pinholes. Rotate the Bragg Cell to make sure the laser beams go through the pinholes at any angle.

Take out the two circular plates. Put on the beam splitter on the laser side first. Adjust the beam splitter such that the split beam and its reflected beam are following the same path.

Put on the second beam splitter on the optics side. Excite the Bragg Cell by turning on the control box and running SIZEWARE. There are two Bragg Cell connectors on the rear panel of the PDA control box. Connect the Bragg Cell to the connector which is chosen in the SetUp window. Adjust the Bragg Cell for the first order diffraction. If the first order diffraction beam is not circular or not as strong as the other laser beam, do not proceed. Go back to adjust the Bragg Cell and the Beam Splitters until the above conditions are satisfied. Adjust the beam splitter such that the first order diffraction is following the same path as the transmitting laser beam.

Mount the beam translator and the front optics. Adjust the beam translator to make both the transmitting laser beams and their reflected beams follow the same paths. After putting on the front lenses, adjust the beam translator to make the two laser beams focus. The focus is checked by a projector.

Mount the two polarizers, one on the transmitting laser and the other one on the beam splitter. Adjust the direction of the polarization according to applications. The direction of the polarized laser beams is critical to the measurement. Refer to the User's Manual for a correct direction of polarization.

A.2 Adjustment of Receiving Optics and Electronics

After the transmitting optics are aligned, the following procedures should be followed.

Mount the receiving optics. Make sure that the receiver is on a plane normal to the laser beams. The distance from the laser focal volume to the front lenses of the receiver should be about $310cm$ in air. Calculate the actual distance according to how much the distance is in water; otherwise, you can not find the focal volume. Find the focal volume of the laser beams from the view finder on the receiving optics. Adjust the position so that the focal volume is approximately located at the cross in the view finder.

From the SIZEWARE, select velocity measurement only. Set the high voltage on PM 1 between 800V to 1200V. Adjust the receiver by the fine tune-up screws to achieve the best data rate. Then fix the receiver position.

Adjust the high voltage on photomultiplier 1 (PM 1). Watch the data rate and validation rate. As the voltage increases, the data rate should increase while the validation rate should be 100%. But if the voltage is too high and noise becomes mixed with the signal, the

validation rate begins to drop below 100%. Find the voltage at the edge where the validation rate begins to drop. This is the high voltage setup for the master photomultiplier, PM1. Now you should be able to measure particle/bubble velocity. If no measurement or signal is received by the computer, check the focus of the transmitting lasers and the polarization of the transmitting lasers. Make sure that the focal volume is generated by the first order frequency shifted laser beam and the other laser beam. Also make sure that you choose the correct polarization for the laser beams since at certain receiving angle the receiver can not see the laser beams with a certain polarization. A convenient check is to connect the output of PM 1 (on the front panel of the control box) to an oscilloscope. If there is Doppler burst signal, the problem is in the control box, computer or the connections between them. If there is no Doppler burst, the problem is either in the transmitting optics or in the receiving optics. Sometimes noise looks like a Doppler burst signal. Measuring the signal duration can distinguish a noise signal from a Doppler burst. Doppler burst usually has a duration about a millisecond order while noise usually has a much smaller duration.

Select measurement for both velocity and diameter. Connect the outputs of PM1 and PM2 (on the front panel of the control box of PDA). Adjust the high voltage of PM2 so that the Doppler burst signals on both PMs are at the same level. Adjust the high voltage on PM3 the same way.

Select the ERRS window. Adjust the high voltages on PM2 and PM3. Watch the phase error, data rate and validation percentage. Adjust the high voltages to achieve optimal values for all three parameters.

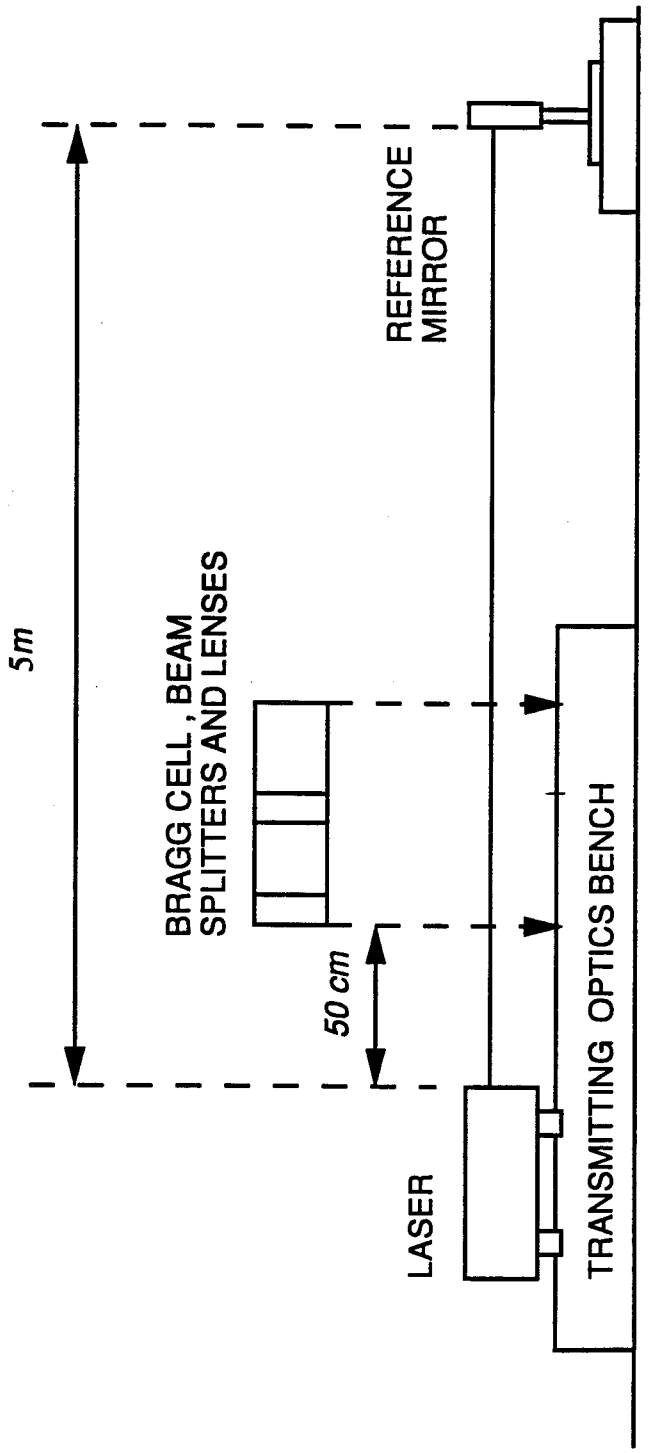

Figure A.1: A schematic of the transmitting laser and optics setup for the Laser Doppler Anemometry.

Appendix B

Bubble Screening Effects

In this Appendix, we will detail the calculations of the screening function, $\Sigma(r/r_H)$, i.e., the movement of a bubble relative to the stream lines. Referring to Chapter 5, Σ is defined as

$$\Sigma\left(\frac{r}{r_H}\right) = \int_A^B \frac{1}{\rho_L U^2}\left(\frac{\partial p}{\partial n/r_H}\right)\left(\frac{U}{q}\right) d\left(\frac{s}{r_H}\right) \tag{B.1}$$

Since the stagnation point flow is the same on any blunt axisymmetric body, it is appropriate to choose to examine the stagnation region in the potential flow around a sphere in order to evaluate $\Sigma(r/r_H)$. Consider the flow field near the front stagnation point of a sphere. Figure B.1 shows the coordinate and velocity definitions. Referring to figure B.1, the upstream flow velocity is U; the local velocity is $q = (u_\rho^2 + u_\theta^2)^{1/2}$ where u_ρ and u_θ are the velocity components in a spherical coordinate system. The velocity components in a cylindrical coordinate are denoted by u and v respectively. The relation between r and ρ and θ is

$$r = \rho \sin\theta \tag{B.2}$$

The stream function for incompressible and inviscid flow around a sphere is given by

$$\begin{aligned}\Psi &= \frac{1}{2}U\sin^2\theta\left(\rho^2-\frac{a^3}{\rho}\right)\\ &= \frac{1}{2}U\left(r^2-\frac{a^3\sin^3\theta}{\rho}\right)\\ &= \frac{1}{2}Ur_{up}^2\end{aligned} \tag{B.3}$$

where r_{up} is the distance between a stream line and the axis in the far upstream.

$$r_{up} = r^2 - \frac{a^3\sin^3\theta}{\rho} \tag{B.4}$$

It follows that the velocities in spherical coordinates are given by

$$\begin{aligned}u_\rho &= \frac{1}{\rho\sin^2\theta}\frac{\partial\Psi}{\partial\theta}\\ &= U\cos\theta\left(1-\frac{a^3}{\rho^3}\right)\\ u_\theta &= \frac{1}{\rho\sin\theta}\frac{\partial\Psi}{\partial r}\\ &= -U\sin\theta\left(1+\frac{a^3}{2\rho^3}\right)\end{aligned} \tag{B.5}$$

The axial and radial velocity components, u and v, are then given by

$$\begin{aligned}u &= -u_\rho\cos\theta + u_\theta\sin\theta\\ &= \frac{U}{4}\left(\frac{a^3}{\rho^3}-4+\frac{3a^3\cos(2\theta)}{\rho^3}\right)\\ v &= u_\rho\sin\theta + u_\theta\cos\theta\\ &= -\frac{U}{4}\left(\frac{3a^3\sin(2\theta)}{\rho^3}\right)\end{aligned} \tag{B.6}$$

From Bernoulli's equation for inviscid, incompressible and irrotational flow, we have

$$\frac{\partial}{\partial n}\left(\frac{p}{\rho_L}+\frac{q^2}{2}\right) = 0 \tag{B.7}$$

where α is the angle between the flow velocity and the axial axis. From the geometric relationships

$$\begin{aligned}\frac{\partial}{\partial n} &= \cos(\theta+\alpha)\frac{1}{\rho}\frac{\partial}{\partial\theta}+\sin(\theta+\alpha)\frac{\partial}{\partial\rho}\\ &= -\frac{u_\rho}{q}\frac{1}{\rho}\frac{\partial}{\partial\theta}+\frac{u_\theta}{q}\frac{\partial}{\partial\rho}\end{aligned} \tag{B.8}$$

Therefore,

$$\begin{aligned}-\frac{1}{\rho_L}\frac{\partial p}{\partial n} &= -\frac{u_\rho}{q}\frac{1}{\rho}\frac{\partial(q^2/2)}{\partial\theta}+\frac{u_\theta}{q}\frac{\partial(q^2/2)}{\partial\rho}\\ &= -\frac{u_\rho}{2q}\frac{1}{\rho}\frac{\partial(u_\rho^2+u_\theta^2)}{\partial\theta}+\frac{u_\theta}{2q}\frac{\partial(u_\rho^2+u_\theta^2)}{\partial\rho}\end{aligned} \tag{B.9}$$

Substituting (B.5) and (B.6) into (B.9), we have

$$-\frac{1}{\rho_L}\frac{\partial p}{\partial n}=\frac{U^3}{q}\left(\frac{-3a^3}{\rho^4}\right)\left[\frac{\sin^2\theta}{2}\left(1+\frac{a^3}{2\rho^3}\right)^2-\cos^2\theta\left(1-\frac{a^3}{\rho^3}\right)\left(2+\frac{a^3}{4\rho^3}\right)\right]\sin\theta \tag{B.10}$$

Referring to figure B.1, we have

$$\begin{aligned}ds &= \left(\frac{ds}{dr}\right)dr\\ &= \left(\frac{q}{v}\right)dr\end{aligned} \tag{B.11}$$

It follows that the integral

$$\begin{aligned}\Sigma\left(\frac{r}{r_H}\right) &= \int_A^B\frac{1}{Uq}\left(\frac{1}{\rho_L}\frac{\partial p}{\partial n}\right)ds\\ &\approx \int_{r_{up}}^a\frac{1}{Uq}\left(\frac{1}{\rho}\frac{\partial p}{\partial n}\right)\left(\frac{ds}{dr}\right)dr\\ &= \int_{r_{up}}^a\frac{1}{U}\frac{1}{v}\left(\frac{1}{\rho}\frac{\partial p}{\partial n}\right)dr\end{aligned} \tag{B.12}$$

Subtituting (B.10) and (B.6) into (B.12) and using equation (B.4) to replace ρ with r and r_{up}, we have

$$\Sigma\left(\frac{r}{r_H}\right)=\int_{r_{up}}^a\frac{1}{r\cos\theta}\frac{\left[\sin^2\theta\left(\frac{3}{2}-\frac{1}{2}\frac{r_{up}^2}{r^2}\right)^2+\cos^2\theta\frac{r_{up}^2}{r^2}\left(\frac{9}{2}-\frac{1}{2}\frac{r_{up}^2}{r^2}\right)^2\right]}{\left[\left(\frac{3}{2}-\frac{1}{2}\frac{r_{up}^2}{r^2}\right)^2+\cot^2\theta\frac{r_{up}^4}{r^4}\right]^{1/2}}dr \tag{B.13}$$

$\frac{r}{r_H}$	$\Sigma\left(\frac{r}{r_H}\right)$	$\frac{r}{r_H}$	$\Sigma\left(\frac{r}{r_H}\right)$	$\frac{r}{r_H}$	$\Sigma\left(\frac{r}{r_H}\right)$	$\frac{r}{r_H}$	$\Sigma\left(\frac{r}{r_H}\right)$
0.001	0.0466539	0.007	0.1444724	0.019	0.2419348	0.039	0.3343648
0.002	0.0707214	0.009	0.1654022	0.023	0.2649122	0.043	0.3479161
0.003	0.0896635	0.011	0.1838196	0.027	0.2851638	0.047	0.3603592
0.004	0.1057653	0.013	0.2003508	0.031	0.3032454	0.051	0.3718303
0.005	0.1199626	0.015	0.2153786	0.035	0.3195480	0.055	0.3824388

Table B.1: Numerical values of $\Sigma(r/r_H)$ as a function of r/r_H.

This equation can be integrated numerically. Table B shows the results of Σ as a function of r/r_H.

Using the minimum-least-square method to fit the data in the table, we have the analytical expression

$$\Sigma(r/r_H) = \Gamma(r/r_H)^{\gamma} \tag{B.14}$$

where $\Gamma \approx 1.69$, $\gamma \approx 0.5$.

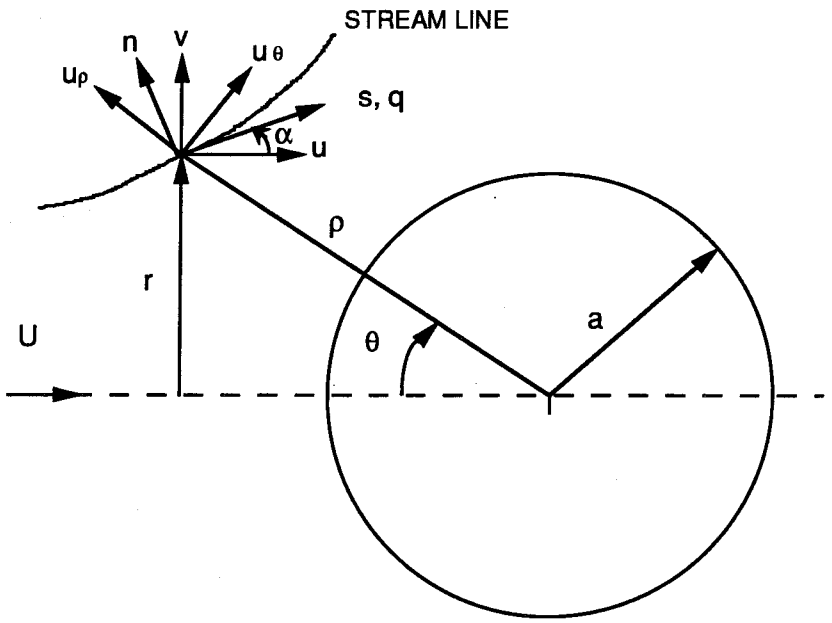

Figure B.1: Flow field around the stagnation point of a sphere.